ADVANCED NEUTRON IRRADIATION SYSTEM USING TEXAS A&M UNIVERSITY NUCLEAR SCIENCE CENTER REACTOR

A Dissertation

by

SI YOUNG JANG

Submitted to the Office of Graduate Studies of
Texas A&M University
in partial fulfillment of the requirements for the degree of

DOCTOR OF PHILOSOPHY

August 2004

Major Subject: Nuclear Engineering

ADVANCED NEUTRON IRRADIATION SYSTEM USING TEXAS A&M UNIVERSITY NUCLEAR SCIENCE CENTER REACTOR

A Dissertation

by

SI YOUNG JANG

Submitted to Texas A&M University
in partial fulfillment of the requirements
for the degree of

DOCTOR OF PHILOSOPHY

Approved as to style and content by:

Warren D. Reece (Chair of Committee)	Leslie A. Braby (Member)
Michael A. Walker (Member)	John Ford (Member)
William E. Burchill (Head of Department)	

August 2004

Major Subject: Nuclear Engineering

ABSTRACT

Advanced Neutron Irradiation System Using Texas A&M University Nuclear Science Center Reactor. (August 2004)

Si Young Jang, B.S., Hanyang University;

M.S., Korea Advanced Institute of Science and Technology

Chair of Advisory Committee: Dr. Warren D. Reece

A heavily filtered fast neutron irradiation system (FNIS) was developed for a variety of applications, including the study of long-term health effects of fast neutrons by evaluating the biological mechanisms of damage in cultured cells and living animals such as rats or mice. This irradiation system includes an exposure cave made with a lead-bismuth alloy, a cave positioning system, a gamma and neutron monitoring system, a sample transfer system, and interchangeable filters. This system was installed in the irradiation cell of the Texas A&M University Nuclear Science Center Reactor (NSCR).

By increasing the thickness of the lead-bismuth alloy, the neutron spectra were shifted into lower energies by the scattering interactions of fast neutrons with the alloy. It is possible, therefore, by changing the alloy thickness, to produce distinctly different dose weighted neutron spectra inside the exposure cave of the FNIS. The calculated neutron spectra showed close agreement with the results of activation foil measurements, unfolded by SAND-II close to the cell window. However, there was a considerable less agreement for locations far away from the cell window. Even though the magnitude of

values such as neutron flux and tissue kerma rates in air differed, the weighted average neutron energies showed close agreement between the MCNP and SAND-II since the normalized neutron spectra were in a good agreement each other.

A paired ion chamber system was constructed, one with a tissue equivalent plastic (A-150) and propane gas for total dose monitoring, and another with graphite and argon for photon dose monitoring. Using the pair of detectors, the neutron to gamma ratio can be inferred. With the 20 cm-thick FNIS, the absorbed dose rates of neutrons measured with the paired ion chamber method and calculated with the SAND-II results were 13.7 ± 0.02 Gy/min and 15.5 Gy/min, respectively. The absorbed dose rate of photons and the gamma contribution to total dose were 6.7×10^{-1} ± 1.3×10^{-1} Gy/min and 4.7%, respectively. However, the estimated gamma contribution to total dose varied between 3.6 % to 6.6 % as the assumed neutron sensitivity to the graphite detector was changed from 0.01 to 0.03.

ACKNOWLEDGMENTS

I would like to forever acknowledge that none of this work would be possible without Jesus Christ. First of all, I would like to thank my advisor, Dr. Dan Reece, for his sincere guidance and support in my graduate education, as well as livelihood in College Station. In addition, I would like to express my thanks to Dr. Leslie Braby for his endless and sincere technical advice. Special thanks go to Dr. John Ford and Dr. Michael Walker for their help and support as members of my committee. I would like to express my thanks to the NSC staff for their help and friendship. Finally, I would like to thank my family, my wife Kiyeon, my daughter Jiwon, and my son Sungjin, for their tremendous support.

TABLE OF CONTENTS

CHAPTER Page

LIST OF FIGURES

Page

Page

Page

Page

Page

LIST OF TABLES

CHAPTER I

INTRODUCTION

1.1. BACKGROUND

In 1994, a Task Group submitted a report titled "Biological Effectiveness of Neutrons: Research Needs" (ORAU 1994) to the Federal Government's Committee on Interagency Radiation Research and Policy Coordination. The concluding observation of this report was that "an effective program focused upon the radiobiology of neutrons requires that adequate laboratory and irradiation facilities be available and adequately staffed." This report also pointed out that "due to the limitations of human data in terms of statistics and types of exposures where data are available, and the limitations of extrapolating animal data to humans, the long term solution to estimating health risks will depend on a better understanding of the underlying mechanisms." Unfortunately, as university and Department of Energy research reactors have been shut down, the number of facilities where the needed neutron irradiation spectra can be found has continued to diminish. Furthermore, the biological significance of radiation response in cells that have not been traversed by a charged particle has become a major question in the area of risk evaluation for high LET radiations.

Although a great deal of work, reviewed in the CIRRPC report (ORAU 1994), has been done on the biological effectiveness of neutrons in animals and cell culture systems, very little of this can be used to evaluate the significance of a bystander cell effect or to guide development of risk evaluation models. Most of the mechanistic

---

This dissertation follows the style of Health Physics.

studies were done with mammalian cells grown as a mono-layer on a plastic substrate. This irradiation configuration, and the cellular and molecular endpoints that were utilized, limited the results to those expressed by individual irradiated cells. In intact organisms, cells seldom exist in mono-layers, or occur in isolation from surrounding cells. In order to understand the mechanisms of damage and repair that are mediated, in part, by a bystander cell effects, it is necessary to conduct experiments with three-dimensional tissue systems expressing normal cell growth and differentiation characteristics. A recent emphasis of the Department of Energy Low Dose Research Initiative has been on the development of experimental systems for studying low dose effects, including the bystander effect, in tissues and other three-dimensional systems. Several new approaches have been proposed, and research is progressing. Eventually it will be necessary to test models derived from this tissue response research in test animals and in *in vivo/in vitro* systems.

Organ culture and small animal experiments to test radiation risk models place stringent demands on the neutron irradiation system used to conduct the research. The biological effectiveness of neutrons is thought to be a strong function of the neutron energy or other measure of “radiation quality”. Cell and tissue responses also seem to be strongly influenced by the environmental conditions such as temperature and atmosphere composition. Therefore, to test models of radiation risk requires an irradiation facility that provides two or more well characterized neutron fields with significantly different radiation quality, minimum gamma ray contamination, adequate dose rates, and controlled environmental parameters.

1.2. LITERATURE REVIEW

Previous work at the Armed Forces Radiobiology Research Institute (AFRRI) has shown that it is possible to achieve gamma dose rates of less than 10 % of the total dose rate in fission neutron beams by enclosing the sample to be irradiated in a shield constructed primarily of lead (Prasanna et al. 2002). AFRRI has established a neutron irradiator using a TRIGA reactor that delivers a fission neutron field with a 30:1 neutron/photon absorbed dose ratio; the design used lead bricks and fission neutron beams including thermal neutrons, with the photon contamination mostly shielded. Hence, the neutron spectrum of the AFRRI facility was close to that of fission neutron spectrum in the reactor core. The AFRRI facility has a movable lead shielding system, which can be placed in front of the reactor core to increase the neuron to gamma ratio (Redpath et al. 1995). In addition, the exposure room is lined with a gadolinium-cadmium shielding materials to minimize the scattered thermal neutrons (Zeman et al. 1988). The exposure cave was built of lead bricks, 5 cm-thick, and the outside dimensions of the system were 71 cm in height and 51 cm in width and depth. Additional 15-cm lead shielding was placed in front of the exposure cave (Prasanna et al. 1997). The samples were loaded into the cave manually through the extractor tube, which penetrated the exposure room wall.

The University of Massachusetts Lowell Research Reactor has installed a Fast Neutron Irradiator (FNI) in the pool area of the reactor (White and Jirapongmed 2002) to provide a large-volume irradiation location for the irradiation of electronic parts, which

has a high fast neutron flux with low thermal neutron and gamma flux. One of the design goals was to provide neutron beam that have a 10:1 fast-to-thermal flux ratio and a total gamma dose rate to the sample less than 1 kGy/hr (White and Jirapongmed 2002).

On the other hand, research in Boron Neutron Capture Therapy (BNCT) are currently under way in many different places, utilizing epithermal neutrons with low-levels of fast neutrons and gamma-ray contamination (Ross et al. 1993; Matsumoto 1996; Sakurai and Kobayashi 2000). Although these BNCT studies have the same goal in minimizing gamma-ray contamination, materials with high-scattering cross-sections are used to produce epithermal neutrons by slowing down fast neutrons.

1.3. OBJECTIVE

The objective of this study is to develop a heavily filtered fast neutron irradiation system (FNIS) that will be used to evaluate the biological mechanisms which lead to long-term health effects from neutron exposure. In addition, the FNIS could be used to test electronic parts such as integrated circuit (IC) chips and semiconductors with fast neutrons. This irradiation system utilizes the Texas A&M University Nuclear Science Center Reactor (NSCR), which is a 1-MW pool-type MTR-converted TRIGA reactor, to provide an intense fission spectrum neutron source, carefully designed neutron filters to create spectra with different biological effectiveness, a heavily shielded exposure cave to minimize gamma dose, and a pneumatic sample transfer system to deliver samples for irradiation and to control dose without interrupting reactor operation. To accomplish this, an exposure cave of lead-bismuth alloy, a moving rail system, paired ion chambers

for dose monitoring, sample transfer system, and interchangeable filters were installed into the irradiation cell of the NSCR.

This study used the Monte Carlo N-Particle (MCNP) version 5 code (Briesmeister 2003) and a set of high-temperature ENDF/B-VI continuous neutron cross-section data for a realistic modeling of the reactor, the irradiation cell, and the FNIS. Sensitivity analyses were performed to find the characteristics of the FNIS as a function of the thickness of the lead-bismuth alloy. A paired ion chamber system was constructed with a tissue equivalent plastic (A-150) and propane gas for total dose monitoring and with graphite and argon for gamma dose monitoring. This study, in addition, confirmed the Monte Carlo modeling of the FNIS, as well as the performance of the system by comparing the calculated results with experimental data measured with activation foils and paired ion chambers.

Contents of this dissertation are as follows: materials and methods used in this study are presented in Chapter II. Section 2.1 describes the characteristics of the Nuclear Science Center Reactor (NSCR), including the explanation of both the reactor core and the irradiation cell. Section 2.2 deals with the design and construction of the filtered neutron irradiation system (FNIS) followed by the design requirements and the characteristics of the constructing materials. Section 2.3 explains the sample transfer and control system installed at the NSCR. The radiation monitoring system is presented in Section 2.4, including the paired ion chamber method, as well as the foil activation method for characterizing neutron energy spectra. The Monte Carlo modeling is

described in Section 2.5. This section contains the detail simulation scheme of the FNIS using the MCNP code.

In Chapter III, results and discussion are presented. Section 3.1 describes the results of sensitivity analyses using varying thickness of lead-bismuth alloy, the boral box installed outside of the FNIS, different neutron filters installed in front of the FNIS, and the reactor gap between the aluminum window of the irradiation cell and the void box of the reactor. Comparison of MCNP results with experimental data is discussed in Section 3.2. This section evaluates the 3-dimensional MCNP model without and with the FNIS in the irradiation cell by comparing the calculated MCNP results with those of neutron spectrum and dose rate measurements. Section 3.3 contains the explanation on the axial and radial distributions of neutrons inside the FNIS. Comparison of tissue kerma rate in air with absorbed dose rate in water is shown in Section 3.4. Finally, conclusions of this study are given in Chapter IV.

CHAPTER II

MATERIALS AND METHODS

2.1. OVERVIEW OF NUCLEAR SCIENCE CENTER REACTOR

2.1.1. General Overview

Since its initial operation on December 18, 1961, the Nuclear Science Center Reactor at Texas A&M University (NSCR) has been heavily utilized (NSC 2003). The NSCR, which is a 1-MW, pool-type TRIGA (Teaching, Research, and Isotopes, General Atomic) reactor, has been in active use for radioisotope production, Instrumental Neutron Activation Analysis (INAA), and various experiment setups such as delayed neutron counting, a real-time neutron radiography, and experiments with beam ports. The NSCR has a movable reactor core that can be placed at any position along the pool centerline. On the west side of the pool is an irradiation cell for large experimental objects as shown in Fig. 2.1.

The reactor has operated with a full FLIP (Fuel Life Improvement Program) core or FLIP/Standard mixed core since 1973; the current configuration is based on 4-element bundles with TRIGA-FLIP fuel (NSC 2003). Light water circulates through the reactor core by natural convection, acting as a neutron reflector and reactor coolant at the core perimeter, and graphite serves as an additional reflector on two sides to minimize neutron leakage. The concrete pool structure, including the stainless steel liner and the pool water, provide neutron and gamma ray shielding for the reactor. The shielding capacity is for a reactor operating at 5 MW, which is well above the current 1 MW maximum operating level (NSC 2003). The movable reactor bridge allows the operation

of the reactor at any position on the pool centerline, which runs approximately east to west as shown in Fig. 2.1.

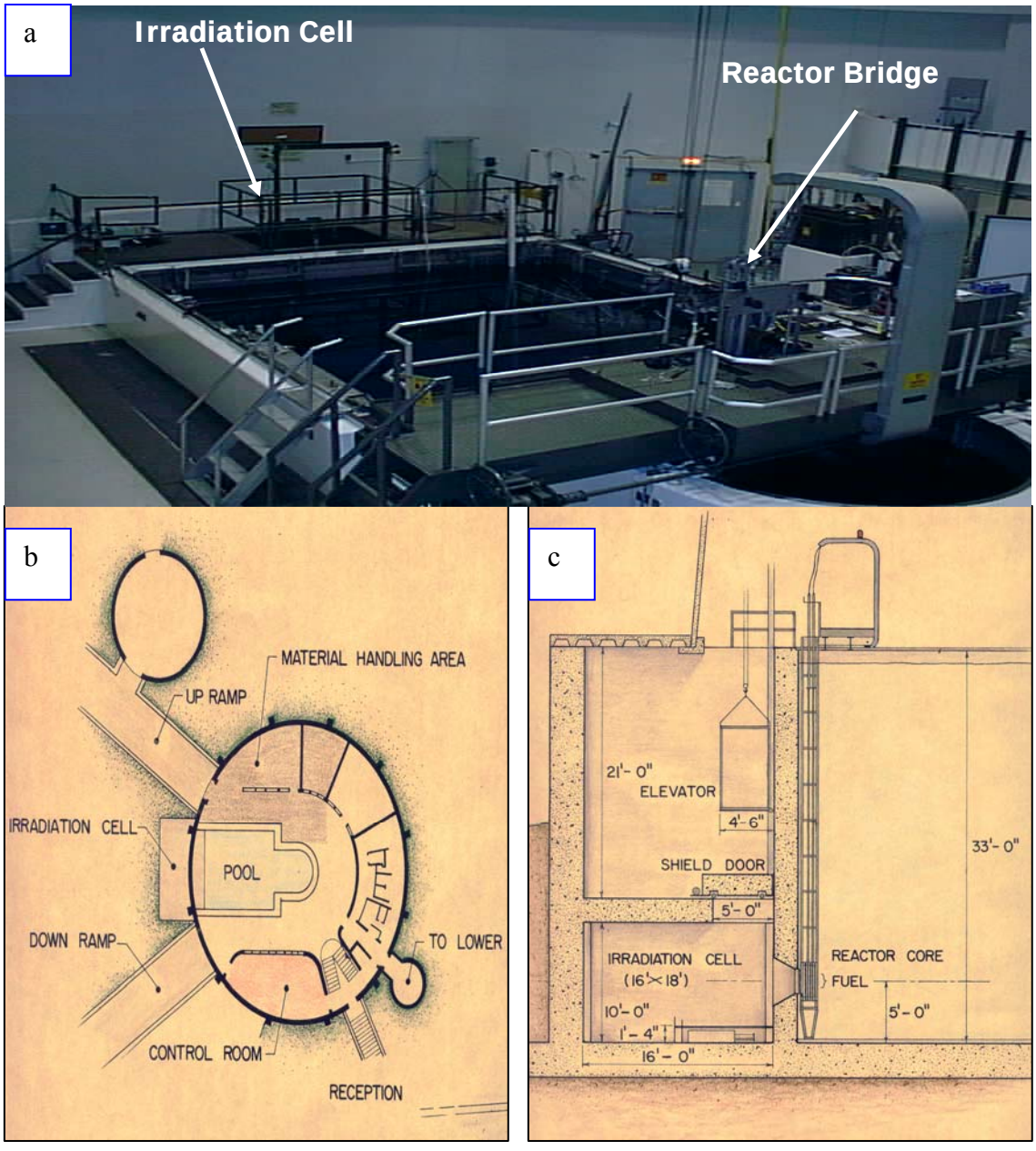

Fig. 2.1. a) General view of the NSCR at stall position. b) Upper research level plan of the NSCR, which shows a huge irradiation cell, reactor pool, and control room. c) Cross-section showing reactor positioned adjacent to entrance window of dry well.

Since the fuel configuration in the NSCR is such that the minimum nominal spacing between the fuel rods provides adequate convection cooling of reactor core up to 2.0 MW thermal power-rating, this spacing and the extra cooling holes at the corners of the bundle can enhance the core cooling capability. The increased depth of pool, in addition, improves the cooling capability of the NSCR. A suspension frame supported by a bridge yoke that spans the pool supports a grid block which in turn supports the fuel, reflector, control rods, samples and any others in-the reactor core. The pool is 10 m-deep and 5.5 m-wide in the main pool side and experimental penetrations consist of the thermal column, pneumatic tubes, beam ports and the irradiation cell window.

2.1.2. NSCR Core Characteristics

The NSCR obtained permission to operate full standard, mixed, or full FLIP TRIGA cores in June 1973 (NSC 2003). The mixed core is licensed to operate at a maximum steady-state power of 1 MW with a maximum pulse reactivity insertion of $2.00. In July 1973, the first NSCR mixed TRIGA core, containing 35 FLIP and 63 standard elements, went into service. In July 1975, the maximum permissible pulse reactivity insertion was increased to $2.70. The NSCR has operated with two mixed core loadings containing 35 FLIP and 59 FLIP since initial approval in June 1973. Since the late 1970s, the NSCR, however, has been operating with all FLIP fuel.

The current NSCR core configuration as shown in Fig. 2.2 contains 92 regular fuel elements, an instrumented fuel element, 4 shim safety rods, a transient rod and a regulating rod (Kim et al. 2004). The fuel elements and control rods are grouped into 4-rod bundles, which are positioned and supported by an aluminum grid plate containing a 6 by 9 array of holes. The graphite blocks, detectors, pneumatic devices and various experiments are also positioned and supported by the holes on the grid plate. The grid locations on the core are addressed by the column (A, B, C, D, E and F) and row (1, 2, 3, 4, 5, 6, 7, 8 and 9) of the grid plate. The four positions in each bundle are specified by NW (northwest), NE (northeast), SW (southwest) and SE (southeast). The grid locations in column A (more specifically, A2, A4, A6 and A8) on the grid plate are available for positioning various experiments or irradiation devices. The grid locations D3 and D7 are reserved for experiments that require fast neutrons or higher neutron flux. Pneumatic irradiation devices are installed at B1, C2, and D2 for short irradiations. The east face of the reactor core is used to irradiate large objects.

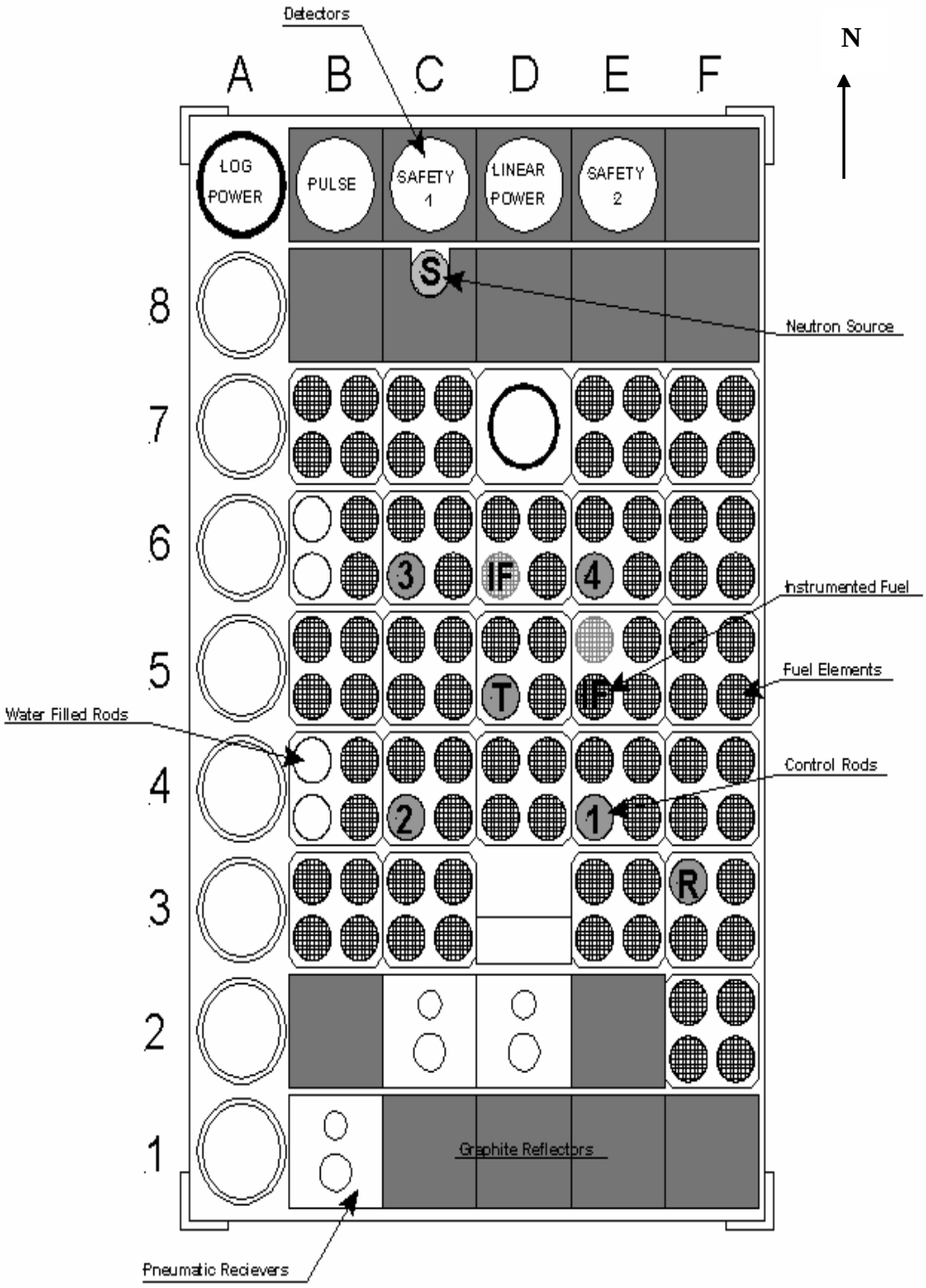

Fig. 2.2. NSCR reactor core configuration including control rods, graphite, and core monitoring instruments (NSC 2003).

2.1.3. Irradiation Cell

The irradiation cell (i.e., dry well) is a shielded structure adjoining the main pool as shown in Fig. 2.3 (NSC 2003). The irradiation cell was originally designed to perform reactor experiments for large objects such as large animals and motor/pumps or to serve as pool water storage (Gidden 1996). The cell is now, however, used mainly for the radiation exposure of small biological samples with the NSCR or various targets with the lanthanum gamma source. An irradiation window, which is located in the shield wall, separates the reactor pool and the irradiation cell. The reactor can operate any desired distance from the cell window for irradiating objects in the cell. The upper 5.2 m-length pool wall is made with standard concrete, while the lower portion of the pool wall is barites concrete and light concrete (NSC 2003). The NSCR can operate at steady state power levels up to 1 MW with the reactor placed against the irradiation cell at the west end of the main pool. Whenever radiation levels in the upper research level increase above 2.5 mR/hr, the control room can control all excess points to the upper and lower research levels.

The irradiation cell is 5.49 m wide by 4.88 m deep by 3.05 m high with 0.6 m thick concrete wall between the irradiation cell and reactor pool. The window is covered by an aluminum plate 1.27 cm thick on the pool-side and is readily accessible for equipment installation and modification. The window to the pool is 0.6 m square at the pool-side of the wall, expanding to 1.2 m square on the irradiation cell side. The reactor can operate with the front row of fuel elements unfilled, thus inserting a 7.62 cm water gap between reactor core face and irradiation window, or a void box containing air can be installed on

the front row filling the 7.62 cm-gap between reactor core face and the irradiation cell window. A 0.6 m-thick concrete ceiling covers the top of the irradiation cell. A 1.5 m by 1.5 m opening provides the access to the irradiation cell over the irradiation window. A motor-driven concrete slab rolls on tracks to cover the access hole when the reactor is in operation as shown in Fig. 2.4. The air from the dry well is vented to the central exhaust system to remove ^{41}Ar in the cell produced by the neutron activation of the air, and is monitored by a gas monitor before release to the environment.

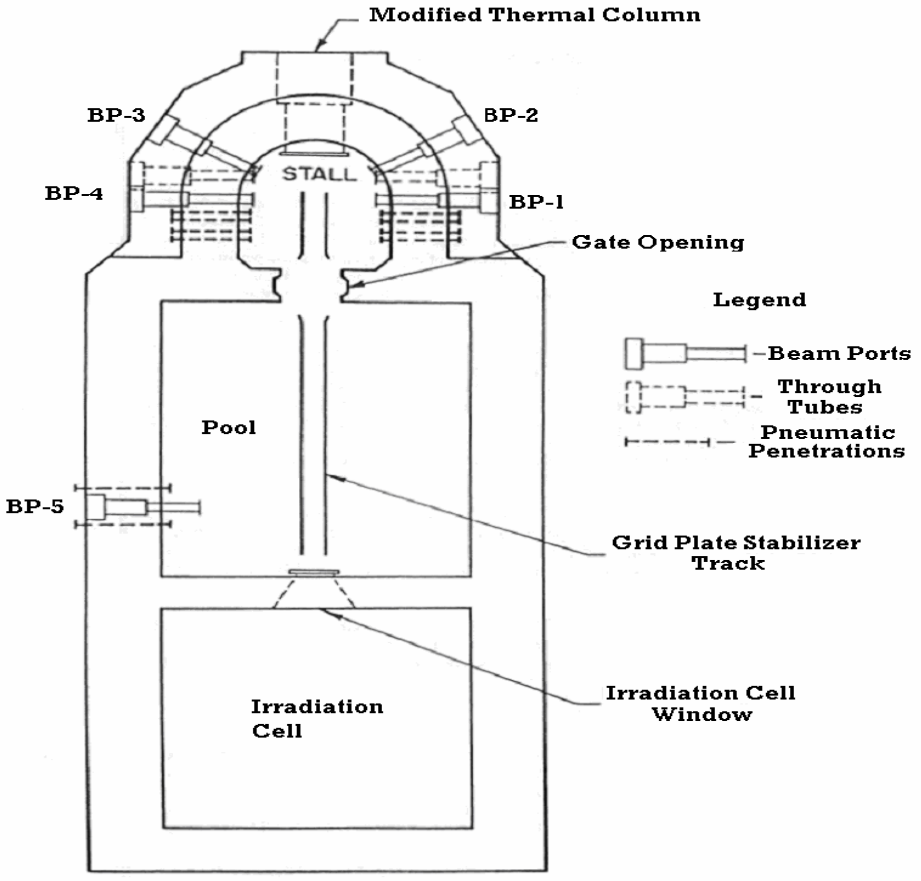

Fig. 2.3. NSCR general drawing including experimental facilities and irradiation cell.

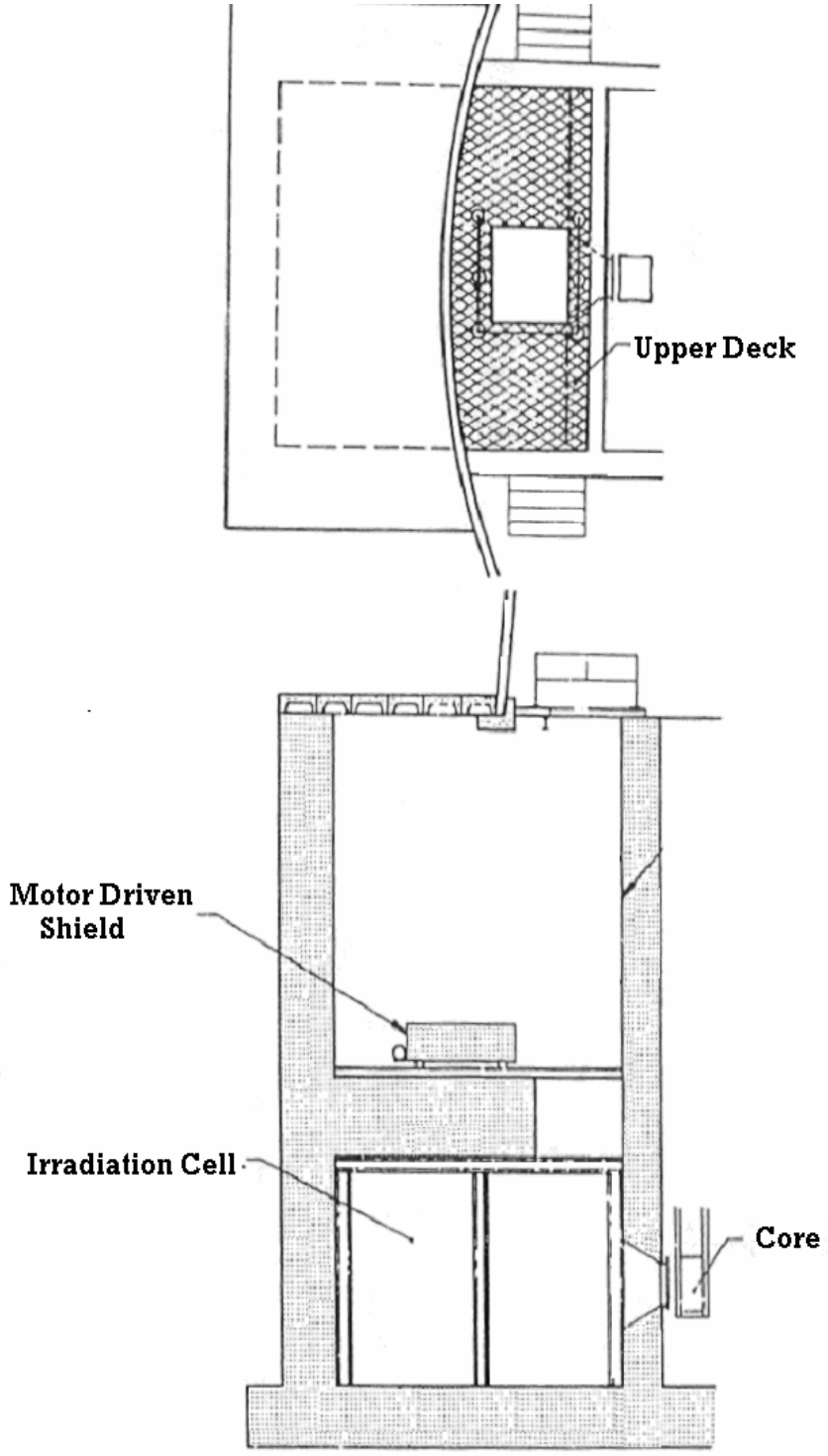

Fig. 2.4. Top and side views of the irradiation cell at the NSCR.

2.2. FILTERED NEUTRON IRRADIATION SYSTEM (FNIS)

2.2.1. Design Requirements

The objective of this study is to develop a heavily Filtered Neutron Irradiation System (FNIS) suitable for exposing tissue samples and small animals. This irradiation system would take advantage of the irradiation cell at the NSCR. Previous work at the Armed Forces Radiobiology Research Institute (AFRRI) has shown that it is possible to limit gamma dose rates to less than 10% in fission neutron beams by enclosing the sample being irradiated in a shield constructed primarily of lead (Redpath et al. 1995). The AFRRI design has established a neutron irradiator with a TRIGA reactor to deliver a fission neutron field capable of yielding a 30:1 neutron/photon absorbed dose ratio.

The detailed design requirements of this study were 1) to deliver fast neutron beams with mean neutron energy greater than 0.1 MeV with several distinctly different energy spectra into the exposure cave of the FNIS, 2) to deliver neutron dose to the samples with photon dose contamination of less than 5%, 3) to produce uniform dose distribution inside the exposure cave, 4) to be able to achieve a wide range of dose rates by moving the FNIS/reactor core or by adjusting the reactor power, 5) provide a sophisticated control system for sample transfer, which can transfer living animals or tissues with minimum dose received while they are in transit through the unfiltered neutron environment, and preventing damage which might be done by a sudden stop, and 6) provide neutron and gamma ray dosimetry.

For accomplishing the design requirements of the new neutron irradiation system, we used materials that have low absorption cross-sections for fast neutrons, as well as

suitable scattering cross-section, so as not to degrade fast neutron beams. In addition, we used thermal/epithermal neutron absorbers to cut off undesirable low energy neutrons. We designed the FNIS using a eutectic alloy of 54.9% bismuth and 44.5% lead as the major construction material, rather than pure lead, to minimize the production of capture gamma rays inside the FNIS.

2.2.2. Properties of Lead-Bismuth Alloy and Boral Plate

The eutectic lead-bismuth Alloy (44.5 w/o Pb, 54.9 w/o Bi) has a potential to be used as a coolant for liquid metal fast breeder reactor instead of liquid sodium (IAEA 2002). Table 2.1 shows some physical and thermal-physical properties characterizing this alloy (IAEA 1998). In this study, the low melting alloy of lead-bismuth (Belmont 2562G) manufactured by Belmont Metals Inc., was used to cast lead-bismuth bricks for the system setup. The lead-bismuth ingots as shown in Fig. 2.5 were melted using a furnace and then were poured into a steel form 10.16 cm × 48.26 cm × 5.08 cm to make the lead-bismuth bricks.

Table 2.1. Characteristics of the low melting alloy of lead-bismuth (Belmont 1997).

Properties	Nominal Value	Element	Abundance (w %)
Melting Temperature	396.6 K	Sb	0.25 max
Boiling Temperature	1943 K	Bi	54.9
Density	10.57 (g/cm^3)	Cd	0.25 max
Heat Capacity	146 (J/kg-K)	Cu	0.10 max
		Pb	44.5

Fig. 2.5. Lead-bismuth ingots, which contains 44.5 w % lead (Pb) and 54.9 w % bismuth (Bi), and lead-bismuth bricks for the FNIS setup, which have the size of 10.16 cm × 48.26 cm × 5.08 cm.

Although good photon shielding capability and mechanical strength should be considered as basic requirements to choose materials for constructing a heavy shielding system, low neutron capture cross-sections are desirable to minimize photon production inside the system. Figs. 2.6 and 2.7 show the mass attenuation coefficients (NIST 1996) and neutron cross-section data for lead and bismuth (ENDF 1998), respectively. In terms of neutron capture reaction with the shielding material, pure bismuth is better than pure lead due to low neutron absorption cross-section of the bismuth over the lower neutron energies, and bismuth, in addition, has a good shielding capability, which is almost equal to that of lead in attenuating gamma rays from reactor core and surrounding concrete. Bismuth is easy to machine into any shape. Pure bismuth, however, is too weak to support a heavy shield that may weigh more than 2 tons. To gain the advantages and to avoid the disadvantages of the pure bismuth, a low melting alloy of lead-bismuth was used in this study. In addition, the fission neutron spectrum is usually shifted down in energy whenever the neutrons pass through any high-Z materials such as lead and bismuth. This shift in energy is due to the energy dependence of the inelastic reactions, and neutrons below 1 MeV are accumulated as the higher-energy neutrons are scattered into a lower energy region (Prasanna et al. 2002).

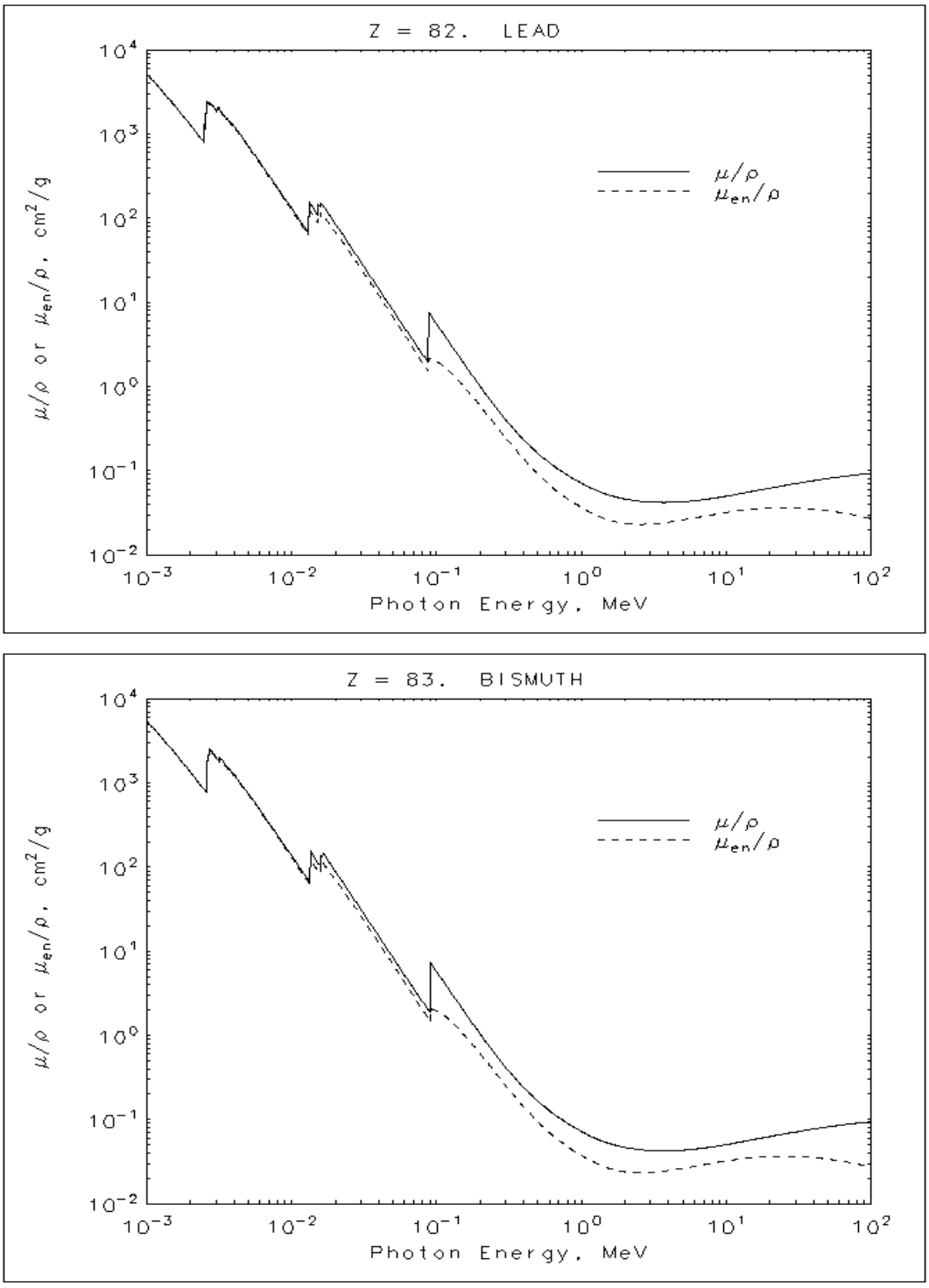

Fig. 2.6. Mass attenuation coefficients of lead and bismuth, respectively (NIST 1996).

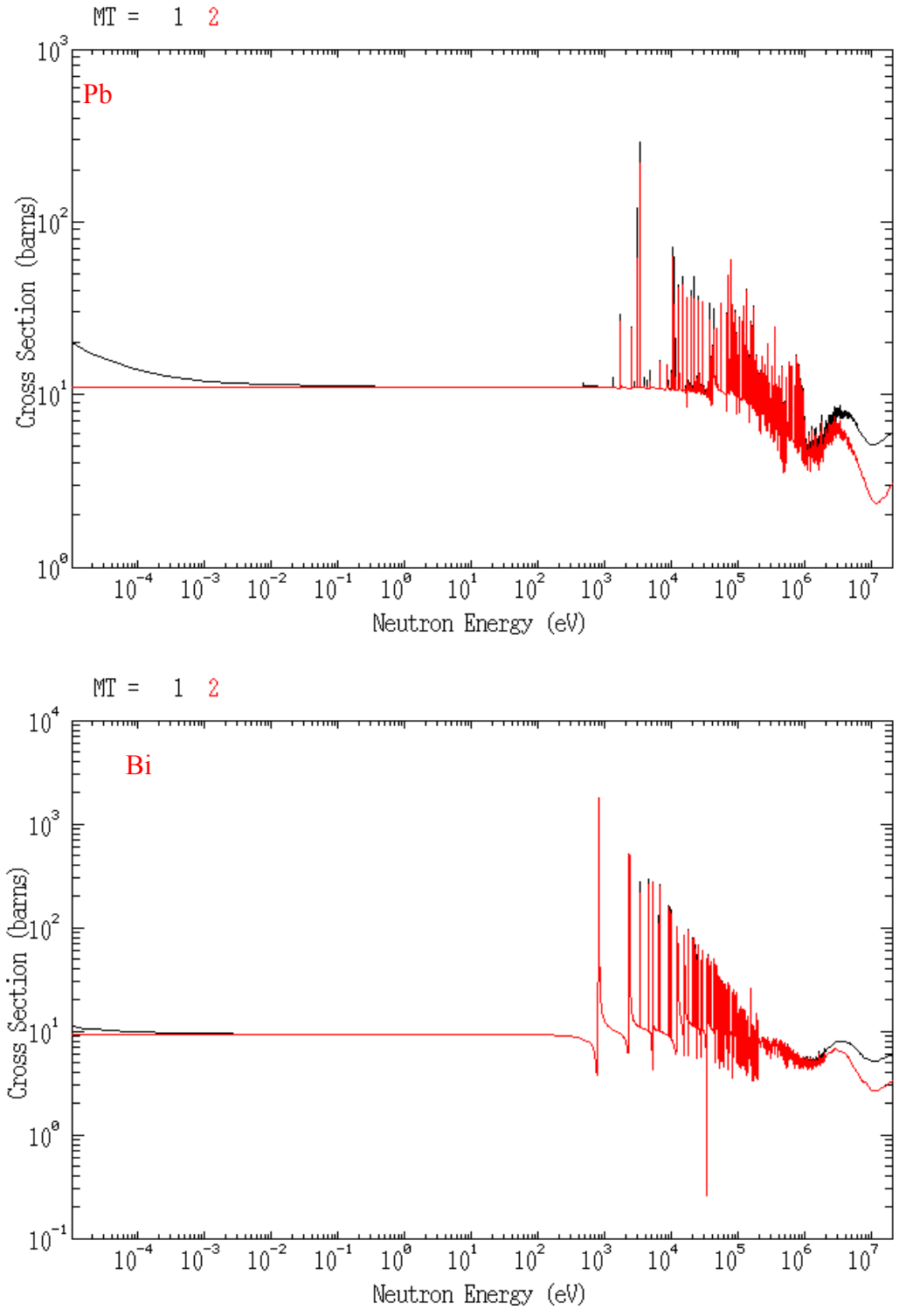

Fig. 2.7. Total (MT=1) and scattering (MT=2) cross-section data of lead and bismuth, respectively (ENDF 1998).

We use thermal/epithermal neutron absorbers to cut off undesirable low energy neutrons and to prevent unwanted gamma ray production in the exposure cave. In this study, we designed the FNIS using a eutectic alloy of 54.9% bismuth and 44.5% lead covered with boral plates to absorb any thermal neutrons. The boral^{TM} plate is a thermal neutron absorber material, composed of boron carbide (B_4C) and 1100 alloy aluminum (Brooks & Perkins 1983). The boral plate is a laminar composite of aluminum and boron carbide, consisting of three distinct layers. The outer layers of cladding are solid 1100 alloy aluminum, and the central layer consists of fine boron carbide particles bound tightly within an aluminum alloy matrix. It is a good shielding material for thermal neutron because the boron carbide provides a high neutron absorption cross-section for thermal neutrons and is stable, strong, and durable. In this study, 0.635 cm-thick boral plates were used to make a boral box outside the exposure cave as shown in Fig. 2.8, as well as a boral plate placed in front of the cell window in the pool side. For the boral box, each side of the box was cut from a large piece of a boral plate, penetrations were made, and then the box assembled using steel frames to support the weight of the FNIS.

Fig. 2.8. Boral box constructed for shielding against thermal neutrons.

2.2.3. Exposure Cave

To deliver optimum neutron spectra inside the exposure cave, assemblies functioning as beam filters were constructed behind the aluminum cell window as shown in Fig. 2.1. The NSC reactor operates with the void box installed on the front row of the grid plate, which fills the 7.62 cm-gap between core face and irradiation window to serve as a once-through transmitter for fast neutrons into the irradiation cell. The detailed specifications of the FNIS, including types and thickness of filters, were determined by simulating the irradiation cell, exposure cave, combination of filters, and reactor core with MCNP version 5 calculations, using ENDF/B-IV continuous neutron cross-section data as described in Section 2.5.

One of the design requirements of the exposure cave is to deliver neutron dose to the samples with photon dose contamination of less than 5%. To meet with this requirement, a cube was constructed as shown in Fig. 2.9, with outside dimensions of 58 cm in height and in width and 69 cm in depth, using 10-cm thick bricks of the eutectic lead-bismuth alloy (44.5 w % Pb, 55.5 w % Bi) mentioned in Section 2.2.2 to cut off incident gamma rays with a minimal absorption of fast neutrons. To minimize radiation streaming through the gap of the bricks, each brick was machined to have a 2.54 cm-wide and 0.16 cm-deep groove centered in the 10 cm-wide face and running its full length. During assembly, a lead strip, 2.54 cm wide and 0.32 cm deep, was placed into the groove. A steel frame was installed inside the system to attenuate gamma rays streaming through the edges of the exposure cave. The inner dimension of the exposure cave is a cube 38 cm × 38 cm × 49 cm that can accept small rodents, as well as a radiation monitoring system. In addition, a square penetration hole 15 cm on each side was made through the back wall of the exposure cave for sample loading and unloading.

Although the boral plate, installed in front of the irradiation cell window, absorbs thermal neutrons from the reactor and pool, the neutron thermalization process in the concrete walls of the irradiation cell produces other thermal neutrons. Therefore, some areas of the irradiation cell were lined with boral plates to cut thermal neutrons emerging from the concrete. In order to deliver neutron beams to inside of the cave with minimum gamma dose, the lead-bismuth cave was put inside a box made of boral plates supported by steel frames (see Fig. 2.8) to minimize capture gamma rays from the lead-bismuth alloy.

Fig. 2.9. Exposure cave for sample irradiation, which was constructed with the lead-bismuth bricks.

The penetration hole was connected to the sample transfer system and the internal steel frame installed to support the weight of the cave. In addition, three steel bands were installed outside the lead-bismuth bricks to bind all bricks together. Tissue equivalent and graphite ion chambers as described in Section 2.4 were installed inside the system to monitor total and photon dose rates. All of these components were put on a steel table that can move the exposure cave to any location of interest based on desired dose rates. Four steel wheels installed in the steel table can sustain a weight of one ton per a wheel, so that the table can support a total weight of 4 tons. A track was constructed with steel H-beams to hold the steel table. Rail stops were installed at the ends of the track for safety. Finally, the table and the track were moved down to the irradiation cell and were installed in front of the cell window at the irradiation cell as shown in Fig. 2.10.

Fig. 2.10. Components used to set up the exposure cave inside the irradiation cell, and final setup of the FNIS including the exposure cave, movable working table, track, and detectors installed inside the irradiation cell.

2.3. SAMPLE TRANSFER AND CONTROL SYSTEM

We need to provide a sophisticated control system for sample transfer, which can transfer living organisms or tissues with minimum dose received while they are in transit through the unfiltered neutron environment, and preventing damage which might be done by a sudden acceleration/deceleration. To achieve rapid transfer of samples without injury, a specially designed pneumatic transfer system, capable of sending a 9 cm-size sample carrier (outer diameter) into the exposure cave in a few seconds and of bringing it back to the upper research level, was installed as shown in Fig. 2.11. The sample loading box located in the upper research level was designed to sustain negative pressure for minimizing any leakage of airborne radioactive materials. A bypass pipe was installed also to reduce the traveling speed of sample carrier approaching the sample loading box from the irradiation cell.

As shown in Fig. 2.12, two sensors, which were made of micro-switch and infrared-LED/photo-transistor, were installed in the exposure cave and in the upper research level, respectively, to control the blower units, as well as the exposure time. The sample transfer pipe was installed through a small penetration between the top of the irradiation cell and the second level of the irradiation cell. Since there are several tortuous turns, bent or curved 45-degree radii PVC pipes were used to prevent any blockage in the sample transfer pipe during the sample movement. To minimize any mechanical shock to samples or animals, round shaped sample carriers will be used. Fig. 2.13 shows the overall configuration of the sample transfer system installed in the upper cell, as well as in the lower cell.

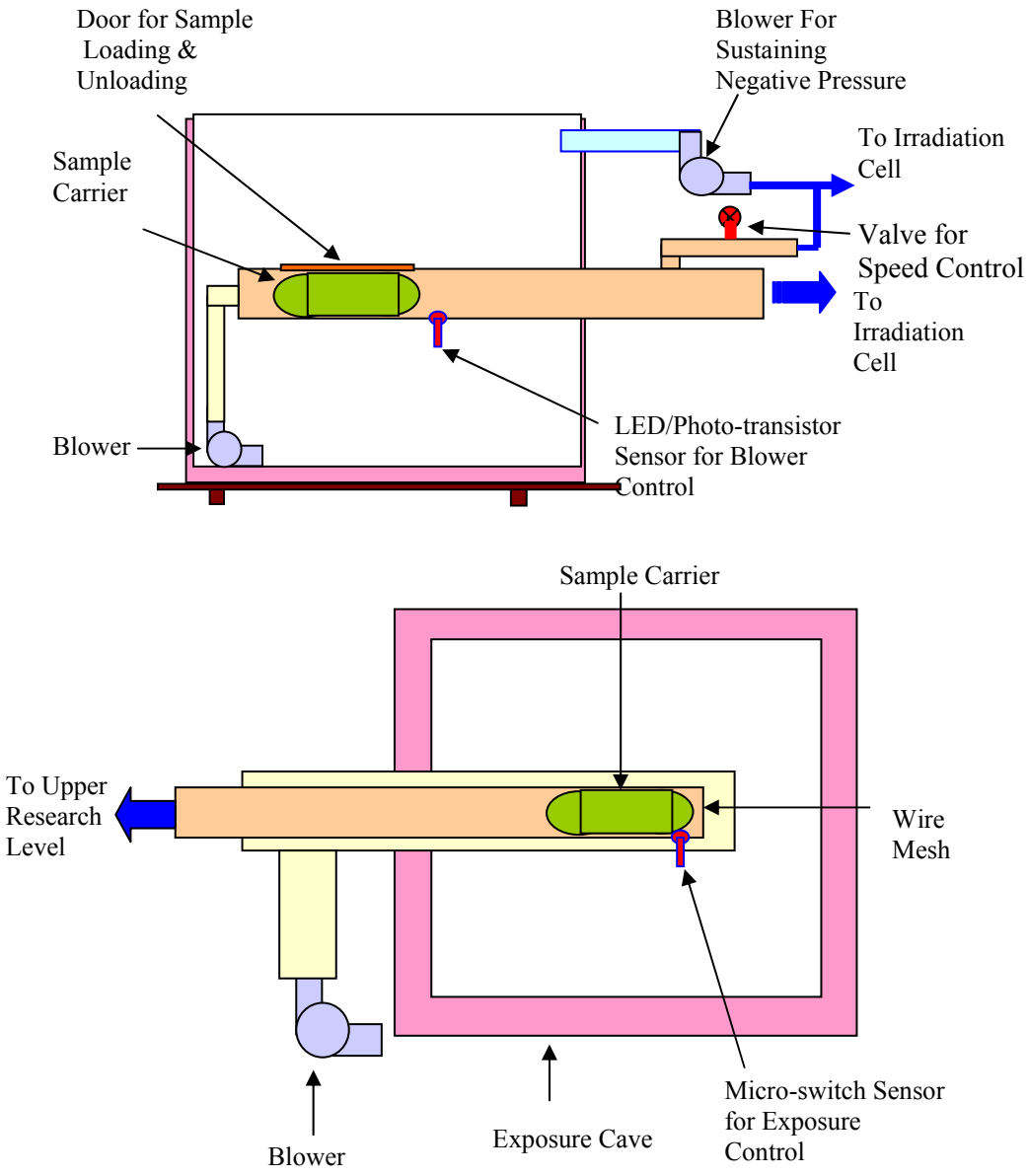

Fig. 2.11. Diagram of the sample transfer system installed in the upper research level (top) and in the irradiation cell (bottom) for sample loading/unloading and exposure control.

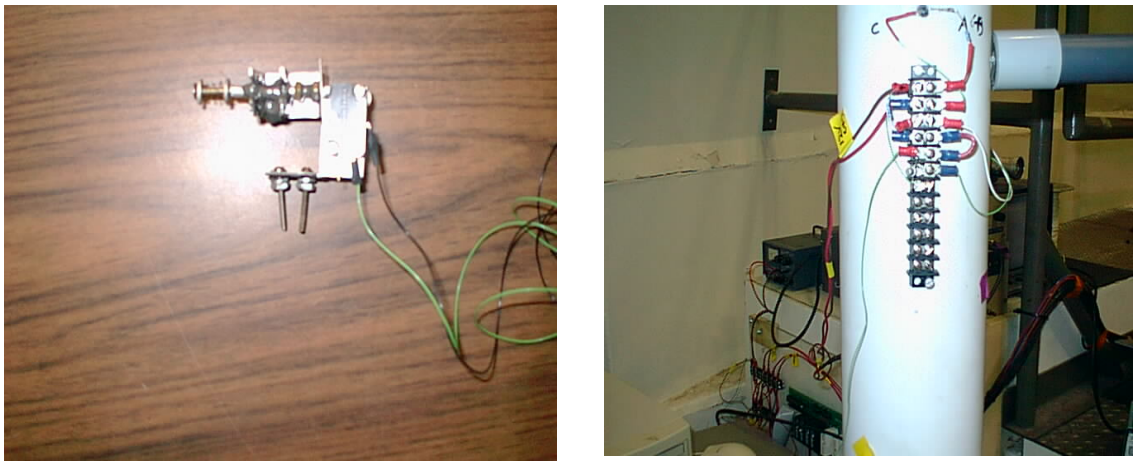

Fig. 2.12. Home-made sensor made of micro-switch (left-hand side) and LED/photo-transistor (right-hand side) for blower control, as well as for exposure time control.

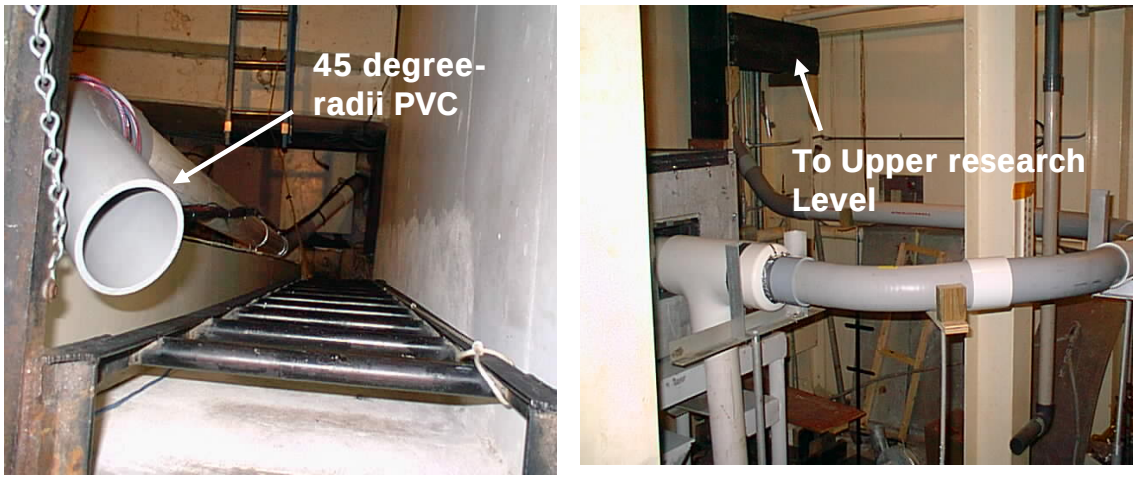

Fig. 2.13. Sample transfer system installed in the upper research level and in the irradiation cell for sample loading/unloading and exposure control.

After installing the PVC pipe through the penetration between the upper cell and the lower cell, 8-cm thick boron-containing polyethylene panels were installed for minimizing neutron streaming around the penetration and the PVC pipe as shown in Fig.

2.14. In addition, portable wooden boxes containing high-density polyethylene particles were constructed to minimize the neutron streaming through the concrete door between the upper cell and the lower cell. Fig. 2.15 shows the sample transfer box installed in the upper research level for sample loading and unloading.

Fig. 2.14. Boron-containing polyethylene panel and portable wooden box for minimizing neutron streaming through the penetration and the concrete door.

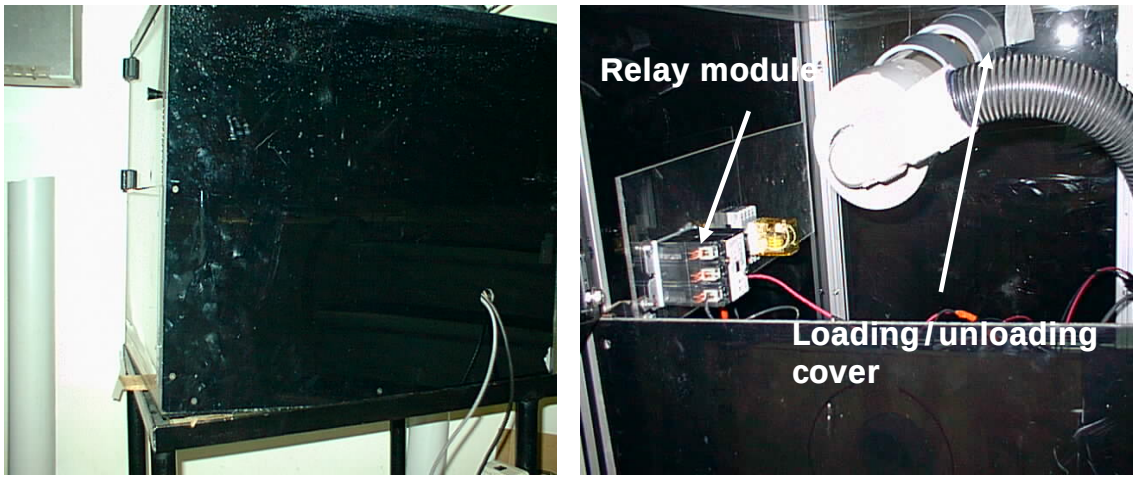

Fig. 2.15. Sample transfer box installed in the upper research level for sample loading and unloading.

As shown in Fig. 2.16, a computerized control system was constructed using Visual-Basic™ to manipulate each module of the system automatically. Data collection and blower control were performed using a digital data interface card (PCI-DIO24™ manufactured by Measurement Computing Corporation), as well as a relay module as shown in Fig. 2.17. The dose monitoring data were collected using RS-232 serial communication ports in the computer. Preset values of exposure time, or neutron absorbed dose can be used to initiate sample retrieval by the pneumatic system.

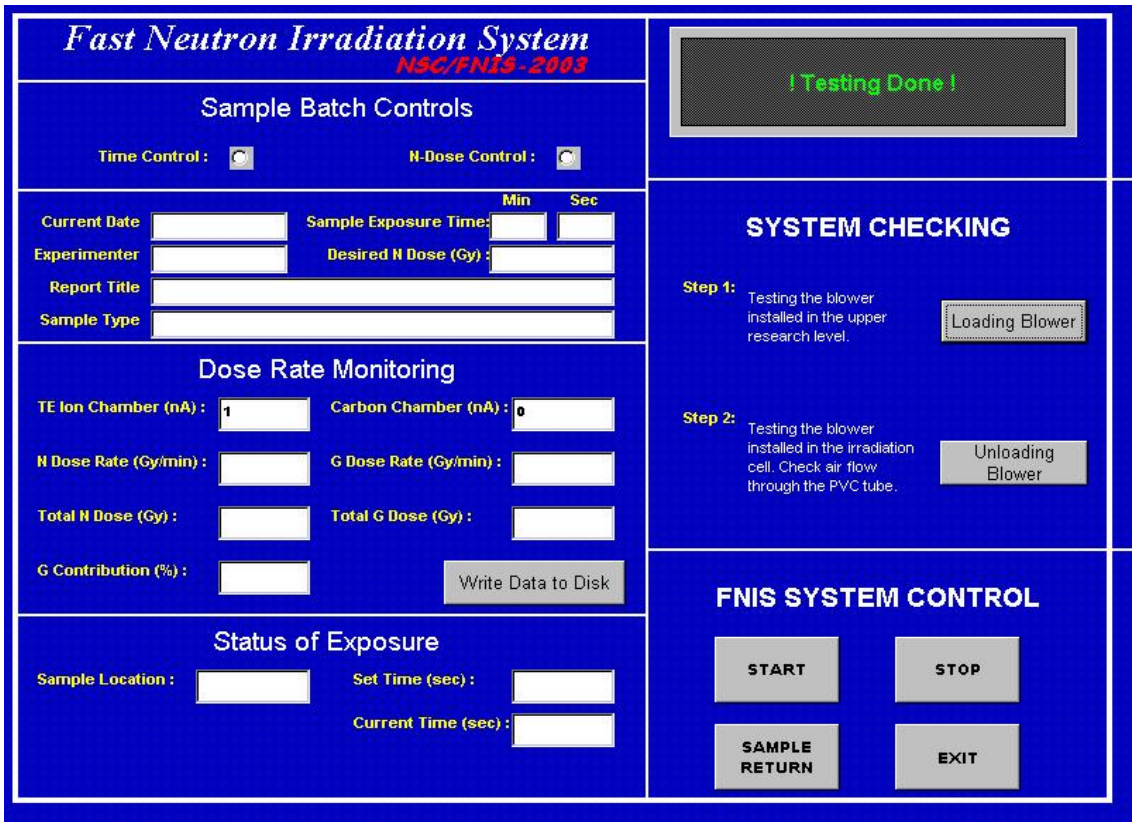

Fig. 2.16. Computerized control system for manipulating each module of the FNIS system automatically.

After the sample is loaded inside the exposure cave using the sample-loading blower, the micro-switch installed inside the exposure cave can send a signal for sample exposure and then for shut the sample-loading blower off to the data interface card. After exposing samples for some time, the sample-unloading blower is activated by the signal transmitted through the data interface card. The sample unloading blower is shut automatically when the samples pass through the LED/photo-transistor sensor located in the upper research level.

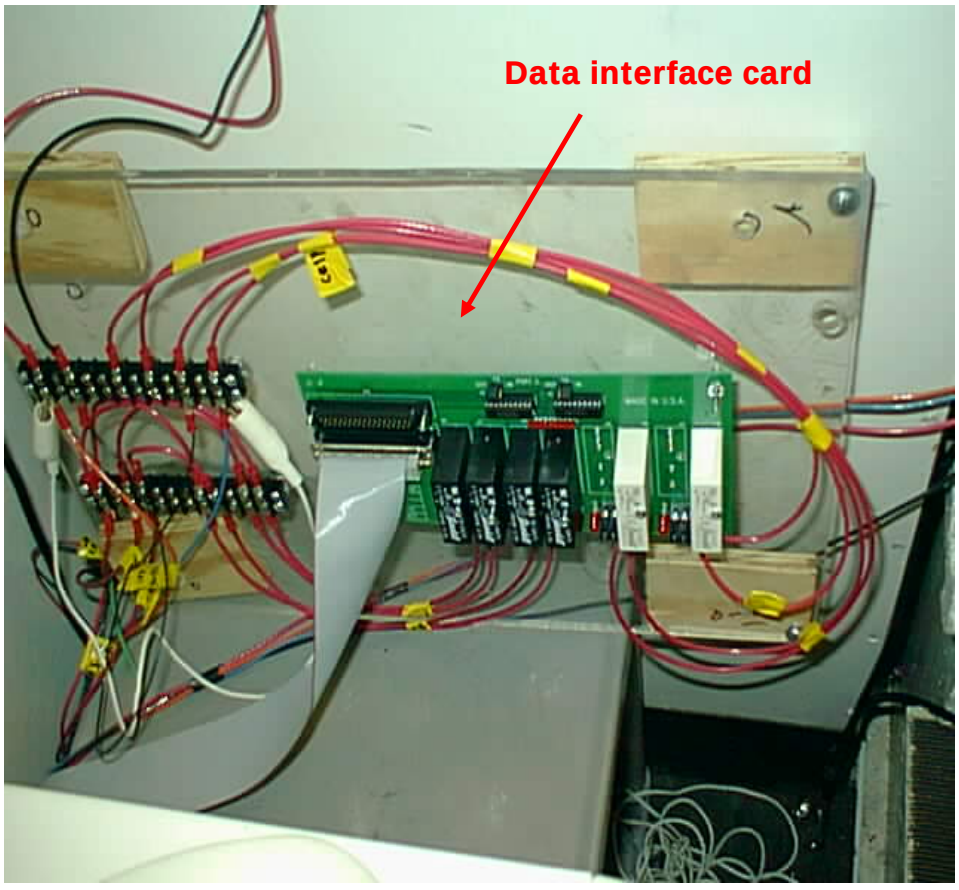

Fig. 2.17. Digital data interface card (PCI-DIO24™ manufactured by Measurement Computing Corporation), which was used for data collection and blower control.

2.4. RADIATION MONITORING SYSTEM

2.4.1. Paired Ion Chamber Method

Radiation biology experiments require determination of both the neutron spectrum, and the absorbed dose due to neutrons and gamma rays. To assure that neutron dose to the samples is delivered with photon dose contamination of less than 5%, we need to monitor the total and the neutron dose rates in the exposure cave during normal operation with the paired ion chamber method (ICRU 1971). To accomplish this task, tissue equivalent and graphite ion chambers were constructed as shown in Fig. 2.18. For total dose monitoring, a propane filled chamber made of tissue equivalent plastic (i.e., A-150 tissue equivalent plastic, 1.27 cm in diameter), with guard electrodes around the copper collecting electrode, was used. Graphite is usually considered as an air-equivalent material and has a minimal neutron absorption cross-section. For photon dose monitoring, the wall of the second ion chamber was made with graphite, 1.27 cm in diameter, and argon gas was used as the fill gas to minimize neutron response.

To determine the detector operating voltage, the detector readings were monitored with increasing applied voltage while exposing the detectors at 1 Gy/min (250 kVp and 10 mA) with an x-ray machine (Norelco MG300) at the Texas A&M Nuclear Science Center as shown in Fig. 2.19. The upper region of the operating voltages was chosen due to the higher ionization density along tracks of secondary particles produced by neutrons (ICRU 1977). These detectors were, then, calibrated with the Picker Co-60 teletherapy source at the Texas A&M School of Veterinary Medicine as shown in Table 2.2.

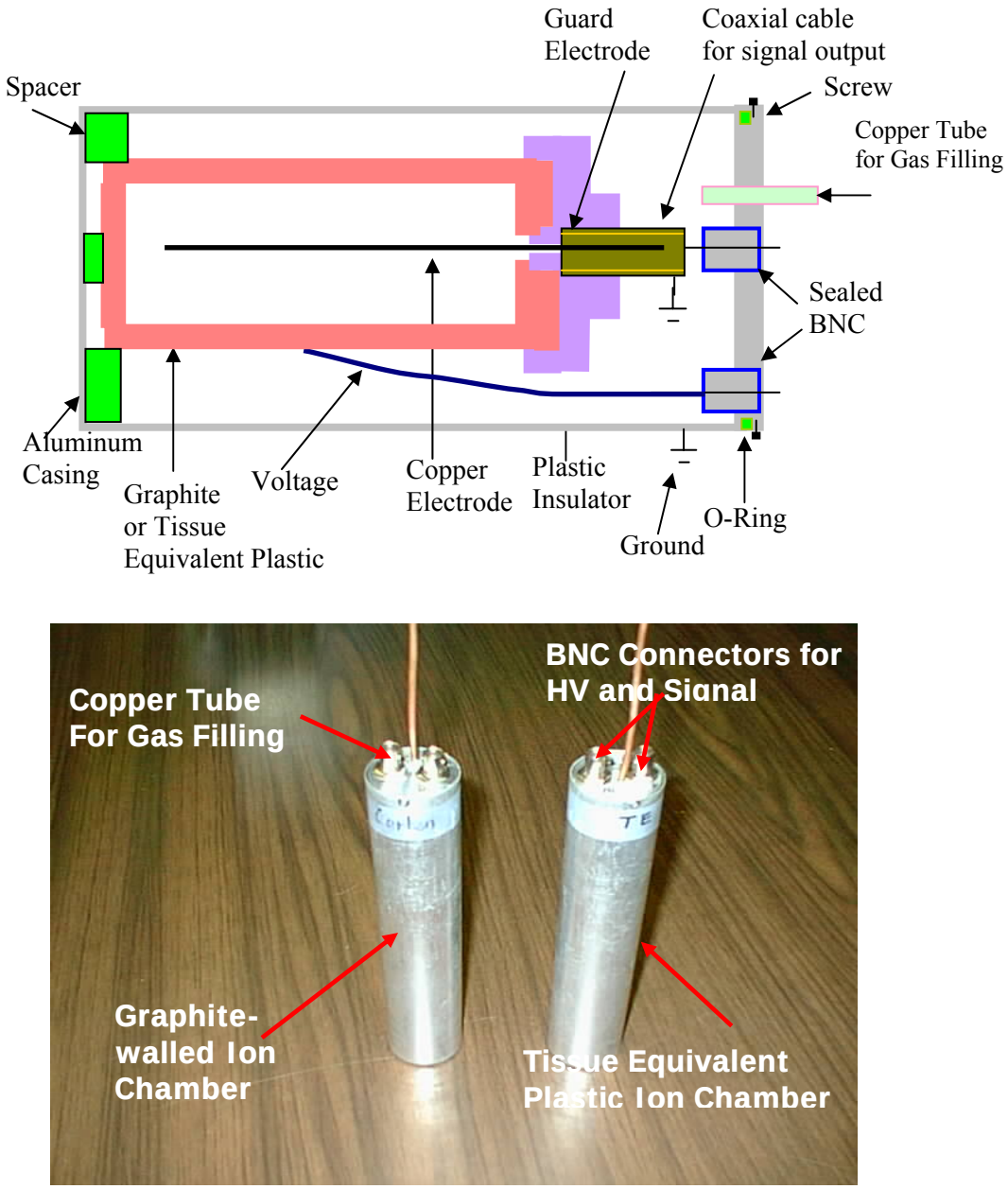

Fig. 2.18. Design scheme and top/side views of the tissue equivalent and graphite-walled ion chambers used in this study

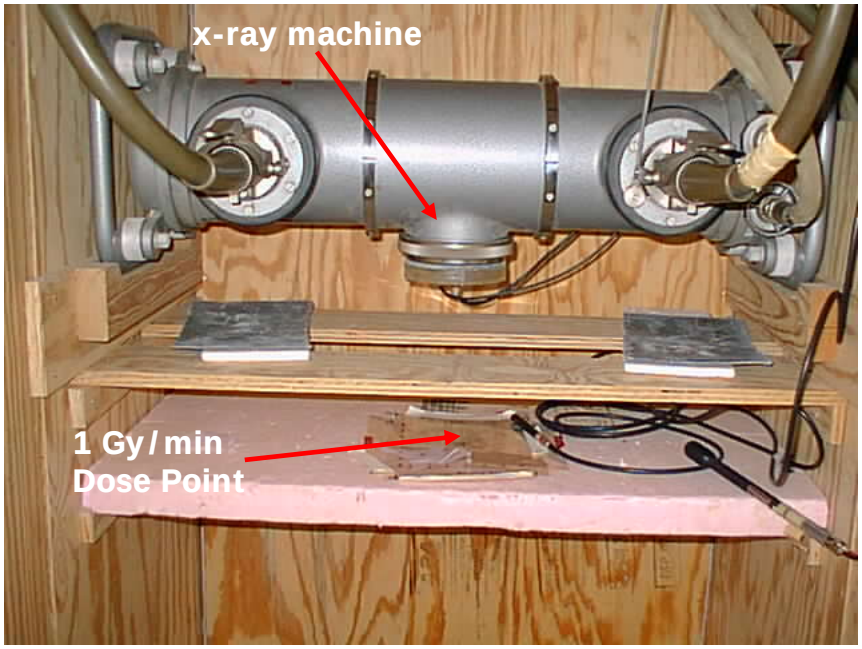

Fig. 2.19. X-ray machine (Norelco MG300) of the Texas A&M Nuclear Science Center used for determining operating voltage, which set at 250 kVp and 10 mA.

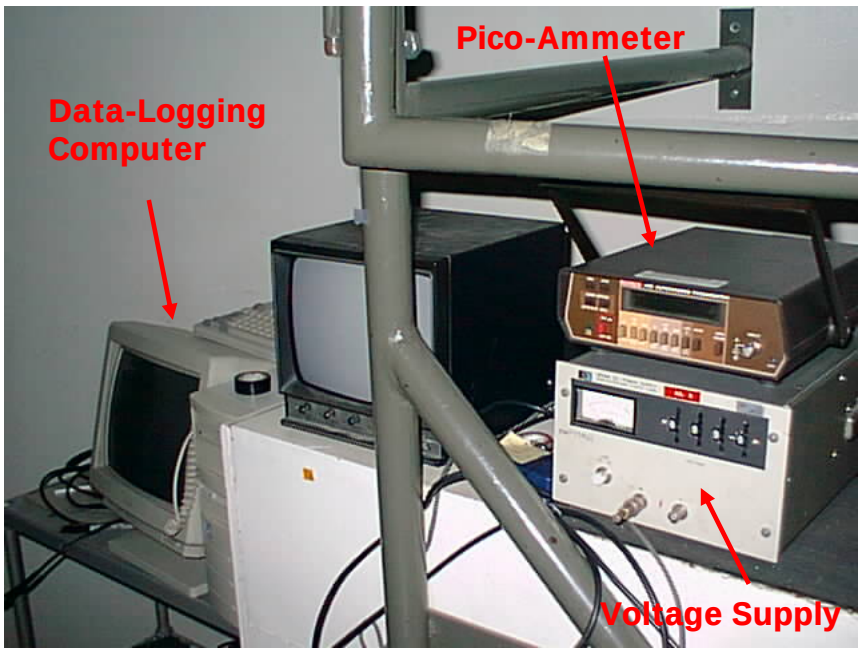

Fig. 2.20. Keithley™ 485 Auto-ranging Pico-ammeter, Hewlett Packard™ HP6516A DC Power Supply used in this study.

The central collecting electrode of the detector was connected to a Keithley™ 485 Auto-ranging Pico-ammeter for the graphite-walled ion chamber and to a Keithley™ 6487 Auto-ranging Pico-ammeter for the tissue equivalent plastic-walled ion chamber, respectively, and the outer wall of the detector was linked to the DC power supply of the Hewlett Packard™ HP6516A as shown in Fig. 2.20. Negative voltage was applied to the detector wall to play a role as a cathode. A computer was used to display the measured dose rates based on the calibration factors and to log the measured data for future use. The detectors were inserted into aluminum casings, which were grounded to protect the internal parts from any electrical and physical impacts. A small copper pipe as shown in Fig. 2.18 was installed on top of the aluminum casings to fill the detectors with their respective gas. The gas filling system has a vacuum pump and valves as shown in Fig. 2.21 that can be used to fill a detector to any pressure from atmospheric to about 5 Torr. After making sure that the detectors are vacuum tight, then the detectors were filled with gas of interest to 760 Torr through the 0.32 cm-diameter copper tube. When filled the gas of interest, we used a special tool to pinch off the tube to make a vacuum tight seal. Fig. 2.22 shows the characteristics of the tissue equivalent and carbon-walled ion chambers with varying voltages.

Since the leakage current should be minimized to measure pico-ampere level events, a coaxial cable was directly inserted into the insulating plastic and connected into the collecting electrode in order to act as a cable for signal output, as well as a guard electrode. Regarding the detection sensitivities of the detectors, the leakage current of each detector was measured with the Keithley™ 485 Auto-ranging Pico-ammeter

without any external radiation source, and then the minimum dose rate, which the detector can measure, was calculated as follows (Knoll 2000);

$$D = \frac{fI_l wS_m}{V\rho(\frac{T_0}{T})(\frac{P}{P_0})} \quad (2\text{-}1)$$

Where, D is the absorbed dose rate of tissue in Gy/min, I_l is the leakage current in pico-ampere, f is the conversion factor, w is the average energy loss per ion pair produced in the given gas (eV/ion pair), S_m is the relative mass stopping power of the tissue to that of the given gas, V is the detector volume in m^3, ρ is the density of the gas at STP in kg/m^3, P_0 and T_0 are standard pressure and temperature (i.e., 760 Torr and 273.15 K), and P and T are gas pressure and temperature. Both of the detectors showed the leakage current (I_l) of less than 1 pA (usually, 0.3 pA), and the sensitivity level for dose rate in tissue was calculated as less than 0.2 cGy/min.

Table 2.2. Calibration factor for the paired-ion chambers used in this study.

Detector	Dose Rate for Calibration (cGy/min)*	Detector Response (pA)	Calibration Factor (cGy/min-pA)
Carbon-walled	5.31×10^{1}	$7.07\times10^{-1}\pm5.77\times10^{-4}$	$7.55\times10^{1}\pm6.17\times10^{-2}$
	2.65×10^{2}	$3.35\times10^{0}\pm8.54\times10^{-4}$	$7.92\times10^{1}\pm2.02\times10^{-2}$
Tissue Equivalent	5.31×10^{1}	$6.11\times10^{-1}\pm5.77\times10^{-4}$	$8.74\times10^{1}\pm8.26\times10^{-2}$
	2.65×10^{2}	$2.83\times10^{0}\pm1.00\times10^{-3}$	$9.38\times10^{1}\pm3.31\times10^{-2}$

* Dose rate in tissue measured at 0.5 cm below of the water tissue.

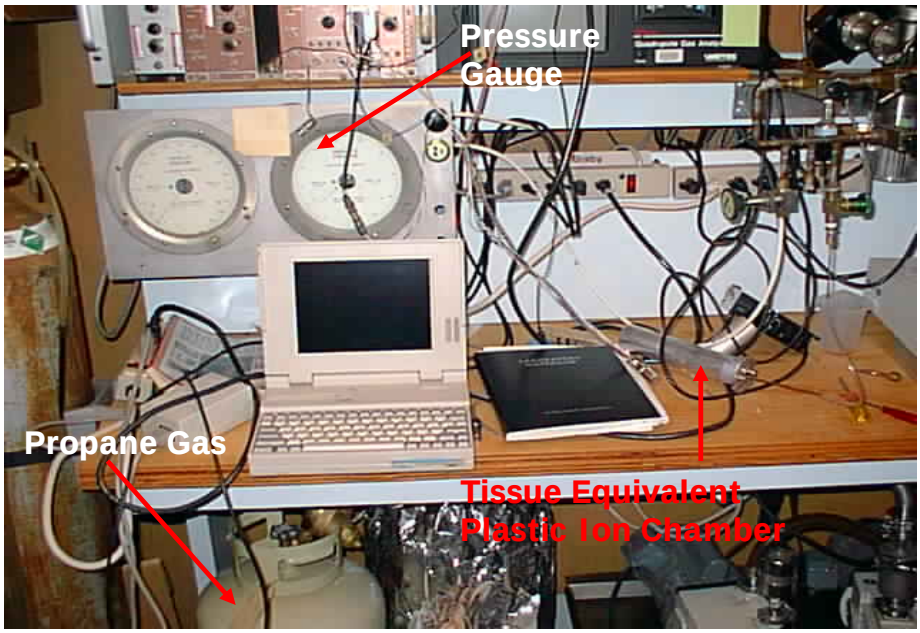

Fig. 2.21. Gas-filling system used in this study for filling argon and propane gas into graphite and tissue equivalent plastic ion chambers, respectively.

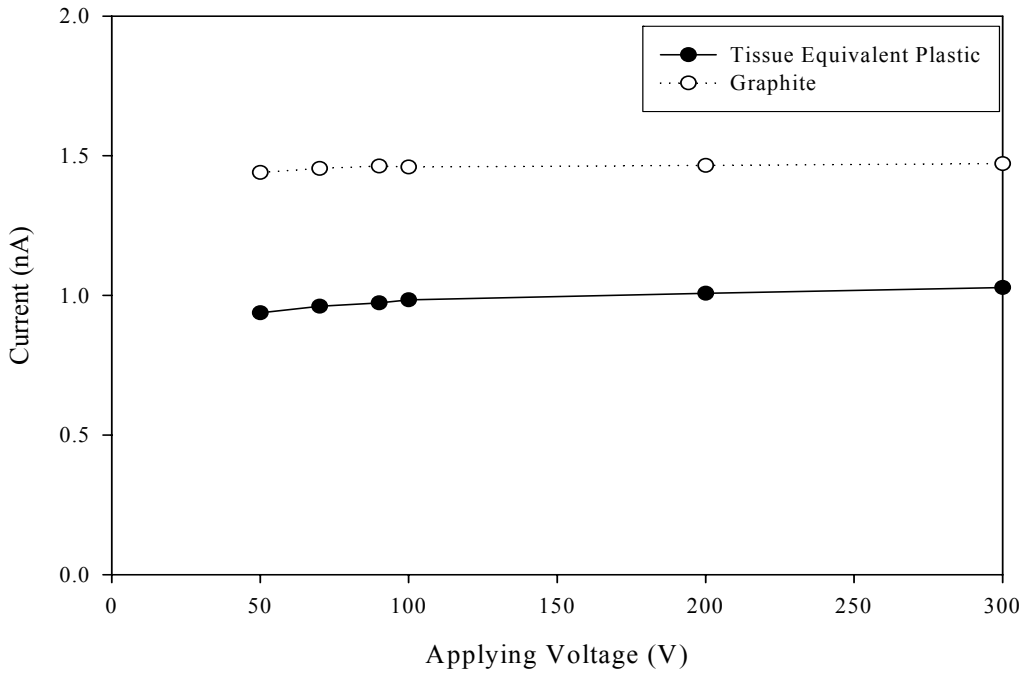

Fig. 2.22. Measured current with varying voltages for setting the operating voltages of the detectors used in this study.

In a mixed radiation field such as the irradiation cell at the NSCR, the paired ion chamber method described in the ICRU-26 (ICRU 1977) can be used to evaluate the separate absorbed doses of neutrons and of photons as mentioned in the previous paragraph. The tissue equivalent ion chamber, denoted by "T" subscript in the following equations, was used to measure responses from neutrons, as well as from photons. On the other hand, the graphite-walled ion chamber, denoted by "U" subscript in the following equations, was used to measure responses mainly from the photons with a lower sensitivity to neutrons. The responses of the tissue equivalent and graphite-walled ion chambers in dose rate, which were measured with the calibration factors to the gamma rays used for the detector calibration, can be denoted as $R_T^{'}$ and $R_U^{'}$, respectively, and then these values can be related with the absorbed doses in tissue of neutrons and of photons as follows (ICRU 1977);

$$R_T^{'} = k_T D_N + h_T D_G \tag{2-2}$$

$$R_U^{'} = k_U D_N + h_U D_G \tag{2-3}$$

Where D_N and D_G are the absorbed dose rates in tissue of neutrons and of photons in the mixed radiation field, k_T and k_U are the ratios of the responses of the detectors to the neutrons to the responses of the detectors to the gamma rays used for the calibration, and h_T and h_U are the ratios of the responses of the detectors to the photons in the mixed radiation field to the responses of the detectors to the gamma rays used for the calibration. Assuming that h_T and h_U are close to unity, the absorbed dose rates in tissue

of neutrons and of photons in the mixed radiation field (i.e., D_N and D_G) can be obtained by

$$D_N = \frac{R_T^{'} - R_U^{'}}{k_t - k_U} \tag{2-4}$$

$$D_G = \frac{k_t R_U^{'} - k_U R_T^{'}}{k_t - k_U} \tag{2-5}$$

2.4.2. Stainless Steel-Walled Ion Camber

Two stainless steel-walled ion chambers were, in addition, used to monitor gamma dose rates inside the irradiation cell without the FNIS. These detectors were manufactured by the LND Inc. for high gamma dose monitoring purpose. Since these detectors are filled with nitrogen at 100 Torr, they are not applicable for a mixed radiation field, which results in a high neutron dose rate compared with the gamma dose rate, due to the capture reactions of the nitrogen with neutrons such as (n, p) and (n, α) reactions. However, they can be applicable for monitoring gamma dose rates in the case of comparable magnitude of the photon dose compared to the neutron dose such as the irradiation cell without the FNIS. By comparing the calculated neutron responses of two different types of filling gases (i.e., nitrogen and tissue equivalent gas) with the measured responses, we can subtract the neutron contribution to the reading, and obtain a better estimate of the photon dose rate.

2.4.3. Activation Foil Method for Determining Neutron Spectra

To characterize the neutron energy spectra inside the exposure cave, foil activation method was used with a bare aluminum-gold foil and 10 cadmium-covered activation foils (Al, Fe, Au, Ni, Ti, Zn, In, Co, Mg, and Cu) with different threshold energies that cover the energy range from thermal neutrons to 13 MeV as shown in Table 2.3. In order to characterize fast neutrons effectively, all of the foils were covered with cadmium plates to cut off thermal neutrons as shown in Fig. 2.23. Thermal neutrons were measured with bare aluminum-gold foil. After exposing the foils with the NSCR against the irradiation cell with and without the FNIS, the foils were counted with a HPGe spectroscopy system to measure specific activities at the end of irradiation. The flux foils ranged in thickness from 0.0375 mm to 0.125 mm to minimize the flux perturbation and self-shielding effects of the foils (Schumacher and Randall 1975). Although all of the foils were cut to less than 1 cm diameter, the spatial resolution of the flux foil sets is limited due to the larger size of the set, as shown in Fig. 2.23. Therefore, the flux foils were used to obtain average neutron spectra over a region of interest.

The SAND (Spectrum Analysis by Neutron Detectors)-II code (Griffin and Kelly 1994), a spectrum deconvolution code, was used to determine a full energy spectrum from the measured specific activity data of the foils. A solution acceptance criterion of 10% was used to obtain neutron spectra using the measured specific activities of flux foils i.e., the SAND-II results were considered as acceptable if the standard deviation of the measured-activity to the simulated-activity ratio was less than 10%.

Table 2.3. Characteristics of the flux foils in terms of neutron reaction.

Element	Reaction	Half-Life	Threshold Energy (MeV)
Manganese	$^{24}Mn(n,p)^{24}Na$	15.0 h	6.0
Aluminum	$^{27}Al(n,\alpha)^{24}Na$	15.0 h	4.9
Iron	$^{56}Fe(n,p)^{54}Mn$	2.56 h	0.85
	$^{58}Fe(n,\gamma)^{59}Fe$	44.6 d	1.1
	$^{54}Fe(n,p)^{54}Mn$	2.56 h	0.84
Cobalt	$^{59}Co(n,\gamma)^{60}Co$	5.28 y	Resonance Reaction
Nickel	$^{58}Ni(n,p)^{58}Co$	71.3 d	1.4
	$^{60}Ni(n,p)^{60}Co$	5.28 y	2.5
Copper	$^{63}Cu(n,\gamma)^{64}Cu$	12.7 h	Resonance Reaction
	$^{63}Cu(n,\alpha)^{60}Co$	5.28 y	5.5
Zinc	$^{64}Zn(n,p)^{64}Cu$	12.7 h	2.0
Indium	$^{115}In(n,2n)^{115m}In$	4.50 h	0.5
Gold	$^{197}Au(n,\gamma)^{198}Au$	2.695 d	Resonance Reaction
Titanium	$^{46}Ti(n,p)^{46}Sc$	83.8 h	2.4
	$^{47}Ti(n,p)^{47}Sc$	82.32 h	0.24
	$^{48}Ti(n,p)^{48}Sc$	44.0 h	4.3

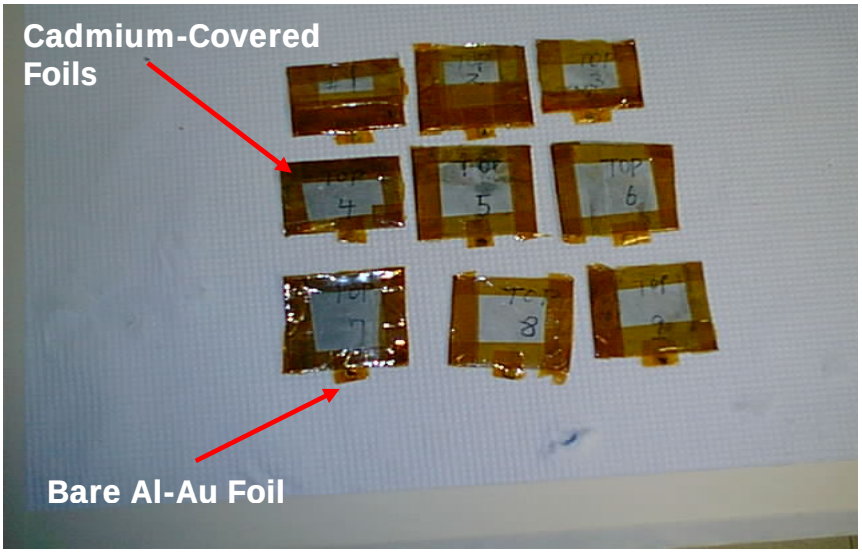

Fig. 2.23. Neutron activation flux foils, which consist of cadmium-covered foils such as Al, Fe, Au, Ni, Ti, Zn, In, Co, Mg, and Cu and a bare aluminum gold foil. Each foil packet is approximately 4 × 4 cm.

2.5. MONTE CARLO MODELING

2.5.1. Overview

The MCNP version 5 code with a set of ENDF/B-VI continuous neutron cross-section libraries was used to model the NSCR core against the irradiation cell at the full power operation (i.e., 1 MW). The MCNP model of the NSCR core itself had already been tested by comparing the calculated results with those of other approaches, i.e., (1) an in-house three-dimensional diffusion code (i.e., SUNMAN) and (2) foil activation measurement (Chen 1997; Kim et al. 2002). The neutron flux of the cell at 100 kW based on MCNP simulation and flux foil measurements agreed well and there was no systematic difference between the MCNP and flux foil results considering complexity of the NSCR core and various approximations made in the MCNP models (Jang et al. 2002). In addition, MCNP simulations with varying combinations of filters including different thickness have been performed for a feasibility study of performing boron neutron capture therapy (BNCT) with the irradiation cell of the NSCR, and combinations of filters have been simulated to deliver epithermal neutron beams into the cell (Jang et al. 2003). However, the above study was focused on relatively broad epithermal neutron beams for the BNCT. In this study, fast neutrons were modeled in detail with 1MeV energy intervals using the MCNP F4 tally for neutron flux and F6 tally for air dose rate inside the system.

2.5.2. Reactor Core Modeling

This study modeled the NSCR core in as much detail as possible, explicitly modeling

the core as shown in Fig. 2.24 except for the Sb-Be source, which is ignored due to its negligible effect on neutron flux. Fig. 2.25 shows a fuel element (left) and a fuel bundle (right) as modeled in this study. A fuel element has 38.1-cm long, 3.482-cm diameter active fuel section or fuel meat. The active fuel section contains a 0.4572-cm diameter zirconium rod at the center. The fuel section and top and bottom graphite slugs are contained in a 0.051–cm thick stainless steel cladding. Top and bottom fittings of a fuel element are made of stainless steel. A fuel bundle consists of an aluminum top handle, four rods and an aluminum bottom adaptor. The four rods in a bundle can be four fuel elements, three fuel elements + an instrumented fuel element, three fuel elements + a control rod, or two fuel elements + two water elements as shown in Fig. 2.24. The top handle consists of a handle, a locking plate and a locking bolt. The bottom adaptor has a shape to fit into the grid plate and the top of the adaptor contains four tapped holes into which fuel rods are threaded. The details of these complicated top handle and bottom adaptor were not explicitly modeled in this study.

The NSCR core utilizes FLIP (Fuel Life Improvement Program) type fuel, in which zirconium hydride moderator ($ZrH_{1.65}$) is homogeneously combined with 8.5 weight % of uranium (70% enriched in ^{235}U) and approximately 1.5 weight % of erbium (as burnable poison) for new fuel. Currently, the fuel bundles in the NSCR core contain 67-84% of their original content of ^{235}U. In this study, the fuel bundles in the core were divided into three groups according to their ^{235}U depletion levels. Then, all the fuel elements in the same group were assumed to have the same amount of ^{235}U. The vertical variation of fuel depletion was modeled based on the vertical variation of thermal

neutron flux in the NSCR core. To incorporate the vertical variation of fuel burn-up, the fuel meat section of a fuel element was divided into five segments as shown in Fig. 2.25 and the concentrations of ^{235}U and ^{167}Er were determined for each of these segments. In this study, only ^{167}Er concentration was determined for the depletion of burnable poison since ^{166}Er concentration does not change much over the lifetime of the fuel due to its small neutron absorption cross-section.

In this study, we did not explicitly model the fission product in the NSCR core due to the lack of a detailed inventory. A rough approximation was made. First, the fission products in the NSCR core were represented by so-called “average fission product” (Briesmeister 2003; Foster and Arthur 1982). The "average fission product" is a pseudo-fission product that has a lump fission product cross-section representing the cross-sections of the fission products that are produced from one ^{235}U fission. The concentration of the “average fission product” in the reactor core was then determined by repeating criticality calculations; that is, the concentration of the “average fission product” was adjusted to make the reactor critical for a given critical condition of the irradiation cell run (i.e., shim safety rods at 80%, transient rod at 100%, and regulating rod at 50%).

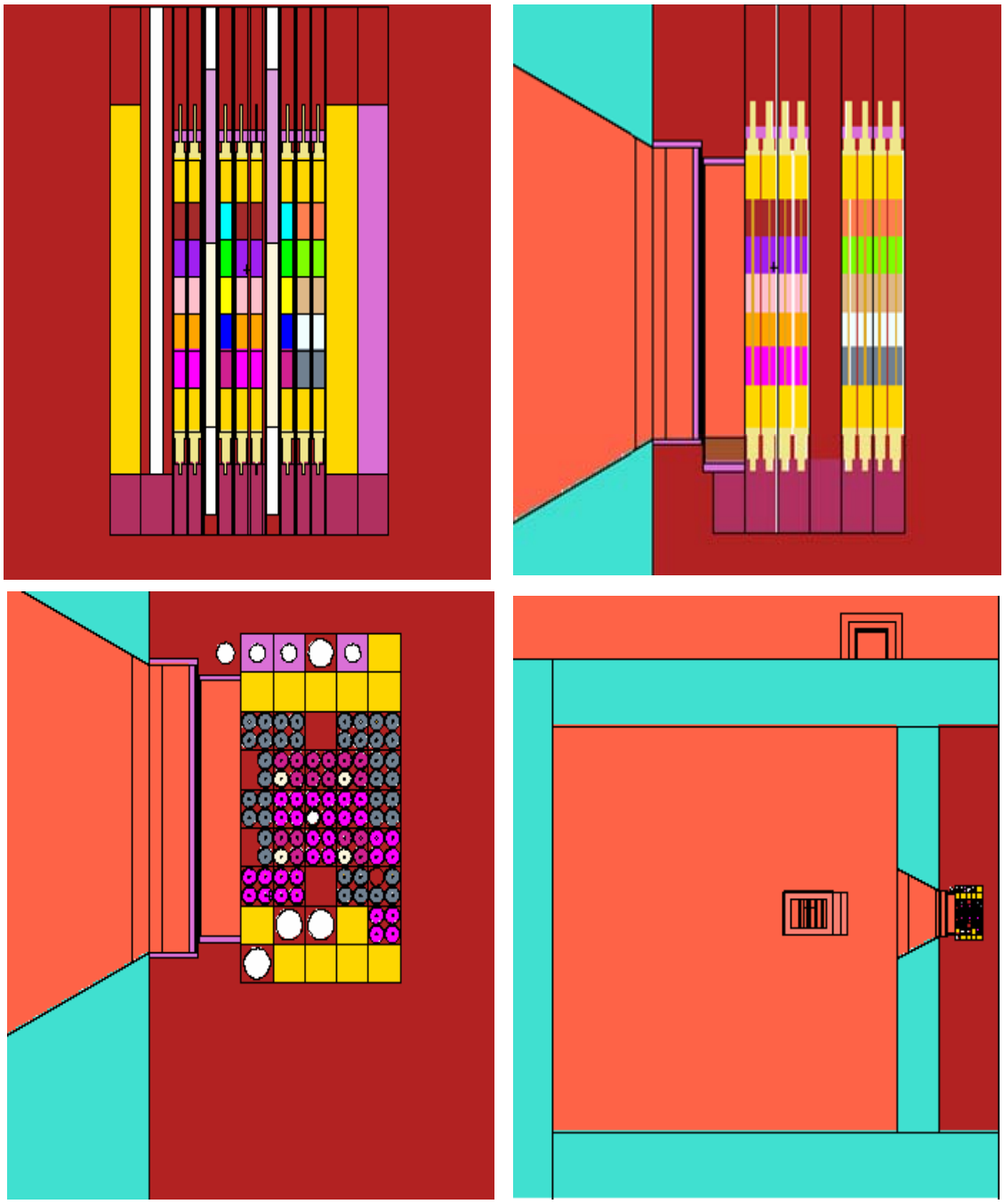

Fig. 2.24. MCNP drawings denoting NSCR, void box, cell window, irradiation cell, and the exposure cave on x-y plane, y-z plane, and x-z plane.

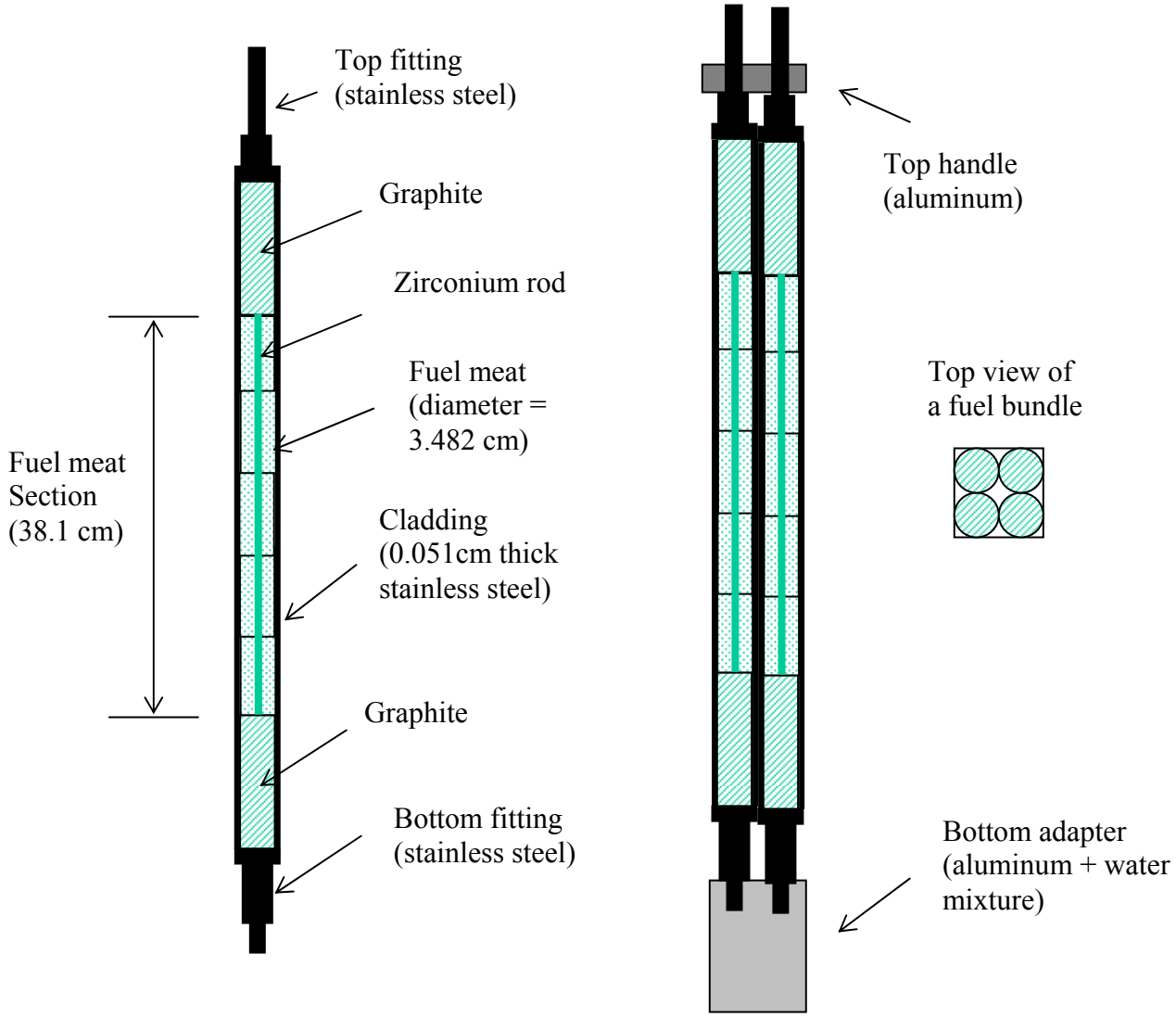

Fig. 2.25. Fuel element and fuel bundle as modeled in this study. Note that the fuel meat section is divided into 5 segments and this study calculates neutron flux in each of these five segments (Kim et al. 2002).

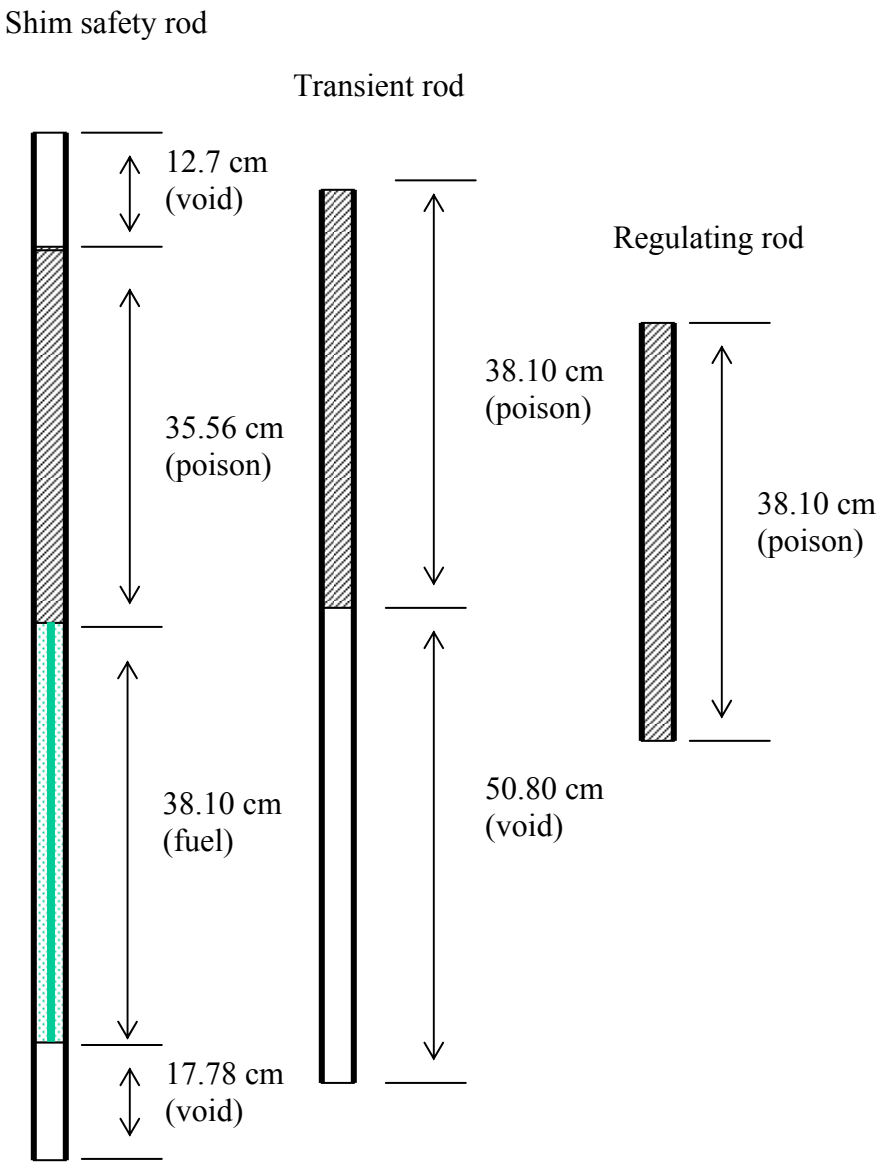

Fig. 2.26. Monte Carlo modeling of control rods as modeled in this study (Kim et al. 2002).

The reactor power is controlled by a total of six control rods (4 shim safety rods, a regulating rod, and a transient rod). Fig. 2.26 shows the control rods as modeled in this study. A shim safety rod, which has scram capability, consists of a poison section, a fuel section and two void sections on the top and bottom. The poison in the shim safety rod is borated graphite (B_4C 25% and graphite 75% by weight). The diameter of the poison is 3.3909 cm and the thickness of the stainless steel (SS304) clad is 0.508 cm. The fuel section is almost identical to a regular fuel rod except that the fuel meat is 3.39090 cm in diameter. The transient rod, which is used for reactor pulsing and has scram capability, consists of a poison section and a void section. The poison used in the transient rod is also borated graphite. The diameter of the poison is 3.03276 cm and the thickness of the stainless steel (SS304) clad is 0.00712 cm. The regulating rod, which is used for 'servo' control of reactor power, is composed of a poison section. The rod size is the same as the transient rod. The only difference is that the poison in the regulating rod is pure B_4C powder. These shim safety rods, transient rod and regulating rod were raised to 80%, 100% and 50%, respectively, to model the reactor against the irradiation cell at the critical condition of 1-MW operation.

This study did not model the Sb-Be source, which is located at C8 in Fig. 2.12 due to its negligible effect on neutron flux. The power monitoring detectors and pneumatic devices were modeled as void space. The grid plate, which is made of aluminum with 54 holes, was modeled as a homogenous mixture of aluminum (84 weight %) and water (16 weight %). The reactor core was modeled as surrounded by water gap in the opposite side of the irradiation cell, which is big enough to account for full neutron scattering in

water.

To model fuel meat sections, this study used the ENDF/B-VI neutron cross-section data which were evaluated at high temperatures (558°K or 600°K). These high-temperature cross-section data were obtained from the Korean Atomic Energy Research Institute (KAERI). The average temperature in the fuel elements (when the reactor is operating at 1 MW) is approximately 550°K and, therefore, the neutron cross-section data were adjusted for the temperature differences using TMP cards in MCNP. For other part of the reactor core, this study used the standard ENDF/B-VI cross-section data that were evaluated at 300°K. The slow neutron scattering law S(α, β), which was evaluated at 300°K or 600°K as appropriate, was used to account for the molecular binding effects in ZrH, water and graphite.

2.5.3. Irradiation Cell Modeling Including the FNIS

In the pool side, a stainless steel (Type 304) liner is installed in the reactor pool for water containment and water purity. However, there is no steel liner inside the irradiation cell. The upper 5.2 m of the wall is made with the standard concrete, and the lower portion of the wall is barites concrete and light concrete (NSC 2003). Therefore, the wall of the irradiation cell has a good capability for reactor experiments in terms of neutron and gamma ray shielding with the maximum reactor power of 1 MW. There is, however, a penetration of 50 cm by 30 cm size for cooling water piping and electrical cables, and therefore additional shielding around the penetration is necessary for further dose reduction in the upper research level. The penetration on top of the cell will be used

for sample loading and unloading as described in the Section 2.3. This study did not model the penetration of top of the cell. Although there are several steel H-beams in the cell for structural integrity and there are unused cooling components, it was not modeled in this study. Fig. 2.27 shows the MCNP drawings denoting the exposure cave, movable steel table, extra lead bricks, aluminum plates, and cell window.

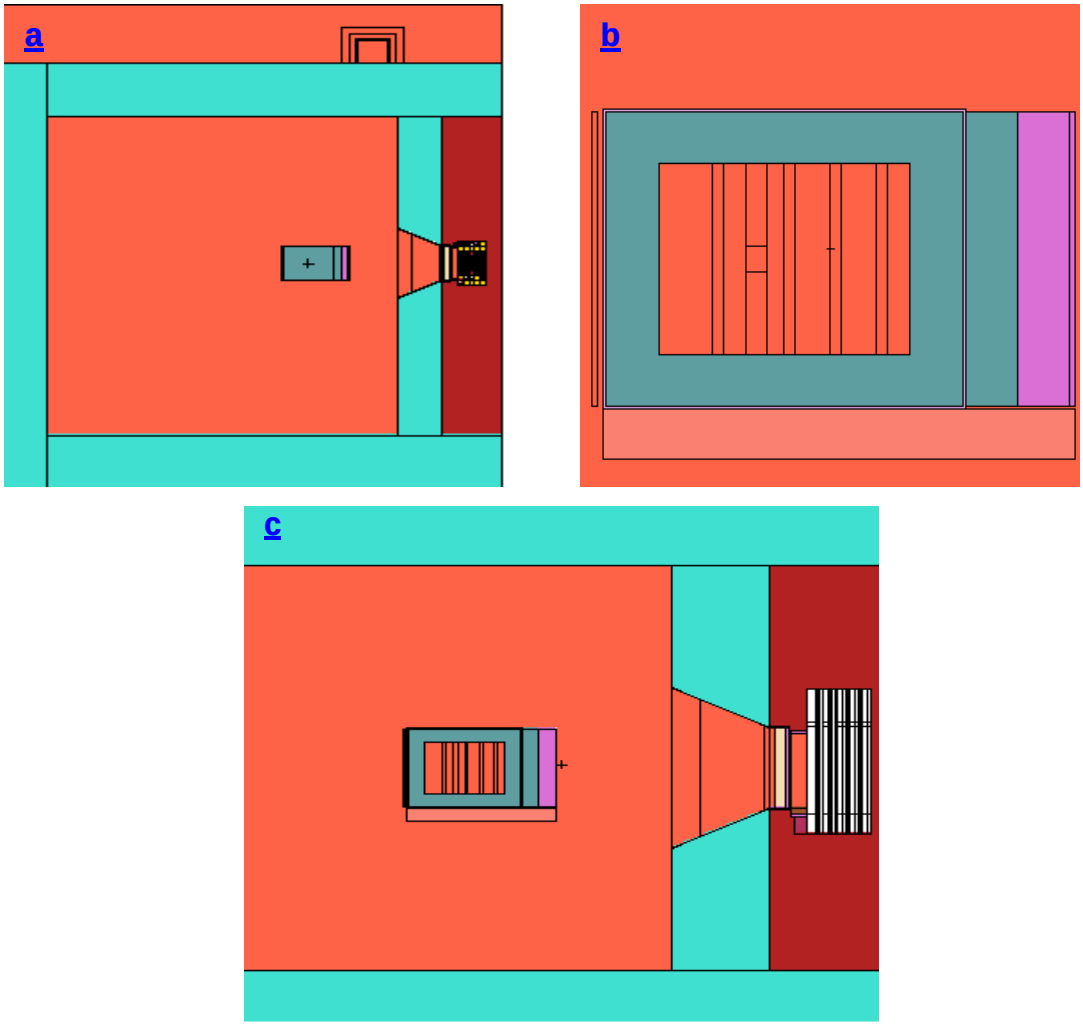

Fig. 2.27. MCNP drawings denoting exposure cave surrounded by a boral box, a movable steel table, a cell window, and the walls of the irradiation cell on a) x-y plane, b) y-z plane, and c) x-z plane.

2.5.4. Criticality and Fluence Calculation

In this study, the FNIS including the reactor core and the irradiation cell was modeled in detail with the 3-D computational model at the full power operation to evaluate the performance of the system. Criticality calculations were performed using the KCODE card in MCNP. This study used 10,000 neutron histories and/or 15,000 for detail simulation purpose per each of 200 cycles (50 settling cycles + 150 active cycles) for criticality calculations. Criticality calculations were repeatedly performed using the KCODE card in MCNP to make the reactor critical for a given condition. The KCODE mode calculates the nuclear criticality in a given system characterized by k_{eff}, which is the ratio between the number of neutrons in successive generations (Briesmeister 2003). Calculating nuclear criticality, k_{eff}, consists of estimating the mean number of fission neutrons produced in one generation, including initial guess of the nuclear criticality. To run the KCODE, the user needs to provide the nominal number of source histories per each criticality-calculation cycle, an initial guess of $k_{eff,}$ the number of source cycles to skip before k_{eff} accumulation, and the total number of cycles in the run.

Typical run time was roughly 1200 minutes per each run with a computational server at the Department of Nuclear Engineering. Although we need to use more neutron histories to reduce statistical disturbances in the MCNP runs, it results in huge computation time to get the final results. Therefore, two different histories mentioned above were selectively chosen based on the simulation purpose. For the initial source distribution, the KSRC card was used with 5 source points in each of the fuel elements. The criticality calculations were repeated adjusting the concentration of the "average

fission product" in the NSCR core to make the reactor critical for a given critical condition (i.e., shim safety rods at 80%, transient rod at 100% and regulating rod at 50%). Although several irradiation devices could be modeled on the reactor core model to calculate neutron flux in these devices, this study did not include any devices such as the fast flux irradiator (FFI) and long tubes.

After the reactor was made critical, neutron and photon flux in the exposure cave were calculated. Since the MCNP code has no capability to simulate delayed gamma rays produced by radionuclides, which are produced by neutron capture reaction with steel frames and aluminum window of the irradiation cell, the photon flux of the MCNP results is due to fission in the reactor core and capture gamma rays. However, the MCNP results do not underestimate the total photon fluence by a large factor because the dose contribution from the radionuclides produced by capture reactions are not dominant compared with those of fission and capture gamma rays (Ross et al. 1993). In this study, fast neutrons in the irradiation cell were modeled in detail with 1MeV energy intervals from 1 MeV to 10 MeV using the MCNP F4 tally for neutron flux and F6 tally for air dose rate inside the system.

2.5.5. Absorbed Dose Rate Calculation

The kerma rate in tissue at a point in space is useful in preliminary planning of radiation therapy and of radiobiology experiments (ICRU 1969). Kerma can be determined with ion chambers, which have a wall thickness sufficient for establishing charged particle equilibrium. Since the paired ion chambers mentioned in the Section

2.5.3 were designed such that the radiation field would not unduly disturbed, we can consider the dose rates measured by the detectors as kerma rates. For determining the absorbed dose at any point in the tissue, we can use the kerma rate in a two-step process (ICRU 1969). First, the dose profile is determined in a phantom placed in the neutron field. Second, a normalizing factor is used to relate the absorbed dose at any point in the tissue to the neutron fluence at a point in the free space. This normalizing factor can be obtained by the kerma in free space, which can be obtained from a measurement at the same point in air before the sample is placed.

Tissue kerma rate in air of neutrons was calculated with the simulated neutron flux of the MCNP and neutron kerma factors stated in the ICRU-26 (ICRU 1977). The ICRU-26 publication provides four different kerma factors such as tissue approximation, tissue equivalent plastic (i.e., A-150 tissue equivalent plastic), ICRU muscle, and standard man. All of these factors were used to calculate neutron tissue kerma rate in air. The tissue kerma rate in air of neutrons can be calculated as follows;

$$D_{tissue}^{n} = \int_{0}^{\infty} fk(E)\phi(E)dE \tag{2-6}$$

Where D_{tissue}^{n} is tissue kerma rate in air of neutrons in Gy/min, f is conversion factor, $k(E)$ is kerma factor for the specified neutron energy of "E" in Gy-cm^2, $\phi(E)$ is differential neutron flux calculated with the MCNP in neutrons/cm^2-sec-MeV. In this study, tissue kerma and absorbed dose were reported for the ICRU muscle (i.e., 10.2 w % H, 12.3 w % C, 3.5 w % N, 72.9 w % O, and 1.1 w % other elements) if not specified for any other purposes.

For the tissue kerma rate in air of photons, the mass transfer coefficient of tissue for photons (Attix 1986) was used to calculate the dose rate with the photon flux inside the exposure cave. The tissue kerma rate in air of photons can be calculated as follows;

$$D_{tissue}^{\gamma} = \int_0^{\infty} fEk(E)\phi(E)dE \tag{2-7}$$

Where D_{tissue}^{γ} is tissue kerma in air of photons in Gy/min, f is the conversion factor, E is the photon energy of interest in MeV, $k(E)$ is the kerma factor of the ICRU muscle for the specified photon energy of "E" in Gy-cm$^{2/}$kg-tissue, $\phi(E)$ is differential photon flux calculated with the MCNP in photons/cm^2-sec-MeV.

CHAPTER III

RESULTS AND DISCUSSION

3.1. SENSITIVITY ANALYSIS RESULTS

3.1.1. Impact of Lead-Bismuth Thickness on the Neutron Energy Spectra

A sensitivity analysis was performed to find the impact of the lead-bismuth alloy shield thickness on the neutron energy spectra using the MCNP code to calculate dose at a sample point, 122 cm away from the cell window in the irradiation cell. This study modeled the exposure cave installed in the irradiation cell, including a boral box surrounding the exposure cave, a boral plate in the pool side, and a void box in the NSCR core. Figs. 3.1 and 3.2 show the differential neutron energy spectra as a function of neutron energy and lead-bismuth thickness over all neutron energies and fast neutron energies, respectively.

As the thickness of the lead-bismuth alloy increases, the neutron energy spectra are shifted to lower neutron energies due to the elastic and inelastic scattering interactions of fast neutrons with the lead-bismuth alloy. The lead-bismuth alloy has a relatively linear inelastic scattering cross section with increasing energies of fast neutrons, and the contribution of slow neutrons to the total dose of neutrons is negligible compared to that of fast neutrons as shown in Fig. 3.3. It is, therefore, possible to produce distinctly different neutron energy spectra in terms of neutron dose and to bring these neutrons into the exposure cave of the FNIS in order to facilitate biology experiments.

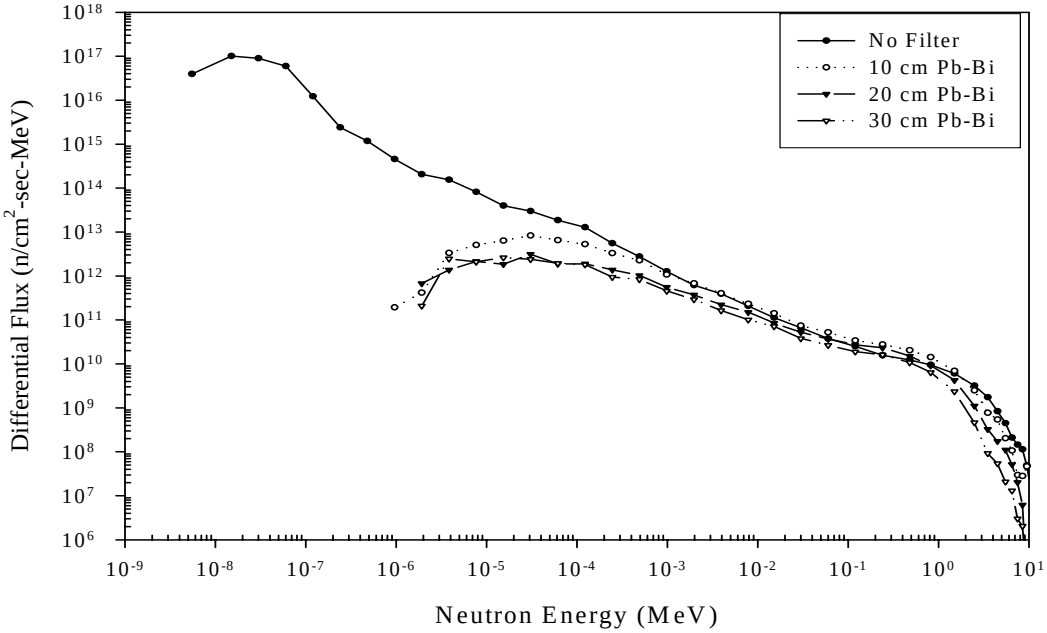

Fig. 3.1. Differential neutron flux over all neutron energies with varying thickness of lead-bismuth alloy, including a void box, a boral plate, and a boral box.

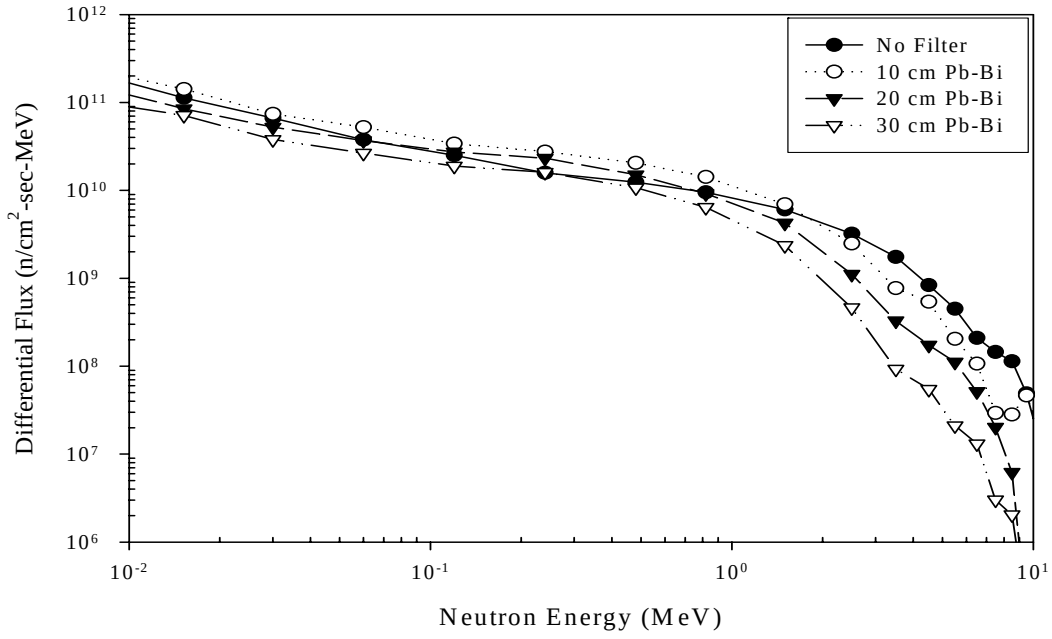

Fig. 3.2. Differential neutron flux for fast neutron energies with varying thickness of lead-bismuth alloy, including void box, boral plate, and boral box.

Figs. 3.3 and 3.4 show the fractions of the neutron flux and of the neutron tissue kerma rate in air as a function of neutron energy and of lead-bismuth thickness. Although the fractions of neutron flux were dominant at thermal and fast neutron energy regions, the tissue kerma rates in air of neutrons were negligible for neutrons with energies of less than 0.01 MeV due to relatively small kerma factors of thermal and epithermal neutrons compared with those of fast neutrons. However, since thermal and epithermal neutrons produce capture-gamma rays through the (n, γ) interactions with surrounding materials, these slow neutrons should be minimized using neutron absorbing materials such as boron, which is contained in the boral plate, regardless of the neutron contribution to total dose.

Fig. 3.5 gives the mean neutron energies ($\overline{E}_n$, $\overline{E}_{TK}$) as a function of lead-bismuth thickness, which are weighted by the neutron flux and by the tissue kerma rate in air of neutrons, respectively. The mean neutron energies ($\overline{E}_n$, $\overline{E}_{TK}$) are calculated in two ways: $\overline{E}_n$ is weighted by the neutron flux and $\overline{E}_{TK}$ is weighted by the tissue kerma rate in air of neutrons.

$$\overline{E}_n = \frac{\int_0^\infty E^2 \phi(E) d\log(E)}{\int_0^\infty E \phi(E) d\log(E)} \tag{3-1}$$

$$\overline{E}_{TK} = \frac{\int_0^\infty E^2 \dot{K}(E) d\log(E)}{\int_0^\infty E \dot{K}(E) d\log(E)} \tag{3-2}$$

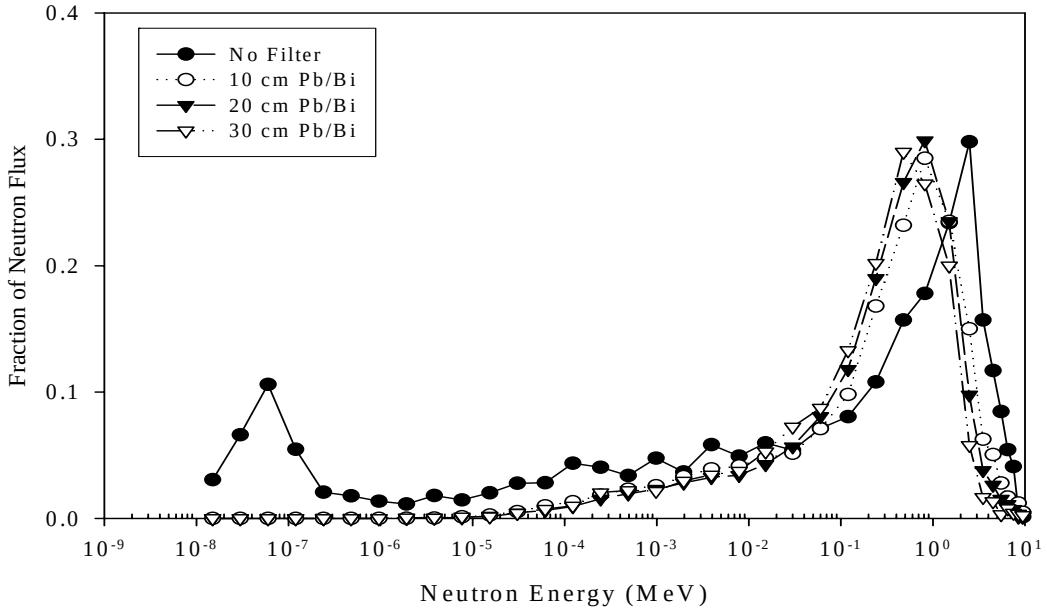

Fig. 3.3. Fraction of neutron flux over all neutron energies with varying thickness of lead-bismuth alloy, including a void box, a boral plate, and a boral box.

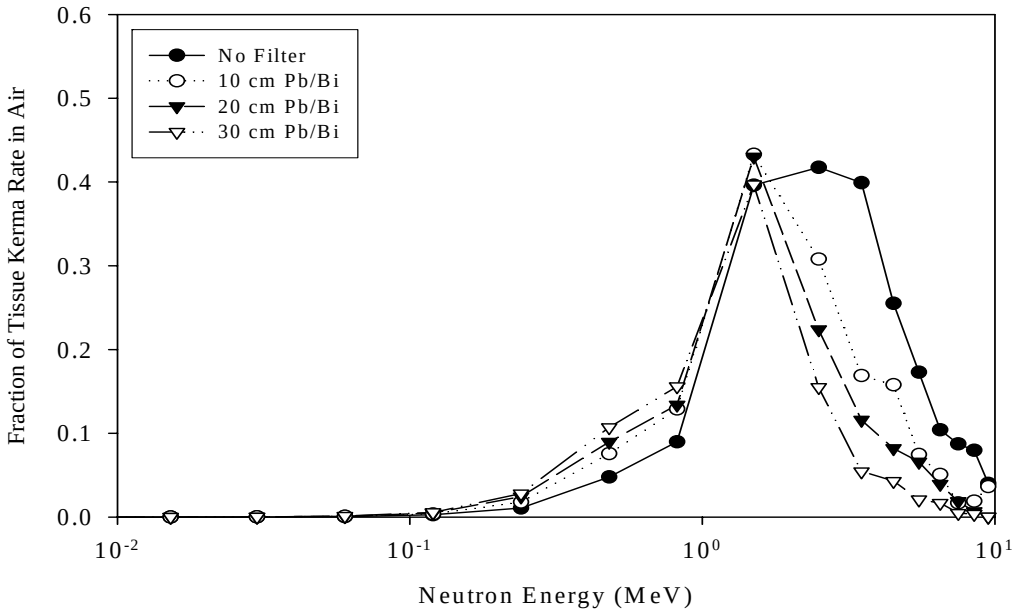

Fig. 3.4. Fraction of tissue kerma in air of neutrons with varying thickness of lead-bismuth alloy for fast neutron energies, including a void box, a boral plate, and a boral box.

Where $\phi(E)$ and $\dot{K}(E)$ are differential neutron flux in n/cm^2-sec-MeV and tissue kerma rate in air of neutrons in cGy/min-MeV, and E is the neutron energy of interest in MeV. The mean neutron energies ($\overline{E}_n$, $\overline{E}_{TK}$) weighted by the neutron flux and the tissue kerma rate in air were 1.10 MeV and 2.09 MeV without any lead-bismuth alloy in the FNIS, respectively. These values were reduced to 0.56 MeV and 1.03 MeV, respectively, with the 30 cm-thick lead-bismuth shielding due to the scattering interactions of incident fast neutrons with the lead-bismuth alloy. It was, therefore, found that the lead-bismuth alloy has a potential capability in delivering fast neutron beams with mean neutron energy of greater than 0.1 MeV with distinctly different energy spectra into the exposure cave of the FNIS in order to facilitate biology experiments.

Fig. 3.6 shows the photon contribution to the total dose with varying thickness of lead-bismuth alloy. The gamma contribution to the total dose decreased substantially from 45% to 2% by adding 10 cm-thick lead-bismuth alloy, and then smoothly decreased to less than 1% by adding 20cm-thick lead-bismuth alloy at the front face of the exposure cave. It was found that the lead-bismuth alloy is effective for gamma shielding with minimal fast neutron loss by capture reactions. The non-linear response shown in Figs. 3.5 and 3.6 is partly because of the (n, 2n) reactions of fast neutrons with the lead-bismuth alloy. Also contributing to the non-linear response was the design of the cave used in the computer simulations. Only its front face thickness was adjusted to the values in the figure. The side-walls, back and top were 10 cm in all cases. The selected exposure cave consists basically of 10 cm-thick lead-bismuth alloy at all sides, inside a boral box, with supporting materials such as steel angles and steel bands.

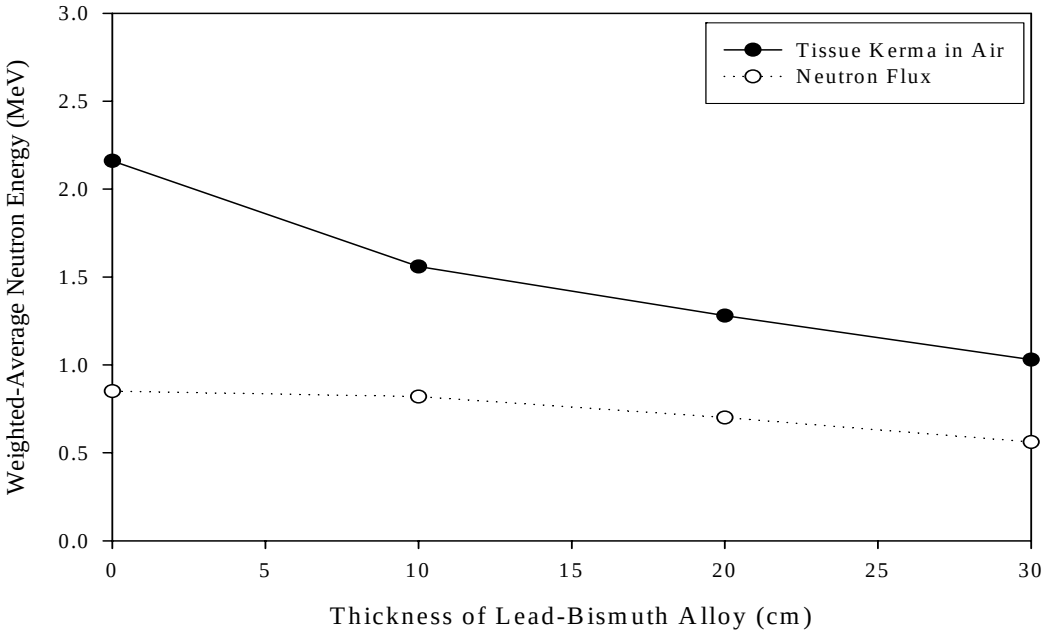

Fig. 3.5. Mean neutron energies of tissue kerma rate in air and of neutron flux with increasing thickness of lead-bismuth alloy in the exposure cave.

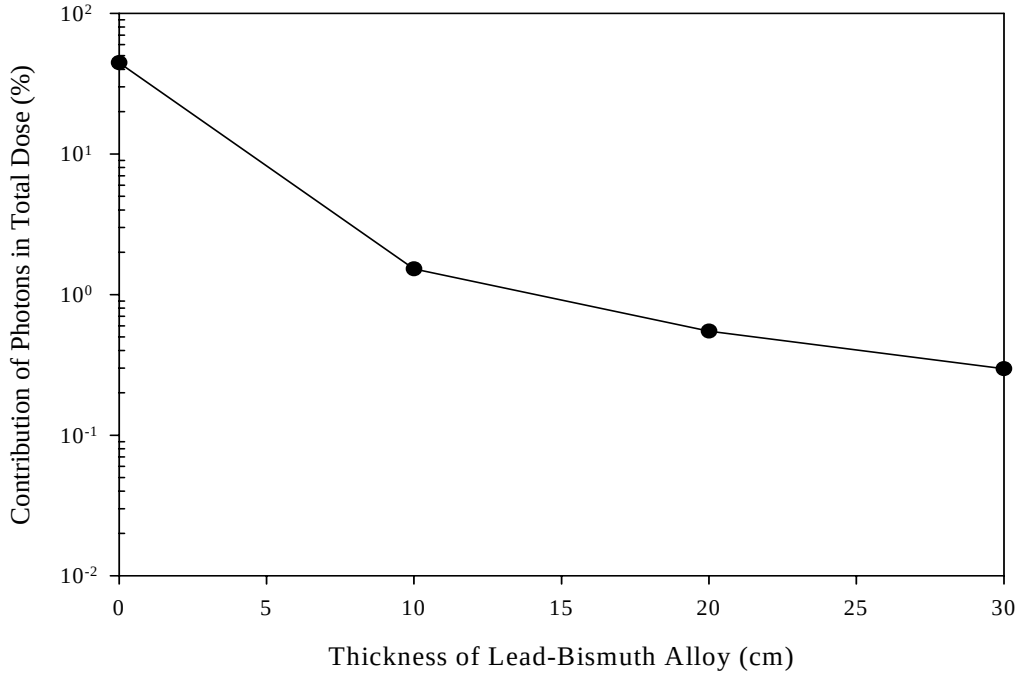

Fig. 3.6. Contribution of gamma rays to total dose with varying thickness of lead-bismuth alloy in the exposure cave.

Therefore, some of scattered gamma rays and neutrons in surrounding concrete and in the air entered into the exposure cave through side faces of the exposure cave, so that the slopes in Figs. 3.5 and 3.6 did not show linear decreasing trends.

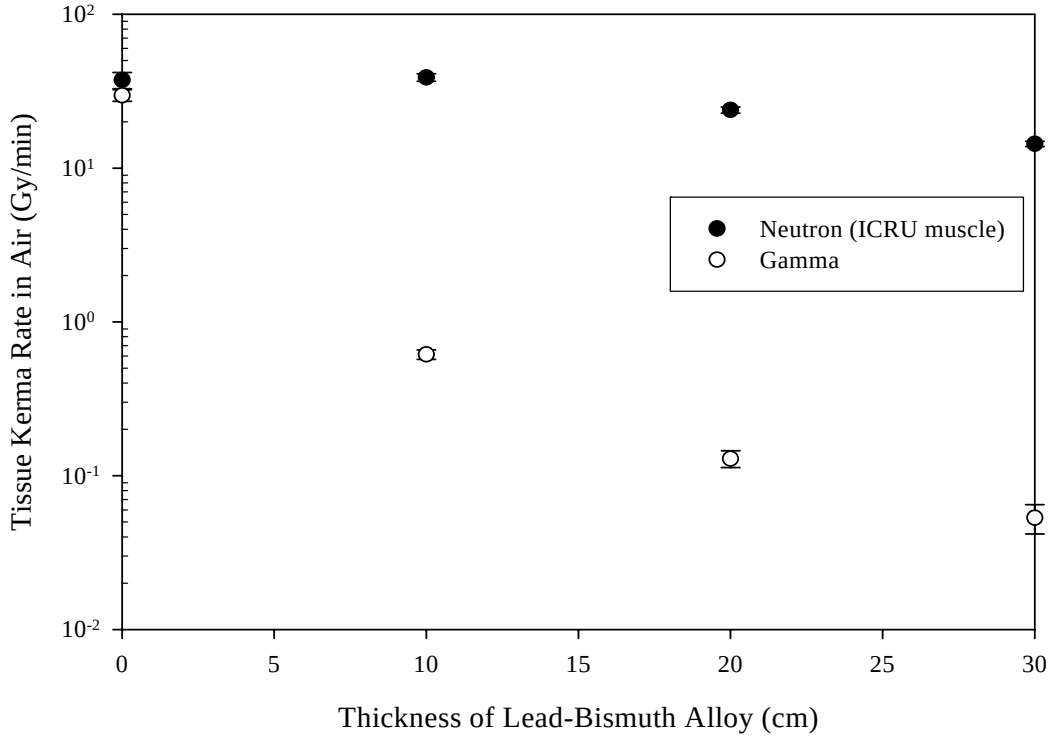

Fig. 3.7. Tissue kerma rate in air of neutrons and of photons with varying thickness of lead-bismuth alloy, respectively.

Fig. 3.7 shows the tissue kerma rate in air of neutrons and of photons as a function of lead-bismuth thickness. As the thickness of the alloy increased, tissue kerma rate in air of neutrons was slightly changed with increasing thickness of the alloy compared with the tissue kerma rate in air of photons. Therefore, the gamma contribution to the total dose was considerably reduced from 50 % to less than 1 % with 30 cm-thick lead-

bismuth alloy. In fact, there are several gamma ray sources in the exposure cave, which originate from fission reactions, capture reactions, and radionuclides produced by capture reactions. Since the MCNP code has no capability to simulate secondary gamma rays emitted by radionuclides produced by capture reactions, the actual gamma contribution to total dose is greater than that predicted by the MCNP code. However, since most of the gamma dose results from the fission- and capture-gamma rays (Ross et al. 1993), the secondary gamma rays produced by the radionuclides have no substantial impact on the total dose while the reactor is in operation against the cell at 1 MW power rating.

Fig. 3.8 shows the tissue kerma rate in air of neutrons inside the exposure cave, which was calculated with different kerma factors stated in the ICRU publication 26 (ICRU 1977). Tissue kerma rate in air of neutrons for the tissue equivalent plastic (A-150) showed 5 % higher than that for the tissue approximation. This was due to the carbon recoils in the plastic (A-150) at fast neutron energies since the carbon in the tissue equivalent plastic was used to substitute the oxygen in the tissue. Tissue kerma rate in air of neutrons increased 5 % in magnitude from 37.3 Gy/min without any filters to 38.3 Gy/min with 10 cm-thick lead-bismuth alloy due to the (n, 2n) reactions of fast neutrons with the lead-bismuth alloy, especially with the lead. In other words, the neutron loss by capture reactions in the alloy was replenished by the neutron production through the (n, 2n) reactions. As the thickness of the lead-bismuth alloy increased further, however, the tissue kerma rate in air started to decrease as the neutron loss became more dominant than the neutron production.

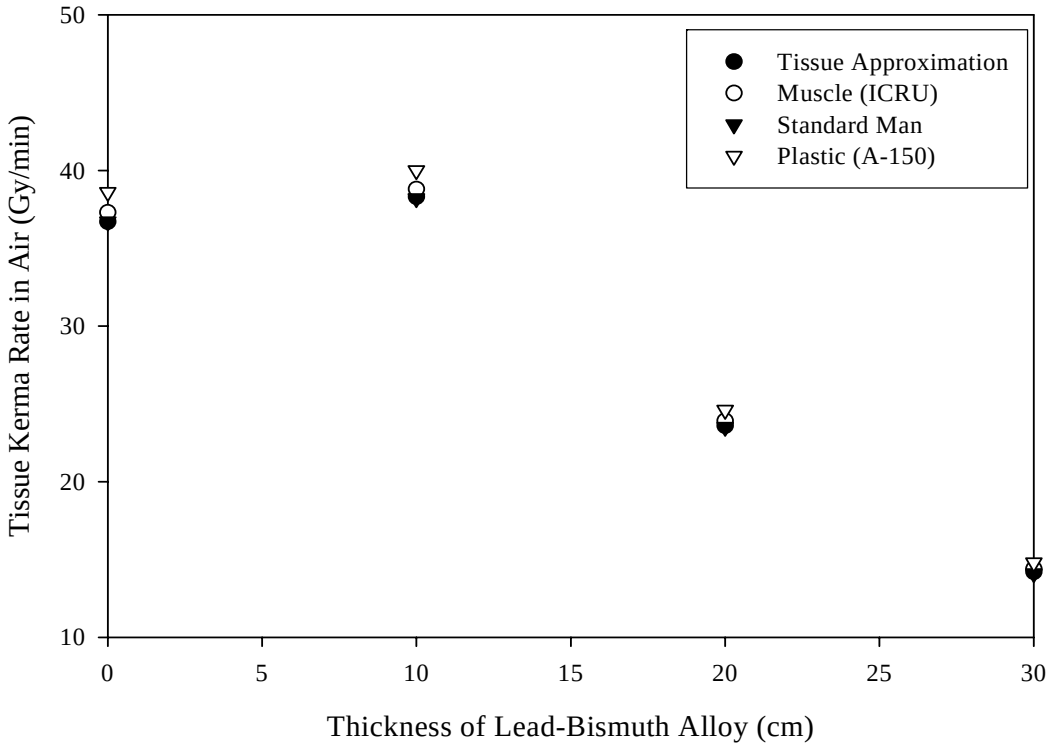

Fig. 3.8. Tissue kerma rate in air of neutrons inside the exposure cave with varying thickness of lead-bismuth alloy, which was calculated with different kerma factors stated in the ICRU publication 26 (ICRU 1977).

3.1.2. Impact of Boral Box on the Neutron Energy Spectra

A sensitivity analysis was performed to find the impact of the boral box used to cut thermal neutrons off around the lead-bismuth alloy on the neutron energy spectra using the MCNP code to calculate dose at a sample point, 122 cm away from the cell window in the irradiation cell. This study modeled the FNIS without any lead-bismuth alloy, including a boral plate in the pool side and a void box in the NSCR core.

Fig. 3.9 shows the differential neutron energy spectra with and without the boral box as a function of neutron energy. Placing the boral box around the 10 cm-thick exposure cave, the slow neutrons of less than 1eV were cut off by the boron carbide in the boral plate. Fig. 3.9, however, showed little change of fast neutron spectra, regardless of the installation of the boral box. Therefore, we can find that the boral box is an effective way of cutting thermal neutrons out by putting 0.635 cm-thick plates around the exposure cave.

Figs. 3.10 and 3.11 show the fractions of neutron flux and of neutron tissue kerma rate in air, respectively. As shown in Fig. 3.10, the fraction of neutron flux of greater than 0.1 MeV became hardened by adding the boral box, showing higher value than that without the boral box. Although the neutron flux-weighted neutron energy increased from 0.85 MeV to 1.10 MeV by adding a boral box surrounding the exposure cave, the weighted neutron energy for the tissue kerma rate in air decreased slightly from 2.16 MeV to 2.10 MeV. The gamma contribution to the total dose increased slightly from 44.4 % to 45.1 % by adding the boral box outside the exposure cave of the FNIS. Therefore, we can find that the boral box is an effective tool to cut out the neutrons of unwanted energies and to minimize unwanted gamma dose inside the exposure cave.

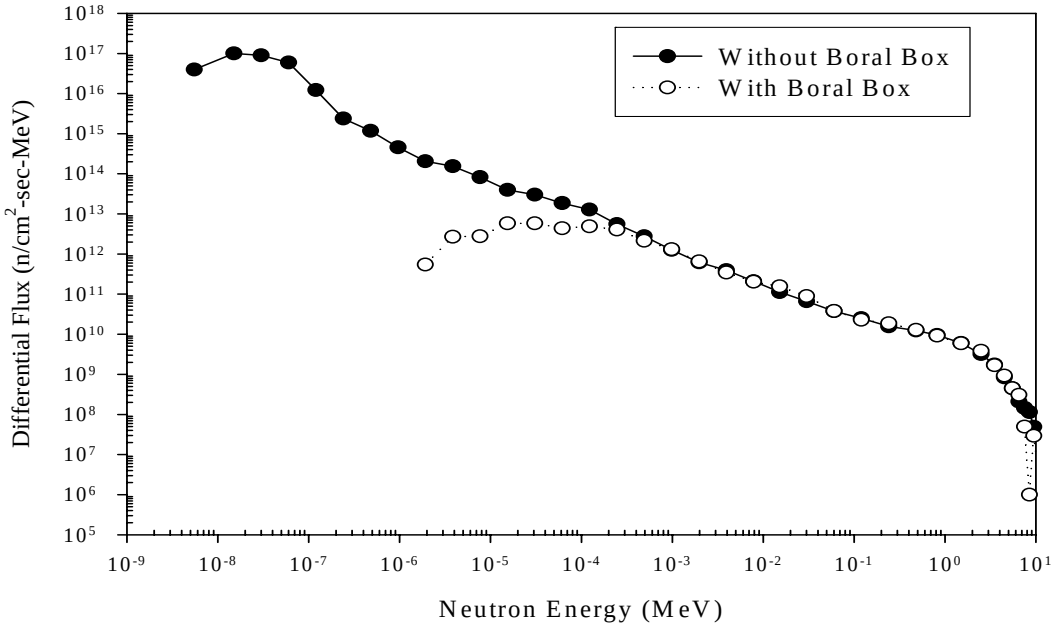

Fig. 3.9. Differential neutron energy spectra simulated by the MCNP with and without boral box, respectively, with a given 10 cm-thick lead-bismuth alloy over all neutron energies.

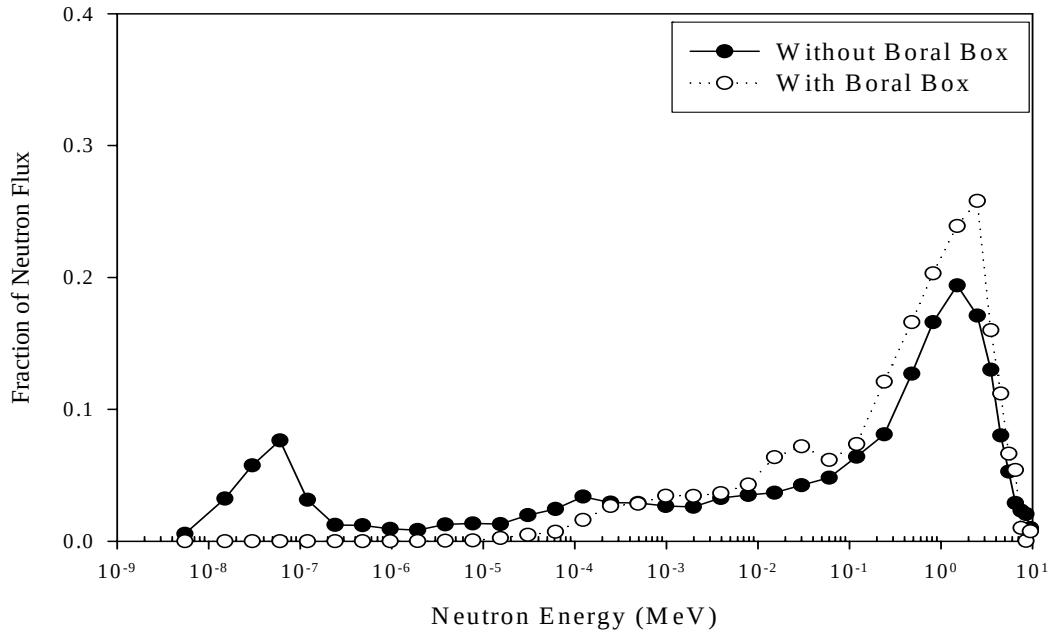

Fig. 3.10. Fraction of neutron flux over all neutron energies with and without boral box, respectively, with a given 10 cm-thick lead-bismuth alloy.

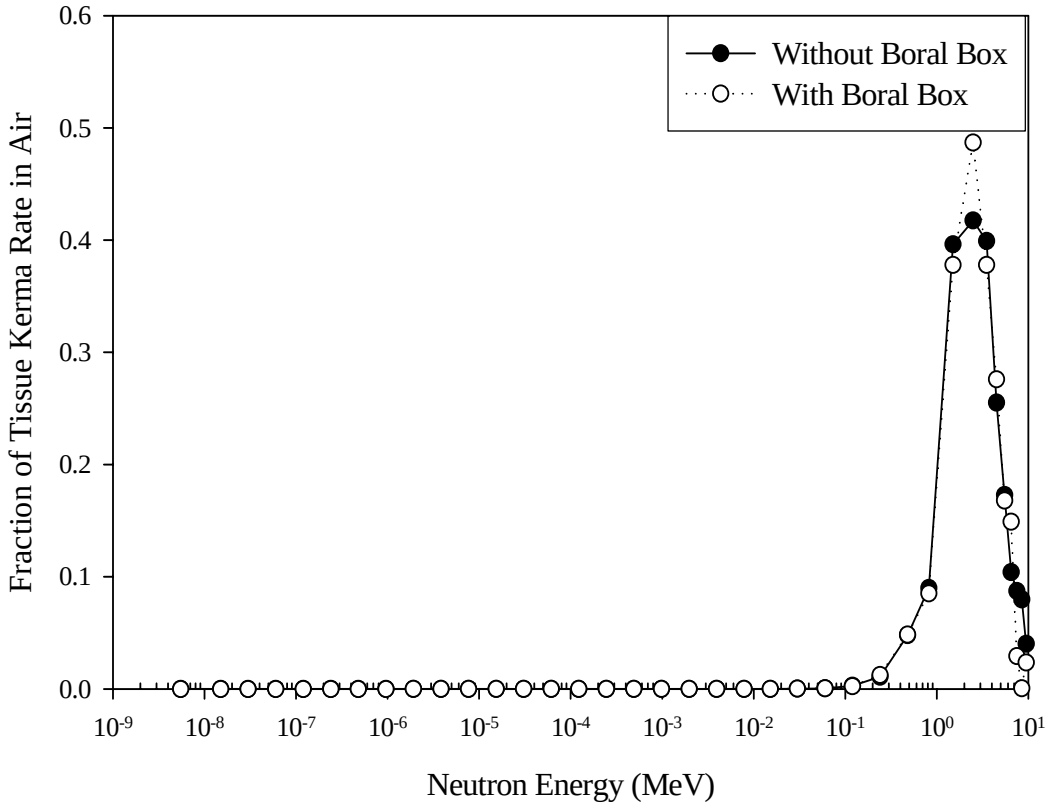

Fig. 3.11. Fraction of tissue kerma in air over all neutron energies with and without boral box, respectively, with a given 10 cm-thick lead-bismuth alloy.

3.1.3. Impact of Aluminum and Other Materials on the Neutron Energy Spectra

A sensitivity analysis was performed to find the impact of the aluminum plate on the mean neutron energy in the exposure cave for the FNIS on the neutron energy spectra using the MCNP code to calculate dose at a sample point, 122 cm away from the cell window in the irradiation cell. The aluminum plate was placed in front of the FNIS with no lead-bismuth shielding. This study modeled the FNIS with a boral box surrounding the exposure cave, including a boral plate in the pool side and a void box in the NSCR core.

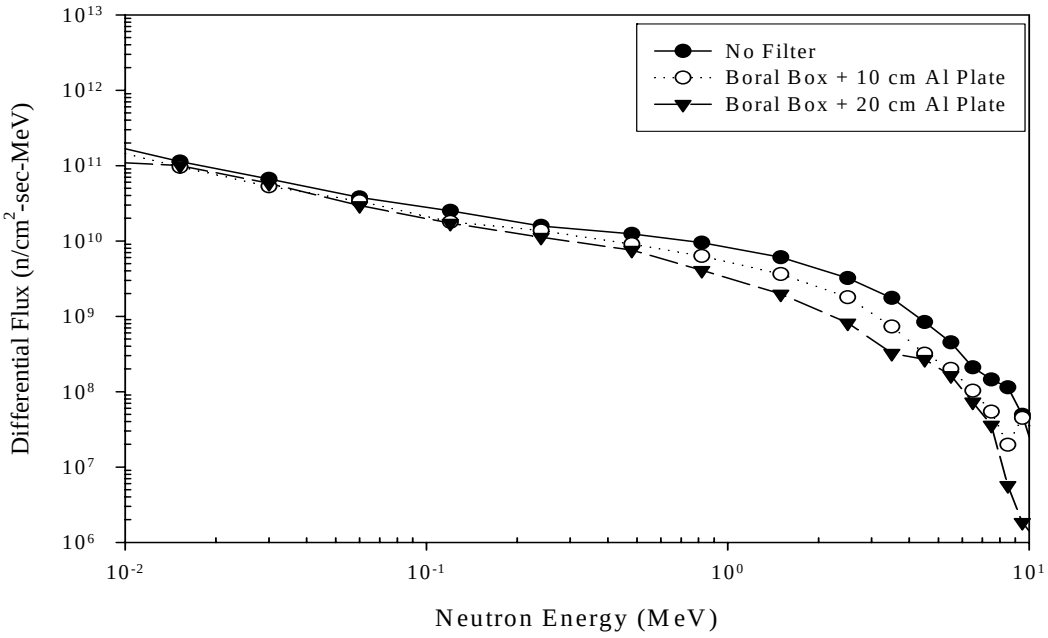

Fig. 3.12. Differential neutron energy spectra for fast neutron energies simulated by the MCNP with varying thickness of aluminum plate.

Fig. 3.12 shows the differential neutron energy spectra with increasing neutron energies over fast neutron region. The neutron spectra were shifted to the left-hand side

due to the scattering reactions of neutrons with the aluminum plate by placing the aluminum plate at the front face of the exposure cave. Figs. 3.13 and 3.14 show the fraction of neutron flux and that of tissue kerma rate in air of neutrons, respectively. As shown in Fig. 3.13, the fraction of neutron flux of greater than 1 MeV decreased and, on the other hand, that of neutron flux of less than 1 MeV increased by adding the aluminum plate, showing the shift of neutron spectrum into left-hand side, i.e., into lower neutron energy region. As shown in Fig. 3.15, the neutron flux-weighted mean neutron energy increased slightly from 0.85 MeV to 0.92 MeV by adding 10 cm-thick aluminum plate and the boral box surrounding the FNIS without any lead-bismuth shielding alloy due to the slow neutron absorption in the boral box.

However, the neutron flux-weighted mean neutron energy decreased from 0.92 MeV to 0.70 MeV by adding additional aluminum plate of 10 cm thickness due to the neutron scattering interactions of the aluminum plate. The mean neutron energy for the tissue kerma rate in air decreased from 2.16 MeV to 1.94 MeV by adding 10 cm-thick aluminum plate and the boral box surrounding the FNIS without any lead-bismuth shielding alloy. The mean neutron energy for the tissue kerma rate in air decreased from 1.94 MeV to 1.66 MeV by adding additional aluminum plate of 10 cm thickness due to the neutron scattering interactions of the aluminum plate. As shown in Fig. 3.16, there was a little change in the gamma contribution to the total dose by adding the aluminum plate, showing 44 % without any aluminum plate to 33 % with 20 cm-thick aluminum plate and boral box surrounding the exposure cave of the FNIS.

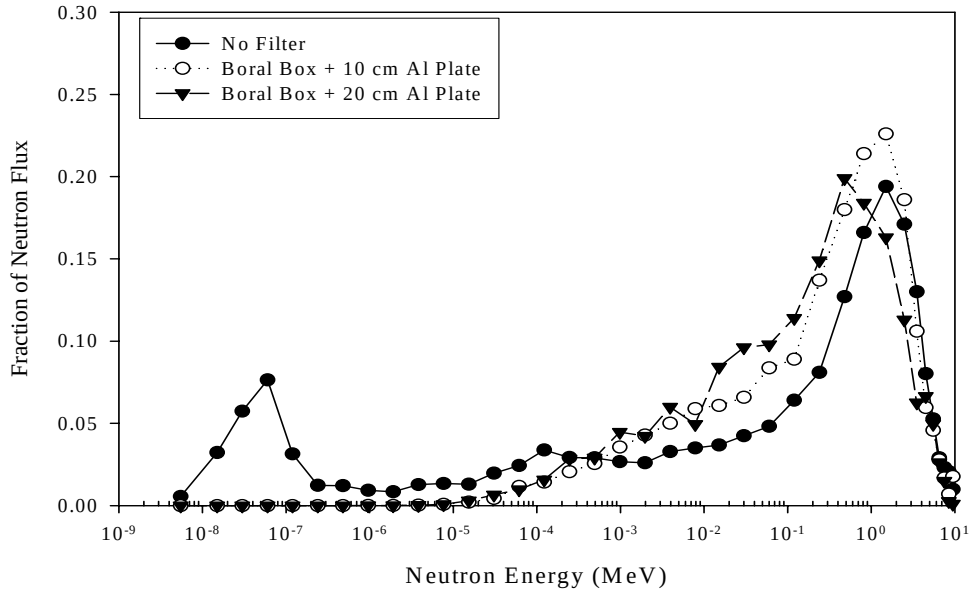

Fig. 3.13. Fraction of neutron flux over all neutron energies with varying thickness of aluminum plate for a given no lead-bismuth alloy in the FNIS.

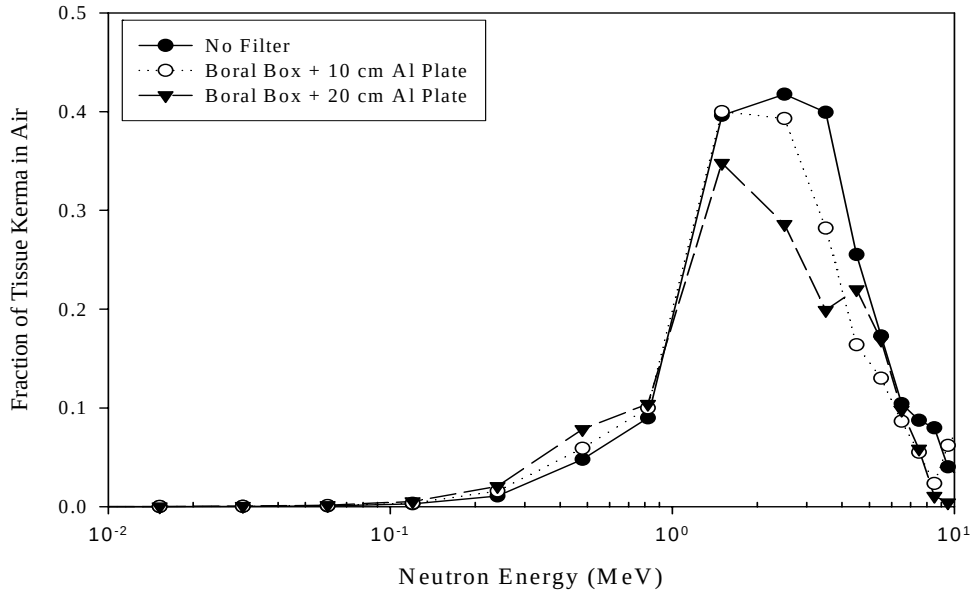

Fig. 3.14. Fraction of tissue kerma rate in air of neutrons for fast neutron energies with varying thickness of aluminum plate for a given no lead-bismuth alloy in the FNIS.

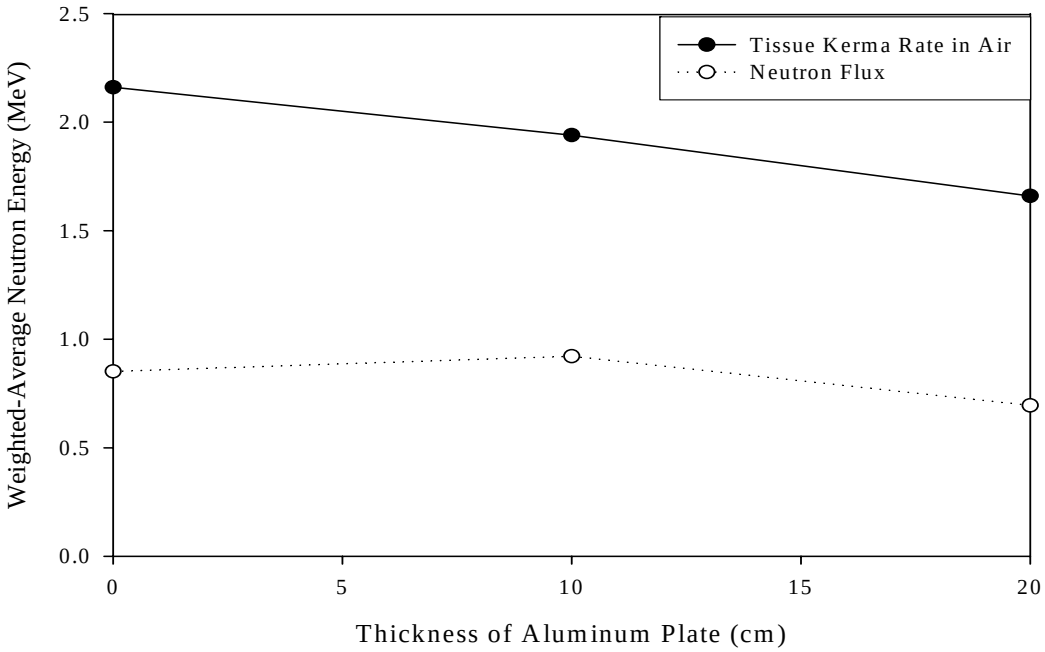

Fig. 3.15. Mean neutron energies weighted by neutron flux and by tissue kerma rate in air of neutrons with increasing thickness of aluminum plate.

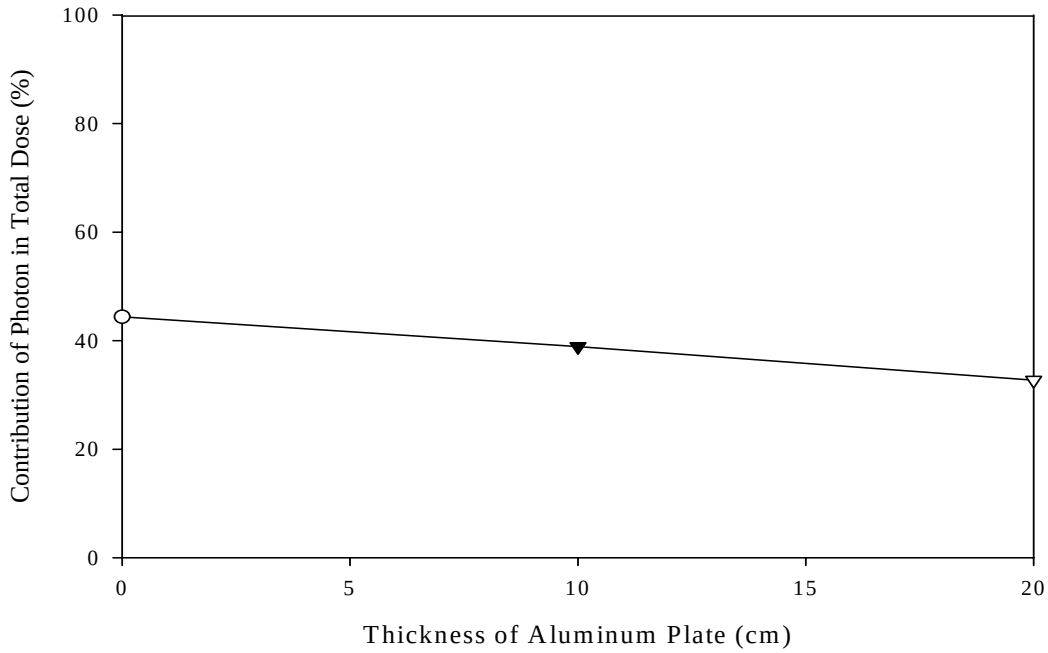

Fig. 3.16. Contribution of gamma rays to total dose with increasing thickness of aluminum plate.

Table 3.1 summarizes the weighted neutron energies and gamma contribution in total dose with various combinations of neutron filters. Although the mean neutron energies generally decreased as the total thickness of filters increased, those values were related to the scattering characteristics of fast neutrons with the materials of interest. Therefore, we can find that the mean neutron energies for the neutron dose can be reduced to values of interest by selecting appropriate materials.

Table 3.1. Mean neutron energies weighted by neutron flux and tissue kerma rate in air of neutrons, and gamma contribution in total dose with various combinations of neutron filters, including a void box, a boral plate, and a boral box.

Combinations of Neutron Filters	$\bar{E}$ (MeV) for Flux	$\bar{E}$ (MeV) for Kerma Rate	Gamma Contribution in Kerma (%)
10 cm Pb/Bi	0.82	1.56	1.5
10 cm Pb/Bi + 10 cm Sulphur	0.73	1.42	1.2
10 cm Pb/Bi + 10 cm Silicon	0.71	1.35	1.2
10 cm Pb/Bi + 10 cm Molybdenum	0.49	0.99	0.5
10 cm Pb/Bi + 10 cm Iron	0.58	1.08	0.6
10 cm Pb/Bi + 20 cm Aluminum + 14 cm Iron	0.36	0.86	0.7

3.1.4. Impact of Reactor Gap on the Neutron Energy Spectra

When operating the NSCR against the irradiation cell, a void box can be put into the front row of fuel elements to minimize neutron thermalization inside the pool side. In addition, a boral plate is usually installed in front of the cell window. Even though reactor operators try to keep the gap between the boral plate and the void box at a minimum in a consistent manner, there is a maximum uncertainty of 1 cm in the gap between the boral plate and the void box. A sensitivity analysis was performed to find the impact of the gap between the boral plate and the void box on the neutron energy spectra with varying thickness of the reactor gap for the FNIS with no lead-bismuth alloy, 122 cm away from the cell window in the irradiation cell. This study modeled the FNIS with a boral box surrounding the exposure cave, including a boral plate in the pool side and a void box in the NSCR core.

As shown in Fig. 3.17, the neutron flux-weighted neutron energy was changed a little, from 1.11 MeV to 1.10 MeV, by changing the gap between the void box and the boral plate from 0 cm to 1 cm for the FNIS with no lead-bismuth alloy. Although the reactor gap did not have significant impact on the neutron energy spectra, this small change in the neutron flux-weighted neutron energy was due to the thermalization process of the water gap followed by the capture reactions of the boral plate. The weighted mean neutron energy for the tissue kerma rate in air of neutrons, in addition, changed only slightly from 2.14 MeV to 2.09 MeV by changing the gap between the void box and the boral plate from 0 cm to 1 cm. This small change was again due to the thermalization process of the water gap followed by the capture reactions of the boral

plate. As shown in Fig. 3.18, there was not a considerable change in the tissue kerma rate in air of neutrons and of photons by putting the gap between the void box and the boral plate from 0 cm to 1 cm for the FNIS with no lead-bismuth alloy.

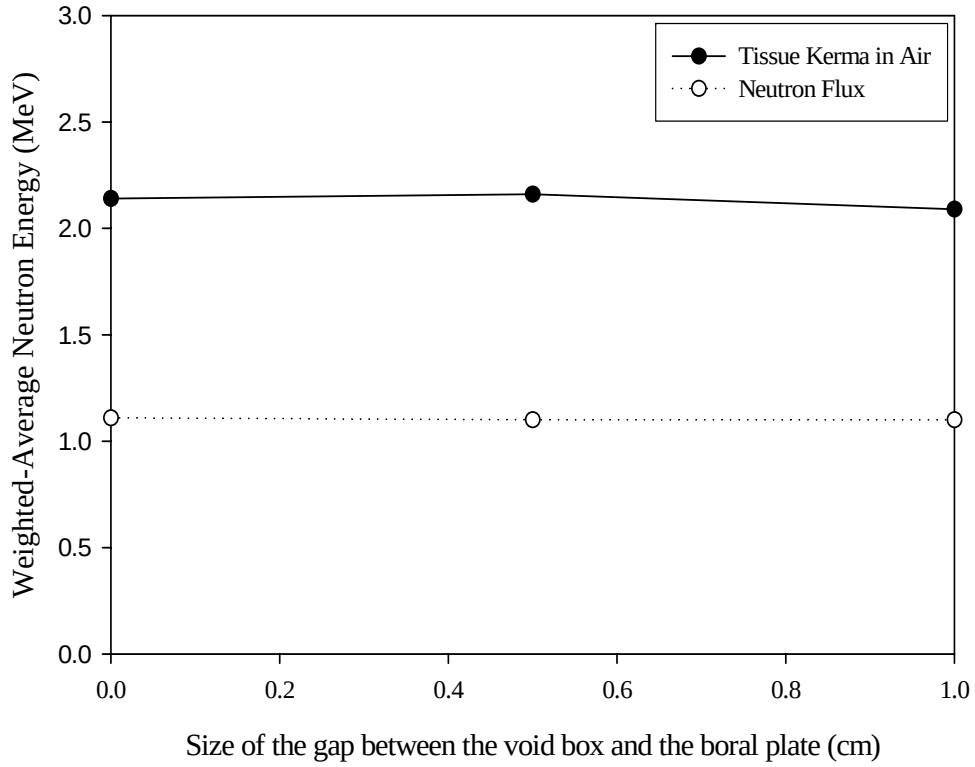

Fig. 3.17. Mean neutron energies for the tissue kerma rate in air of neutrons and neutron flux with variable sizes of reactor gap installed between the void box and the boral plate in the reactor pool-side, respectively.

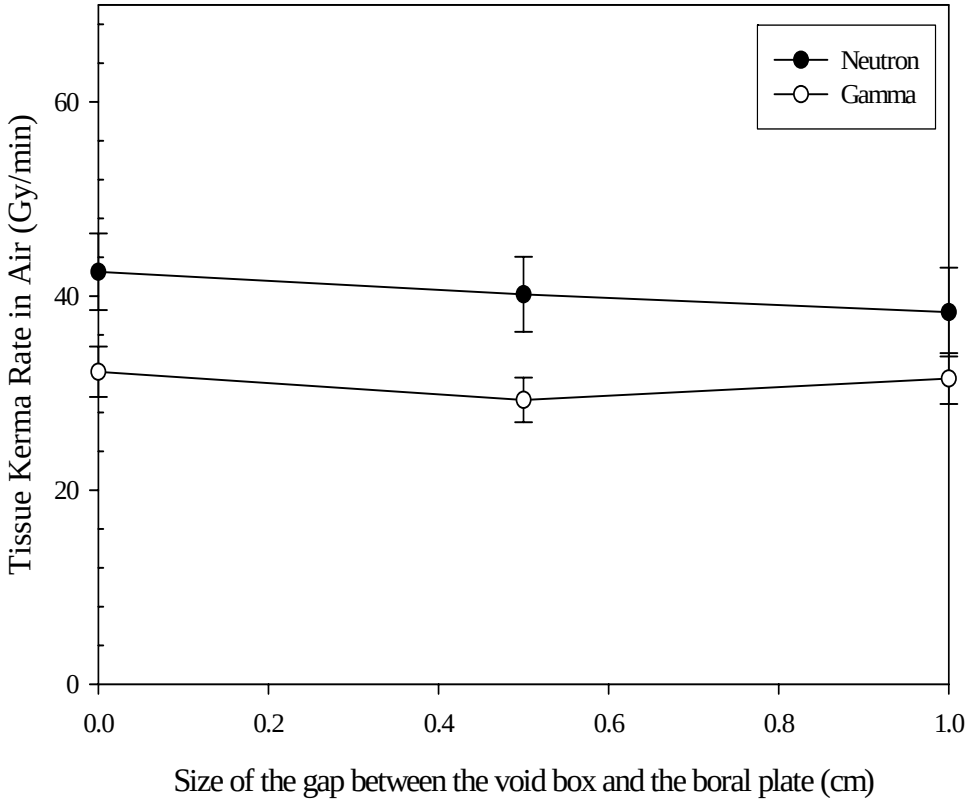

Fig. 3.18. Tissue kerma rate in air of neutrons and of photons with variable sizes of reactor gap installed between the void box and the boral plate in the pool-side, respectively.

3.2. COMPARISON OF MCNP RESULTS WITH EXPERIMENT DATA

3.2.1. Comparison of MCNP Results with Experimental Data Without the FNIS

This study compared neutron spectrum measurements with the MCNP results modeling the irradiation cell without the FNIS. The NSCR core was modeled, as well as the irradiation cell, including a boral plate on the pool side of the cell, and a void box in the NSCR core. Activation foils, which consisted of 10 cadmium-covered foils and a bare aluminum-gold foil, were installed at 13 cm, 61 cm, and 183 cm away from the irradiation cell window, 91 cm above the floor, for characterizing neutron spectra in the cell. In addition, two ion chambers with stainless steel-walls were installed at 61 cm and 183 cm away from the cell window to measure gamma dose rate. The reactor was then placed adjacent to the irradiation cell with the void box and boral plate inside the pool and the reactor was operated at 1 MW for an hour. The specific activities of the samples were measured by counting the samples on a High-Purity Germanium (HPGe) detector gamma spectroscopy system. The neutron energy spectra were then calculated with the SAND-II code, which solves sets of simultaneous activation equations.

In the MCNP calculation, the neutron flux was calculated in each of the 38 energy bins spaced on a logarithmic scale between 1.0×10^{-9} and 1.5×10^{1} MeV. The neutron flux was calculated by using the track-length estimator (F4:N). The statistical error of the MCNP-calculated total neutron flux was less than 5% after 150 active cycles of 10000 neutron histories in a KCODE calculation. This study used the MCNP calculated neutron spectra as the initial spectra of the SAND-II code. The computed neutron spectrum by SAND-II depends significantly on the initial neutron spectrum when a small number of

activation foils are used. There is, therefore, some limitation in quantitative comparison of the SAND-II results to the MCNP results.

Figs. 3.19 and 3.20 show the differential neutron flux at the distance of 13 cm, 61 cm, and 183 cm away from the irradiation cell window without the FNIS, 91 cm above the floor, as calculated by MCNP and as computed by SAND-II from the foil measurements for all neutron energies and for fast neutron energies, respectively. Table 3.2 shows summarized neutron flux for over all neutron energies, for fast neutrons with energies greater than 10 keV, and for thermal neutrons with less than 1 eV, respectively. Fig. 3.21 shows the ratio of the MCNP to SAND-II results without the FNIS in the irradiation cell for the distance from the irradiation cell window. For the fast neutrons greater than 0.1 MeV, the SAND-II results were in good agreement with the MCNP calculated results at the location of 13 cm away from the cell window. As the distance from the cell window increased from 13 cm to 183 cm, the ratios of MCNP to SAND-II results in neutron flux increased from 1.12 to 1.58 for over all neutron energies, from 1.19 to 1.78 for the fast neutrons of greater than 10 keV, and from 0.99 to 1.23 for the thermal neutrons of less than 1eV.

Table 3.2. Neutron flux calculated using the MCNP and the SAND-II at different locations from the cell window without the FNIS, respectively (1 cm gap + safety shim location at 80%).

Distance from the Cell Window	Flux Category	MCNP (n/cm^2-sec)	SAND-II (n/cm^2-sec)	Ratio of MCNP to SAND-II
13 cm	ϕ (total)	$6.19\times10^{11}\pm1.52\times10^{10}$	5.54×10^{11}	1.12
	ϕ (E>10 keV)	$4.37\times10^{11}\pm8.71\times10^{9}$	3.66×10^{11}	1.19
	ϕ (E<1eV)	$6.01\times10^{10}\pm2.30\times10^{9}$	6.06×10^{10}	0.99
61 cm	ϕ (total)	$1.73\times10^{11}\pm6.19\times10^{9}$	1.26×10^{11}	1.37
	ϕ (E>10 keV)	$1.14\times10^{11}\pm3.69\times10^{9}$	7.83×10^{10}	1.45
	ϕ (E<1eV)	$2.08\times10^{10}\pm9.17\times10^{8}$	1.54×10^{10}	1.35
183 cm	ϕ (total)	$3.85\times10^{10}\pm5.20\times10^{9}$	2.43×10^{10}	1.58
	ϕ (E>10 keV)	$2.37\times10^{10}\pm2.80\times10^{9}$	1.33×10^{10}	1.78
	ϕ (E<1eV)	$6.33\times10^{9}\pm9.51\times10^{8}$	5.13×10^{9}	1.23

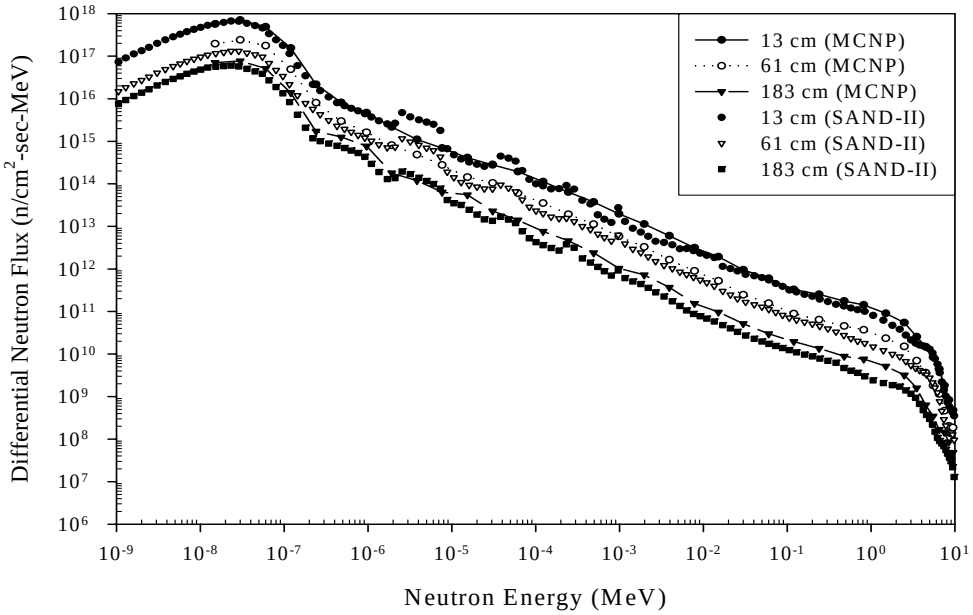

Fig. 3.19. Differential neutron energy spectra simulated by the MCNP, as well as by the SAND-II using the measured specific activities of activation foils over all neutron energies without FNIS.

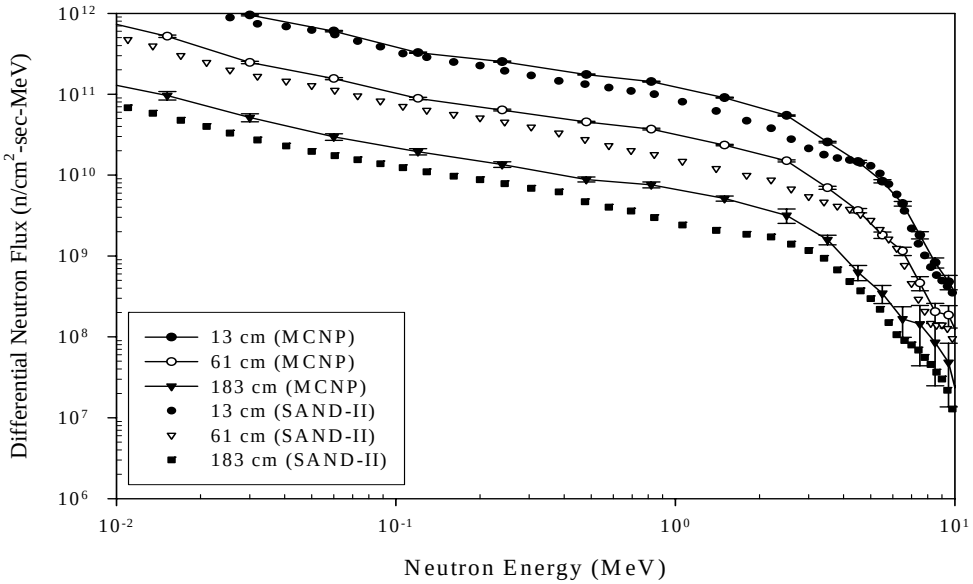

Fig. 3.20. Differential neutron energy spectra simulated by the MCNP, as well as by the SAND-II using the measured specific activities of activation foils for fast neutron energies without FNIS.

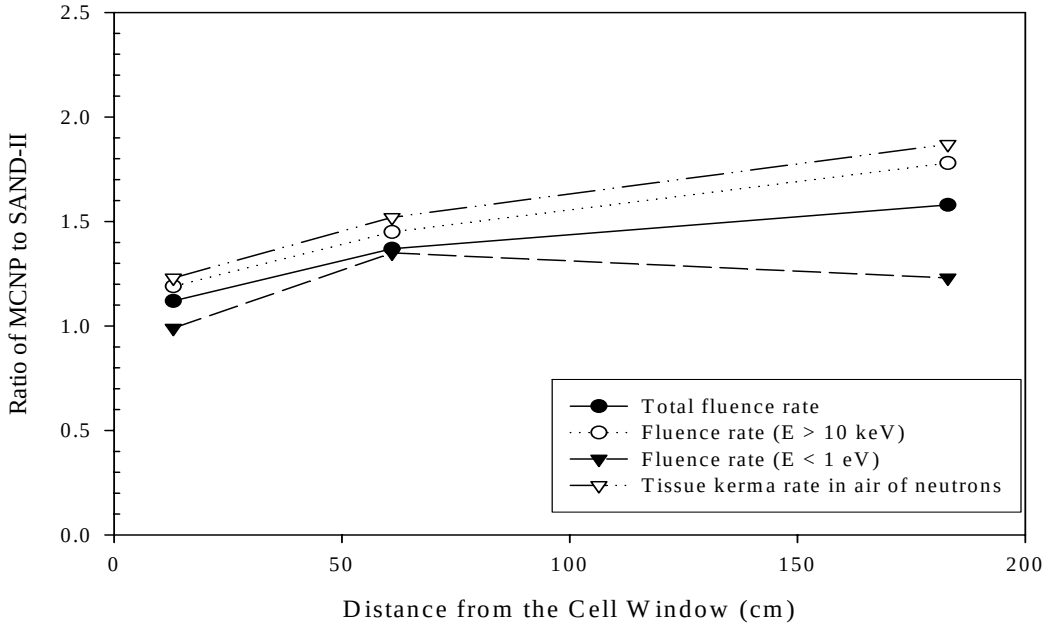

Fig. 3.21. The ratio of the MCNP to SAND-II results without the FNIS in the irradiation cell for the distance from the irradiation cell window.

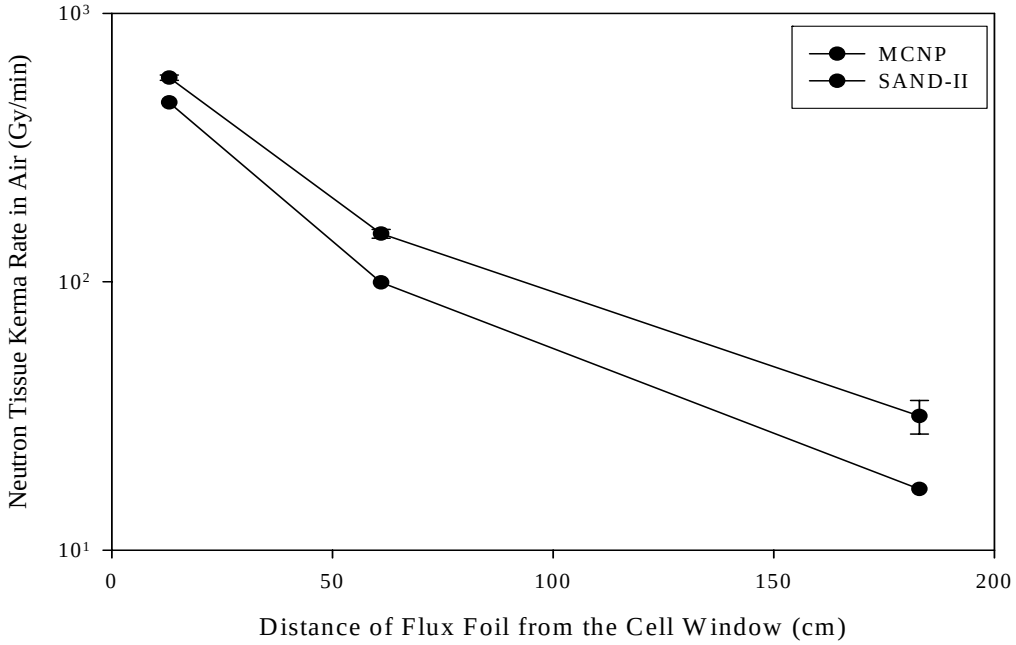

Fig. 3.22. Tissue kerma rate in air of neutrons simulated by the MCNP, as well as by the SAND-II using the measured specific activities of activation foils without FNIS.

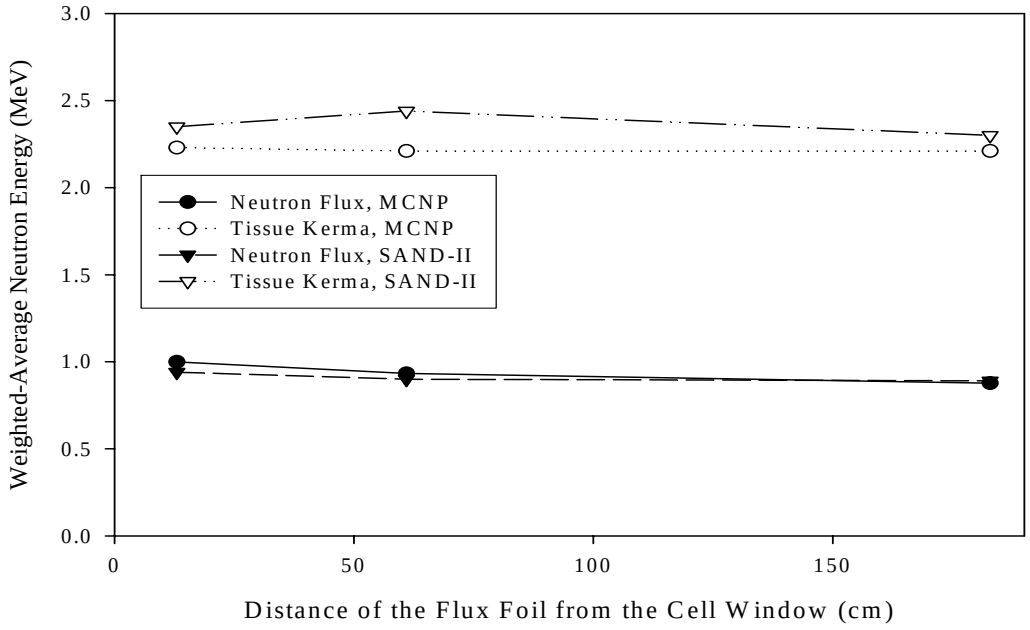

Fig. 3.23. Mean neutron energies based on the MCNP and SAND-II results of the tissue kerma rate in air of neutrons and neutron flux without FNIS, respectively.

Table 3.3. Tissue kerma rate in air of neutrons without the FNIS calculated with neutron flux and kerma factor stated in the ICRU-26.

Distance from the Cell Window	MCNP (Gy/min)	SAND II (Gy/min)	Ratio of MCNP to SAND-II
13 cm	$5.76\times10^{2} \pm 1.31\times10^{1}$	4.65×10^{2}	1.23
61 cm	$1.51\times10^{2} \pm 5.78\times10^{0}$	9.94×10^{1}	1.52
183 cm	$3.16\times10^{1} \pm 4.56\times10^{0}$	1.69×10^{1}	1.87

As shown in Fig. 3.22 and Table 3.3, the tissue kerma rate in air of neutrons decreased from $5.76\times10^{2} \pm 1.31\times10^{1}$ Gy/min to $3.16\times10^{1} \pm 4.56\times10^{0}$ Gy/min for MCNP, and from 4.65×10^{2} Gy/min to 1.69×10^{1} Gy/min for SAND-II as the distance from the cell window to the foil location increased from 13 cm to 183 cm. The MCNP-calculated values were always greater than the SAND-II-calculated values. As the distance from the NSCR core to the location of interest increased, the uncertainties of the MCNP results increased due to the low neutron population at locations far away from the NSCR core. The uncertainties in the measured specific activities also increased due to the lower neutron flux. Although the maximum ratio of MCNP to SAND-II results increased to 1.78 at the distance of 183 cm away from the irradiation cell window without the FNIS, the difference was not surprising considering the small size and complexity of the NSCR core, the variation of water gap between the NSCR and the aluminum window of the irradiation cell, and the various approximations made in the MCNP and SAND-II.

Fig. 3.23 shows the weighted neutron mean energies for the neutron flux and for the tissue kerma rate in air with increasing distance from the cell window. The weighted neutron energy for the neutron flux decreased from 0.99 MeV to 0.88 MeV for MCNP and decreased from 0.94 MeV to 0.89 MeV for SAND-II as the distance from the cell window to the foil location increased from 13 cm to 183 cm. The weighted neutron energy for the tissue kerma rate in air of neutrons slightly changed from 2.23 MeV to 2.21 MeV for MCNP and from 2.35 MeV to 2.30 MeV for SAND-II as the distance from the cell window to the foil location increased from 13 cm to 183 cm. The maximum difference between the MCNP and SAND-II was 5.3% for the weighted mean

neutron energy of the neutron flux and 10.4% for that of the tissue kerma rate in air, respectively. Although the neutron flux and tissue kerma rate in air between the MCNP and SAND-II had differences in magnitude, the weighted mean neutron energy showed good agreement in magnitude and consistency in trend since the normalized neutron energy spectra were in good agreement between the MCNP and SAND-II (see Fig. 3.24). Fig. 3.24 shows the normalized neutron energy spectra, in which the total neutron flux within the energy range of $1.0\times10^{-9} – 1.5 \times 10^{1}$ MeV was set equal to one.

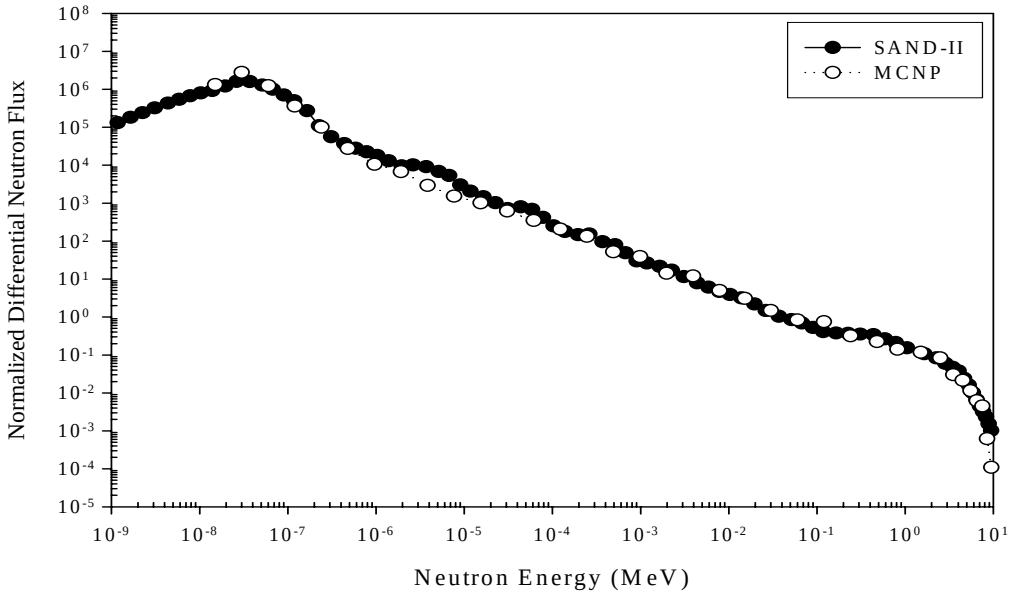

Fig. 3.24. Normalized neutron spectra from SAND-II and MCNP at the distance of 183 cm away from the irradiation cell window without the FNIS (The calculated spectrum was normalized so that the total neutron flux within the energy range of $1.0\times10^{-9} – 1.5 \times 10^{1}$ MeV was equal to one).

For the tissue kerma rate in air of photons, the measured gamma dose rates at the location of 61 cm and 183 cm from the cell window at the height of 91 cm above the

floor were $1.74\times10^{2} \pm 3.60\times10^{0}$ Gy/min and $3.46\times10^{1} \pm 0.77\times10^{0}$ Gy/min, respectively. The MCNP results were 1.22×10^{2} Gy/min and 2.50×10^{1} Gy/min at the location of 61 cm and 183 cm from the cell window, respectively. The difference between the measured results and the MCNP results was mainly due to the direct interaction of neutrons with the nitrogen filling gas of the stainless steel-walled ion chambers. After adjusting the measured gamma dose rate with the amount of neutron energy deposited in the filling gas, which was calculated by the MCNP, the dose rates were adjusted to 1.28×10^{2} Gy/min and 2.54×10^{1} Gy/min at the location of 61 cm and 183 cm from the cell window, respectively, showing that the difference between the measured and the MCNP results was less than 5 %.

In summary, the MCNP results showed close agreement with the SAND-II results at the location closest to the cell window. However, there was considerable disagreement at the location 1.83 meters from the cell window. Even though the neutron flux and tissue kerma rates in air showed considerable differences, the weighted mean neutron energies showed close agreement between the MCNP and the SAND-II results since the normalized neutron energy spectra were in good agreement each other. Hence, it was found that the SAND-II code is appropriate to characterize the exposure cave as the distance from the cell window increases and the three-dimensional MCNP model is still appropriate to simulate the characteristics of the FNIS in terms of weighted-mean neutron energies.

3.2.2. Comparison of MCNP Results with Experimental Data for the FNIS (I)

Figs. 3.25 and 3.26 show the differential neutron flux inside the FNIS, constructed of 10 cm-thick lead-bismuth alloy at the location of 157 cm away from the irradiation cell window. This study modeled the NSCR core, as well as the irradiation cell, including a boral plate in the pool side, and a void box in the NSCR core. The activation foils, consisted of 10 cadmium-covered foils and a bare aluminum-gold foil, were placed inside the exposure cave at the distance of 5 cm away from the front face. Then, the reactor was operated at 1 MW against the irradiation cell for 90 minutes. As shown in Fig. 3.25, thermal neutron flux below 0.5 eV was negligible due to the boral plates installed in pool side and in the irradiation cell. As shown in Table 3.4, the ratios of MCNP to SAND-II results in neutron flux were 1.2 for total flux, 1.4 for fast neutrons of greater than 10 keV, and negligible for thermal neutrons of less than 1 eV.

Table 3.4. Neutron flux, tissue kerma rate in air of neutrons calculated with the neutron flux and the kerma factor stated in the ICRU-26, and mean neutron energy for the neutron flux and the tissue kerma rate in air with the FNIS, constructed of 10 cm thick lead-bismuth alloy.

Item	MCNP	SAND-II	Ratio of MCNP to SAND-II
ϕ (total, n/cm^2-sec)	$4.10\times10^{10}\pm2.62\times10^{9}$	3.38×10^{10}	1.2
ϕ (E>10 keV, n/cm^2-sec)	$3.49\times10^{10}\pm2.14\times10^{9}$	2.48×10^{10}	1.4
ϕ (E<1eV, n/cm^2-sec)	0	8.80×10^{4}	-
Tissue Kerma Rate in Air of Neutrons (Gy/min)	38.8±2.7	24.3	1.6
Mean Energy for Neutron Flux (MeV)	0.74	0.64	1.2
Mean Energy for Tissue Kerma in Air (MeV)	1.56	1.67	0.9

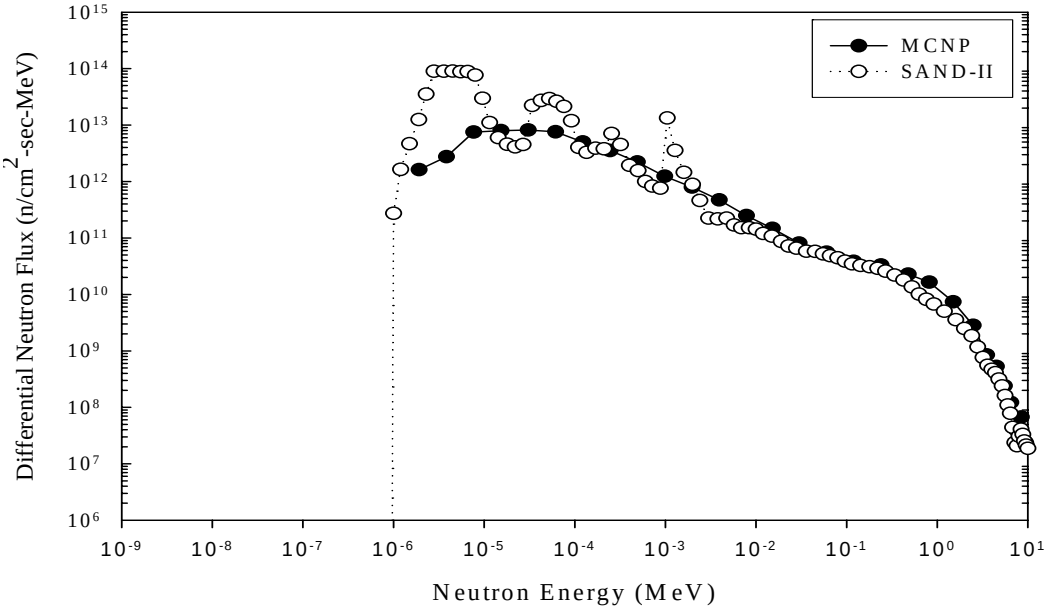

Fig. 3.25. Differential neutron energy spectra obtained by the MCNP, as well as by the SAND-II using the measured specific activities of activation foils over all neutron energies with the FNIS, constructed of 10 cm thick lead-bismuth alloy.

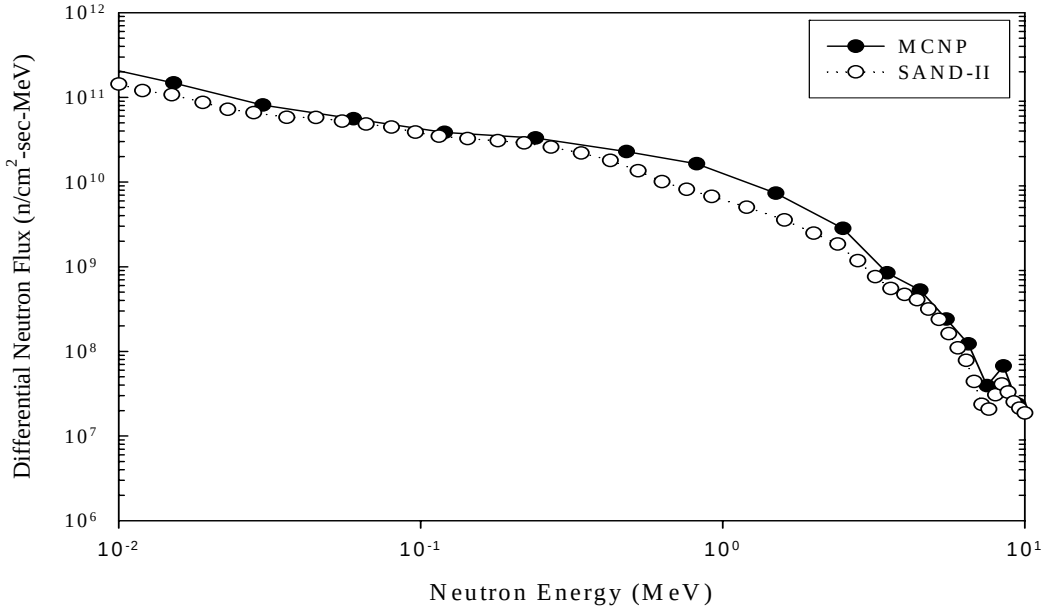

Fig. 3.26. Differential neutron energy spectra obtained by the MCNP, as well as by the SAND-II using the measured specific activities of activation foils for fast neutron energies with the FNIS, constructed of 10 cm thick lead-bismuth alloy.

The tissue kerma rates in air of neutrons were calculated as 38.8 ± 2.7 Gy/min for MCNP and 24.3 Gy/min for the SAND-II, respectively, resulting in a ratio of MCNP to SAND-II of 1.6. The weighted mean energies of neutrons for the neutron flux and for the tissue kerma rate in air were 0.74 MeV and 1.56 MeV for MCNP and were 0.64 MeV and 1.67 MeV for SAND-II, respectively. However, the weighted mean energy of neutrons for the tissue kerma rate in air without the FNIS was 2.21 MeV for MCNP and 2.30 MeV for SAND-II at the location of 183 cm away from the irradiation cell window as stated in Section 3.2.1. These differences in the weighted neutron mean energies, i.e., shifted down in neutron mean energy, were due to scattering interactions of incident fast neutrons with the lead-bismuth alloy. It was, therefore, found that fast neutron beams with mean neutron energy of greater than 0.1 MeV with distinctly different energy spectra were delivered into the exposure cave of the FNIS using different thickness of lead-bismuth alloy.

The difference in the weighted neutron energy for the tissue kerma rate in air was 6.6%. Most of the contribution to the neutron dose resulted from the fast neutrons, which had energies of from 0.1 MeV to 5 MeV. Since the weighted mean energy is calculated with the fraction of neutrons over the energy of interest multiplied by the mean energy, the normalized neutron spectrum plays an important role in the calculation of weighted mean energy. Although the ratio of MCNP to SAND-II results in the tissue kerma rate in air of neutrons was large in magnitude (i.e., 1.6), the weighted mean neutron energy showed good agreement in magnitude (i.e., 6.6%) since the normalized neutron energy spectra were in good agreement between the MCNP and the SAND-II.

3.2.3. Comparison of MCNP Results with Experimental Data for the FNIS (II)

After placing additional 10 cm-thick bricks in front of the exposure cave, constructed of 10 cm thick lead-bismuth alloy, the neutron spectra and the dose rates of neutrons and of gamma rays were measured with activation foils and paired ion chambers, respectively. The exposure cave was installed in the irradiation cell, including a boral box surrounding the exposure cave, a boral plate on the pool side, and a void box in the NSCR core. Activation foils, consisting of 10 cadmium-covered foils and a bare aluminum-gold foil were placed inside the exposure cave at 5 cm away from the face of the window. To measure the tissue kerma rate in air of neutrons and of photons, a graphite ion chamber and a tissue equivalent ion chamber were installed at 5 cm away from the surface of the inside exposure cave, located 157 cm away from the irradiation cell window, 91 cm above the floor. The reactor was operated at 1 MW against the irradiation cell for 90 minutes.

Figs. 3.27 and 3.28 show the differential neutron flux inside the FNIS located at 157 cm away from the irradiation cell window over all neutron energies and over fast neutron energies, respectively. As shown in Fig. 3.27, thermal neutron flux below 0.5 eV was negligible due to the boral plates installed in pool side and in the irradiation cell. As shown in Table 3.5, the ratios of MCNP to SAND-II results in neutron flux were 1.3 for total flux, 1.5 for fast neutrons of greater than 10 keV, and negligible for thermal neutrons of less than 1 eV. The tissue kerma rates in air of neutrons were calculated as 26.8 ± 1.9 Gy/min for MCNP and 13.9 Gy/min for the SAND-II, respectively, showing the ratio of MCNP to SAND-II results as 1.9. The weighted mean energies of neutrons

for the neutron flux and for the tissue kerma rate in air were 0.71 MeV and 1.27 MeV for MCNP and were 0.47 MeV and 1.18 MeV for the SAND-II, respectively

The difference in the weighted neutron energy for the tissue kerma rate in air was 7.6%. Most of the contribution to the neutron dose resulted from the fast neutrons, which had energies of from 0.1 MeV to 5 MeV. Since the weighted mean energy is calculated with the fraction of neutrons over the energy of interest multiplied by the mean energy, the normalized neutron spectrum plays an important role in the calculation of weighted mean energy. Although the ratio of MCNP to SAND-II results in the tissue kerma rate in air of neutrons was large in magnitude (i.e., 1.9), the weighted mean neutron energy showed good agreement in magnitude (i.e., 7.6%) since the normalized neutron energy spectra were in good agreement between the MCNP and the SAND-II.

Table 3.5. Neutron flux, tissue kerma rate in air of neutrons calculated with the neutron flux and the kerma factor stated in the ICRU-26, and mean neutron energy for the neutron flux and the tissue kerma rate in air with the FNIS, constructed of 20 cm thick lead-bismuth alloy.

Item	MCNP	SAND-II	Ratio of MCNP to SAND-II
ϕ (total, n/cm^2-sec)	$2.84\times10^{10} \pm 1.16\times10^{9}$	2.18×10^{10}	1.3
ϕ (E>10 keV, n/cm^2-sec)	$2.34\times10^{10} \pm 9.01\times10^{8}$	1.57×10^{10}	1.5
ϕ (E<1eV, n/cm^2-sec)	0	2.80×10^{5}	-
Tissue Kerma Rate in Air of Neutrons (Gy/min)	26.8 ± 1.1	13.9	1.9
Mean Energy for Neutron Flux (MeV)	0.71	0.47	1.5
Mean Energy for Tissue Kerma in Air (MeV)	1.27	1.18	1.1

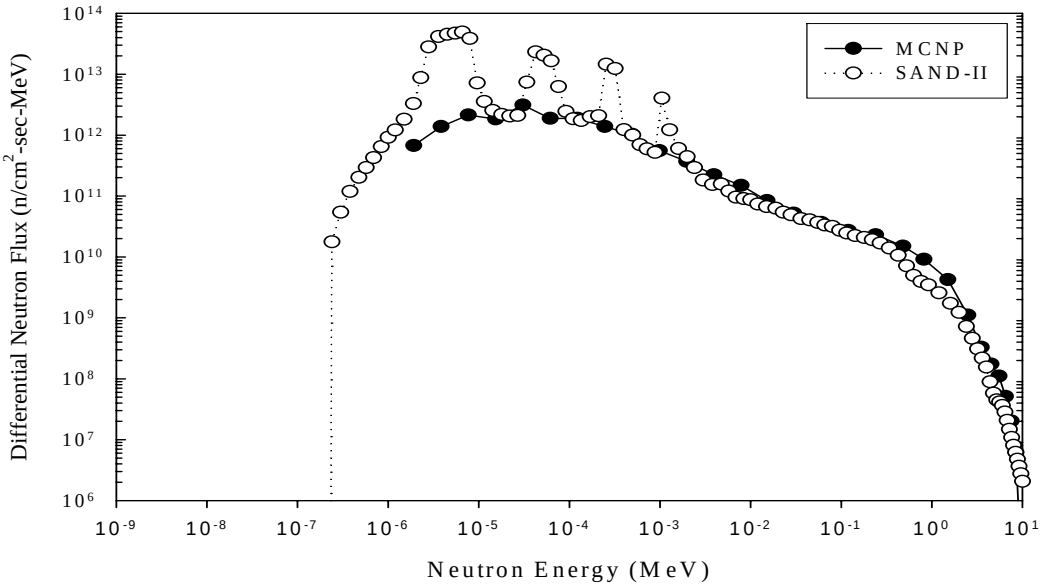

Fig. 3.27. Differential neutron energy spectra calculated by the MCNP, as well as by the SAND-II using the measured specific activities of activation foils with 20 cm-thick lead-bismuth alloy over all neutron energies.

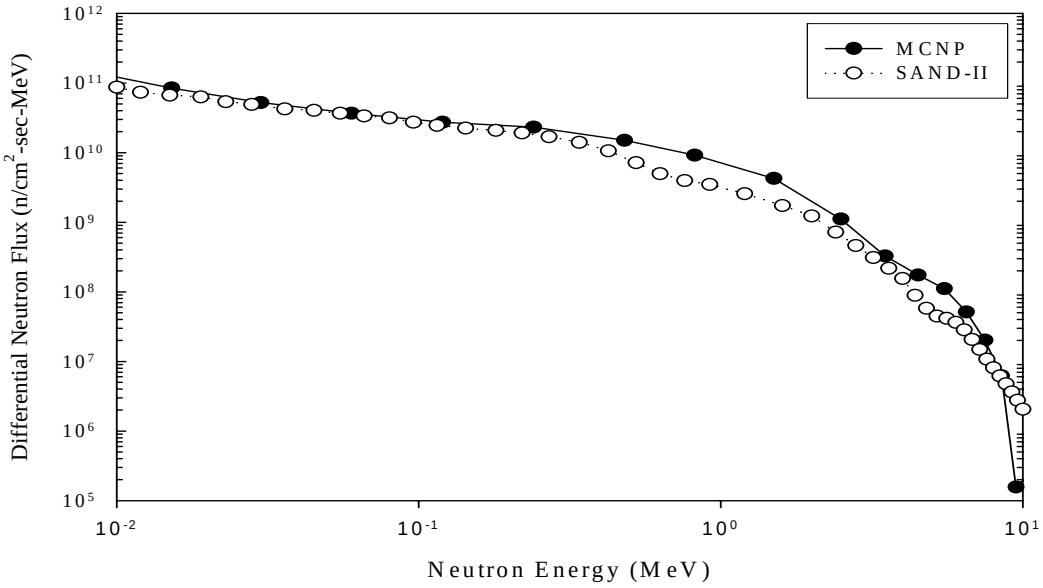

Fig. 3.28. Differential neutron energy spectra calculated by the MCNP, as well as by the SAND-II using the measured specific activities of activation foils with 20 cm-thick lead-bismuth alloy for fast neutron energies.

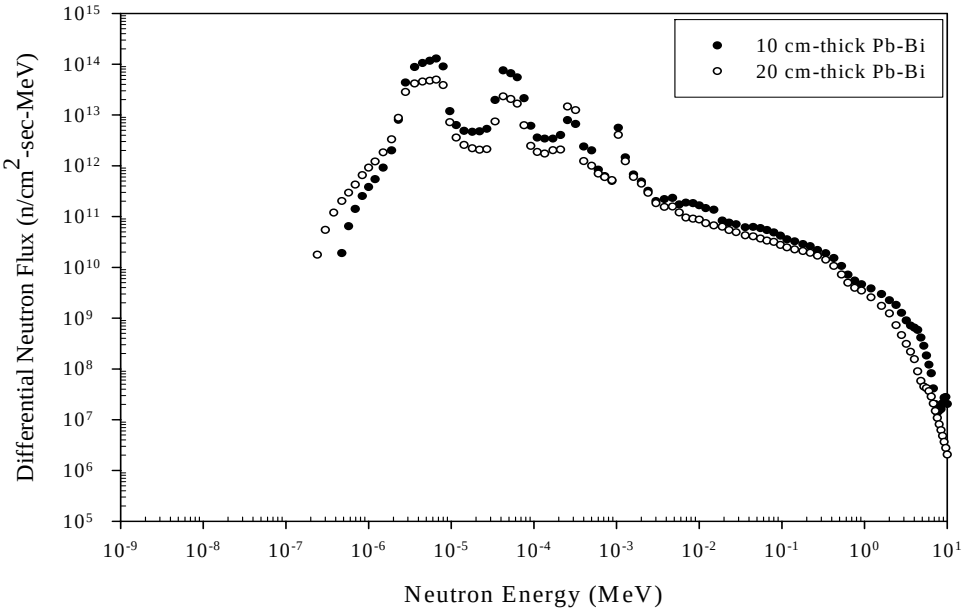

Fig. 3.29. Comparison of the differential neutron energy spectra obtained by the SAND-II using the measured specific activities of activation foils behind10 cm-thick and 20 cm-thick lead-bismuth alloy over all neutron energies.

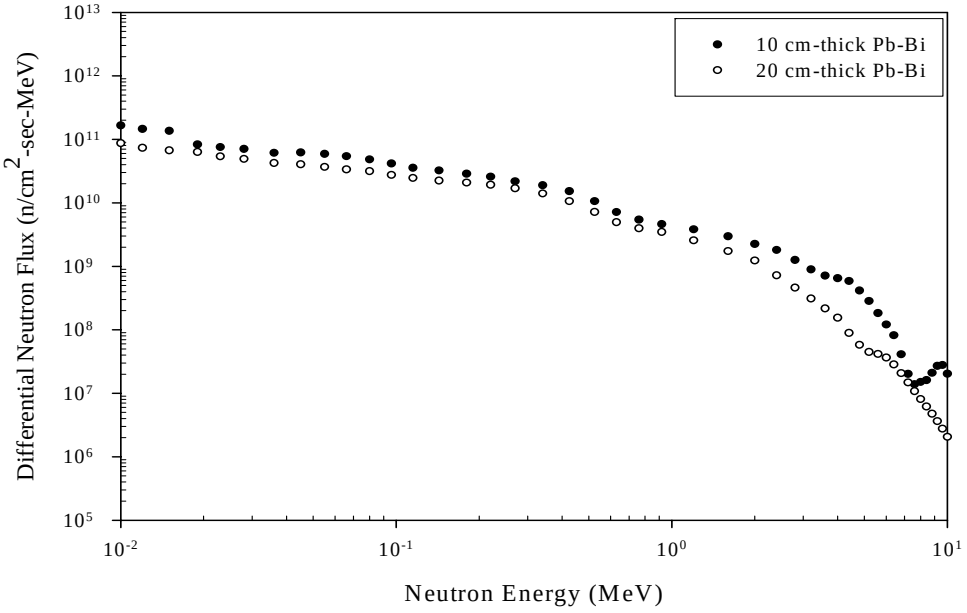

Fig. 3.30. Comparison of the differential neutron energy spectra obtained by the SAND-II using the measured specific activities of activation foils behind 10 cm-thick and the 20 cm-thick lead-bismuth alloy for fast neutron energies.

Figs. 3.29 and 3.30 show the comparisons of differential neutron energy spectra obtained by the SAND-II using the measured specific activities of activation foils behind 10 cm-thick and the 20 cm-thick lead-bismuth alloy over all neutron energies and fast neutron energies, respectively. As shown in Fig. 3.30, since the neutron flux decreased considerably with increasing fast neutron energies, distinctly different neutron energy spectra in terms of neutron dose were brought into the exposure cave of the FNIS.

For the tissue kerma rate in air of neutrons and of photons, three ion chambers, a stainless steel ion chamber, a graphite ion chamber, and a tissue equivalent ion chamber, were installed 5 cm away from the surface of the inside facer of the exposure cave, 122 cm away from the irradiation cell window, 91 cm above the floor. For the stainless steel-walled ion chamber, the absorbed dose rate was measured as $1.75\times10^{0}\pm 3.8\times10^{-2}$ Gy/min. As shown in Table 3.6, the fraction of detector response to the photons through the filling gas was calculated as 6.7 % for the nitrogen filling gas. Hence, the absorbed dose rate of photons was adjusted to be $1.17\times10^{-1}\pm 2.5\times10^{-3}$ Gy/min for the FNIS, constructed of 20 cm-thick lead-bismuth alloy.

Table 3.6. Photon contribution to total dose, which is produced by interacting neutrons with the detector filling gases using the MCNP code.

Items	Gas	No Shielding (%)	20 cm-thick Shielding (%)
Photon Contribution (%)*	N_2	71.7	6.7
	CO_2	86.7	7.3
	Air	71.0	7.6
	Xe	-	91.7
	Ar	-	33.3
	Ne	-	13.2

Note *) Dose rate of photons in tissue was added to the gamma dose rate in the filling gas.

For the paired ion chamber method, the absorbed dose rates of neutrons and of photons were measured as $1.37\times10^{1}\pm 2.3\times10^{-2}$ Gy/min and $6.7\times10^{-1}\pm 1.3\times10^{-1}$ Gy/min based on the physical parameters shown in Table 3.7, respectively. With the basic assumption of the charged particle equilibrium in the detectors, we can compare the tissue kerma rate in air of neutrons calculated using the SAND-II results with the absorbed dose rate of neutrons measured using the paired ion chamber method. The absorbed dose rates of neutrons measured with the paired ion chamber method and calculated with SAND-II were $1.37\times10^{1}\pm 2.3\times10^{-2}$ Gy/min and 1.55×10^{1} Gy/min, respectively. The absorbed dose rate of photons and the gamma contribution to total dose measured using the paired ion chamber method were $6.7\times10^{-1}\pm 1.3\times10^{-1}$ Gy/min and 4.7 %, respectively. The measured results showed good agreement with the SAND-II result. For the second run, the absorbed dose rates of neutrons and of photons measured with the paired ion chamber method were $1.20\times10^{1}\pm 2.0\times10^{-2}$ Gy/min and $7.2\times10^{-1}\pm 1.3\times10^{-1}$ Gy/min, respectively. Although the gamma contribution to the total dose was 5.7 %, the fill gases such as argon and propane were kept in the detectors more than 10 days, so that oxygen could have diffused inside the detectors. Hence, the K_u factor could be increased above 0.02, and then the gamma contribution would be less than 5 % based on the Fig. 3.30.

As shown in Fig. 3.31, although the absorbed dose rate of neutrons was not affected considerably by the ratio of the detector sensitivity to neutrons to the sensitivity to the standard gamma ray, K_u, (i.e., cobalt source used for detector calibration), the absorbed dose rate of photons was affected considerably by the ratio of the detector sensitivity to

neutrons to the sensitivity to the standard gamma ray (i.e., ^{60}Co source). In addition, the uncertainty in the magnitude of gamma dose rate was larger than that of neutron dose rate. Therefore, the gamma contribution to total dose varied from 3.6 % to 6.6 % as the K_u changed from 0.01 to 0.03. Fig. 3.32 shows the relative neutron sensitivities (K_u) of different types of detectors with increasing neutron energy (ICRU 1977).

As stated in ICRU-26, for a neutron field with low gamma contamination, "the overall uncertainty contributed to the determination of the absorbed dose of neutrons will be unchanged, but the overall uncertainty to the determination of the absorbed dose of photons will be 100 times larger." Therefore, it is very difficult to determine a small absorbed dose of photons when accompanied by a large absorbed dose of neutrons. (ICRU 1978). In this case, since the biological effects of the photons are negligible compared with those of neutrons, we could evaluate the absorbed dose rate of photons qualitatively (i.e., the gamma contribution is less than 5 % of total dose).

Table 3.7. Physical parameters used for the absorbed dose characterization in this study.

Reactor Field	Constants
K_t	0.9
K_u	0.02
h_t	1
h_u	1

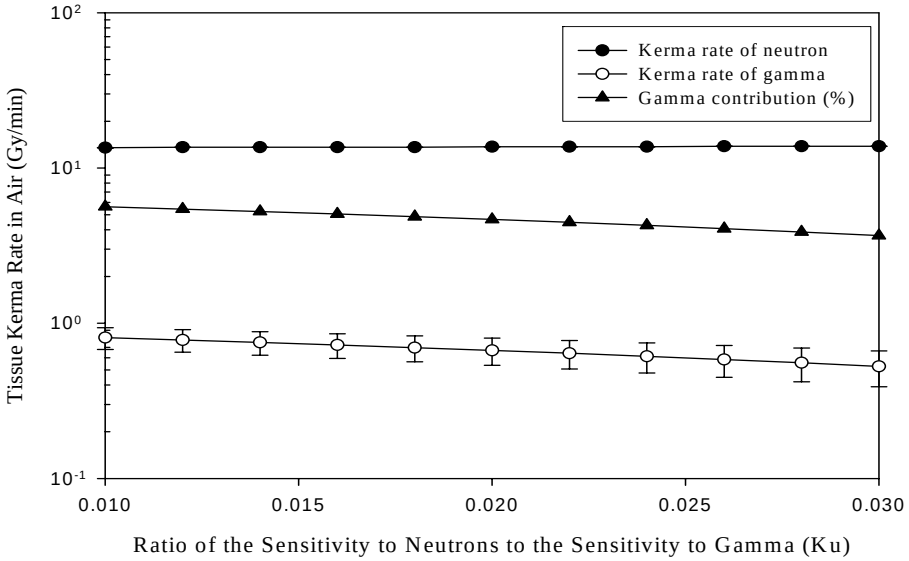

Fig. 3.31. Tissue kerma rate in air of neutrons and of photons measured with paired ionization chamber method and gamma contribution to total dose in percentage with the FNIS, constructed of 20 cm thick lead-bismuth alloy, respectively.

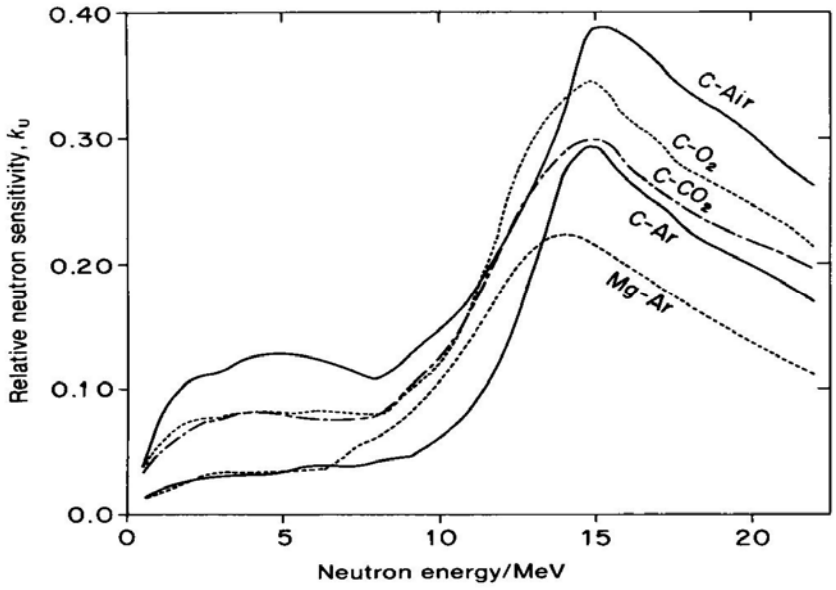

Fig. 3.32. Relative neutron sensitivities of different types of detectors with increasing neutron energy (ICRU 1977).

3.3. Axial and Radial Distribution of Neutrons in the FNIS

To characterize the axial and radial neutron flux distribution, 10 indium foils were installed inside the exposure cave. The AFFRI used rhodium foils to determine field uniformity (Redpath et al. 1995). Figs. 3.33 and 3.34 show the specific activity distributions of the ^{115m}In radionuclide produced by the ^{115}In(n, n′)^{115m}In reaction along axial and radial direction, respectively. Since the threshold energy of the indium for (n, n′) reaction is 0.5 MeV, the specific activities of ^{115m}In results mainly from the reaction of fast neutrons with the indium, so that we can obtain the distribution of fast neutrons of greater than 0.5 MeV inside the exposure cave with the indium foils.

For the radial direction inside the exposure cave, the specific activities of ^{115m}In varied by less than 10 % between the measured values and the mean value as shown in Fig. 3.33. Therefore, it was found that the FNIS could maintain uniform radial dose distribution inside the exposure cave to expose the samples evenly. Since the sample transfer system has some limitation on the sample size due to the sample transfer tube of 10 cm internal diameter, we can estimate the maximum sample size to be put inside a sample carrier as 6 to 7 cm in diameter. With this size of sample, the dose distribution in radial direction can be negligible compared with the axial distribution. For the axial direction of tissue kerma rate in air of neutrons, the specific activity decreased by a factor proportional to the inverse of the square distance from the surface of the reactor core as shown in Fig. 3.34. It is, therefore, necessary for large-size samples in diameter to determine a priori the representative location for dose monitoring.

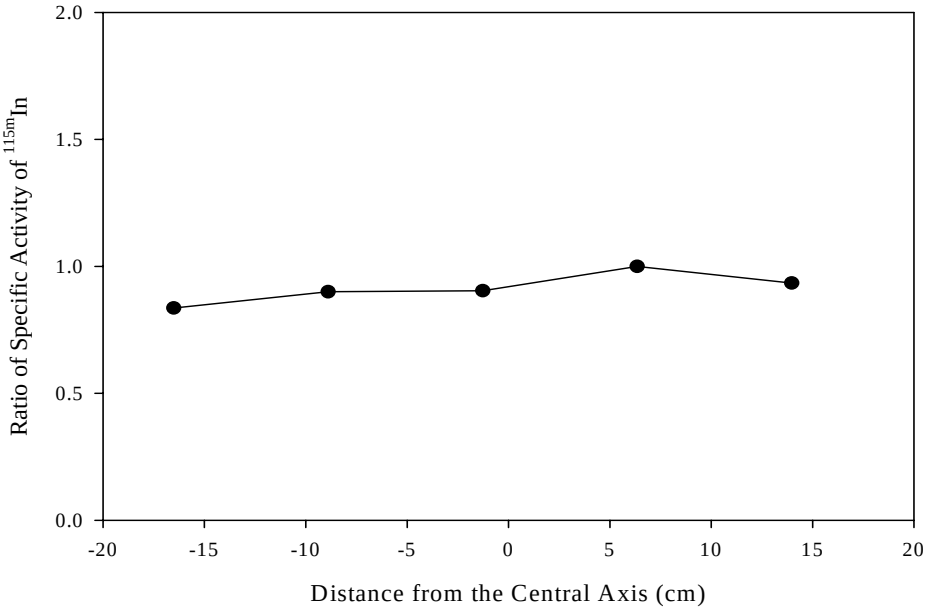

Fig. 3.33. Radial distribution of the specific activities of ^{115m}In produced by the (n, n′) reaction of fast neutrons with the indium foils at 5 cm distance from the front face of the exposure cave of 20 cm thick lead-bismuth alloy.

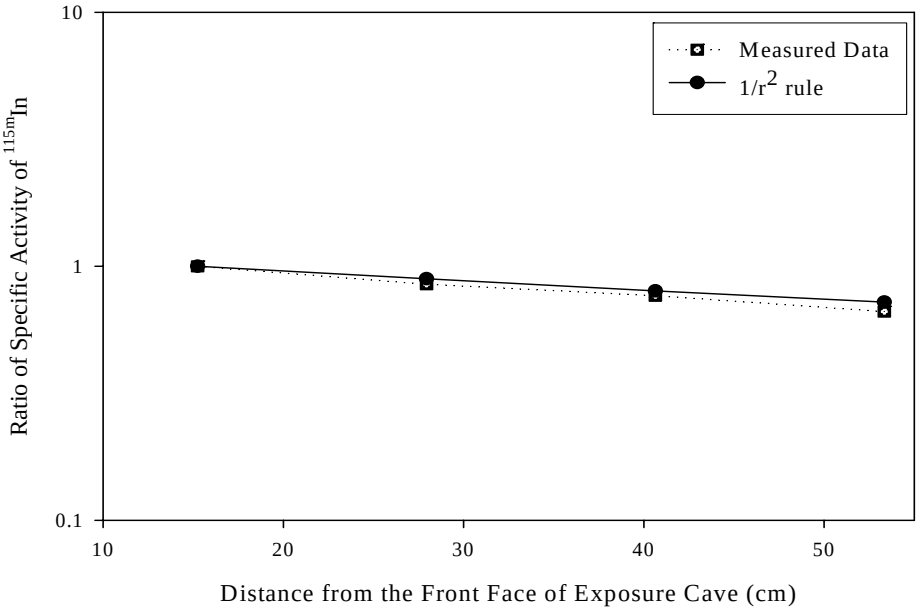

Fig. 3.34. Axial distribution of the specific activities of ^{115m}In produced by the (n, n′) reaction of fast neutrons with the indium foils from the front face of the exposure cave of 20 cm thick lead-bismuth alloy.

3.4. Comparison of Tissue Kerma Rate in Air with Absorbed Dose Rate in Water

For cell culture samples, the sample itself does not disturb the radiation field significantly due to the negligible thickness of the sample. However, for living animals such as mice or rats, we need to consider the effect of the animals on the neutron profile in the exposure cave since the dose, especially the neutron dose, is dependent on the sample size due to moderation of neutrons. To evaluate the effects of sample size on the dose rates of neutrons and of photons, a MCNP simulation was performed with a cube-shaped sample filled with tissue in the exposure cave, which was modeled as 6 cm in width and height and 10 cm in depth. The absorbed dose rates of neutrons and of photons were calculated with the F6 tally directly, and then compared with the tissue kerma rates in air of neutrons and of photons, which were calculated with the neutron flux in the same size cube filled with air and the kerma factor in ICRU tissue.

Fig. 3.35 shows the absorbed dose rates in tissue and the tissue kerma rates in air, respectively. The absorbed dose rates of neutrons in tissue decreased quickly compared to the tissue kerma rates in air of neutrons because of the neutron slowing down process in the tissue followed by neutron capture reactions. Although gammas are shielded by tissue more or less in the same manner, the absorbed dose rates do not decrease with the depth of tissue sample because the capture gamma rays produced by thermalized neutrons in the tissue contribute to the photon dose.

Therefore, whenever the actual absorbed dose rate of neutrons in living animals, especially in a certain organ, is measured with the paired ion chamber method, a correction should be made based on the ratio of the neutron dose results at different

tissue locations of interest using the MCNP code.

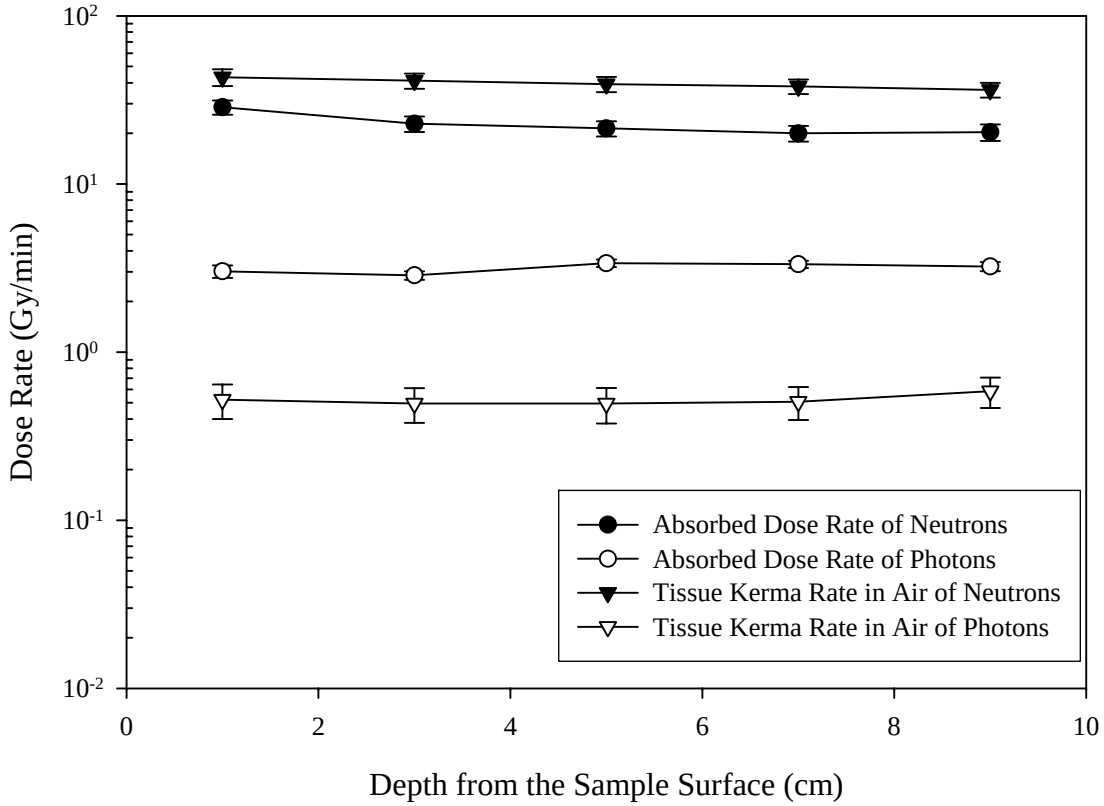

Fig. 3.35. Comparison of absorbed dose rates in tissue and tissue kerma rates in air with varying depth of tissue.

CHAPTER IV

CONCLUSION

A heavily filtered fast neutron irradiation system (FNIS) was developed for a variety of applications, including the study of long-term health effects of fast neutrons by evaluating the biological mechanisms of damage in cultured cells and living animals such as rats or mice. This irradiation system includes an exposure cave made with a lead-bismuth alloy, a cave positioning system, a gamma and neutron monitoring system, a sample transfer system, and interchangeable filters. This system was installed in the irradiation cell of the Texas A&M University Nuclear Science Center Reactor (NSCR). The reactor of the NSC is a 1-MW pool-type MTR-converted TRIGA reactor.

This study used the Monte Carlo N-Particle (MCNP) version 5 code and a set of high-temperature ENDF/B-VI continuous neutron cross-section data for a realistic modeling of the NSCR core, the irradiation cell, and the FNIS. Sensitivity analyses were performed to find out the characteristics of the FNIS regarding the thickness of the lead-bismuth alloy, boral plate, and reactor gap, etc. The neutron spectra were shifted to lower energies by the inelastic scattering interactions of fast neutrons with the alloy as the thickness of the lead-bismuth alloy increased. It was, therefore, possible by changing the alloy thickness to produce distinctly different neutron spectra, in terms of neutron dose, inside the exposure cave of the FNIS.

This study, in addition, tested the Monte Carlo modeling of the FNIS system, as well as the performance of the system by comparing the calculated results with experimental

data measured using activation foils, paired ion chambers, and a simple ion chamber. The neutron spectra characterization showed close agreement with the SAND-II results unfolded from foil measurements close to the cell window. However, the difference between the MCNP and SAND-II was large for locations far away from the cell window. Although there were some differences in the magnitude of the neutron flux and of the tissue kerma rate in air, the weighted average neutron energies showed close agreement between the MCNP and SAND-II since the normalized neutron spectra were in good agreement.

A paired ion chamber system was constructed, one chamber with a tissue equivalent plastic (A-150) and propane gas for total dose monitoring and another with graphite and argon for gamma dose monitoring. Using the pair of detectors, the neutron to gamma dose ratio can be inferred. With the 20 cm-thick FNIS, the absorbed dose rates of neutrons measured with the paired ion chamber method and calculated with the SAND-II results were 13.7 ± 0.02 Gy/min and 15.5 Gy/min, respectively. The absorbed dose rate of photons and the gamma contribution to total dose were 6.7×10^{-1} ± 1.3×10^{-1} Gy/min and 4.7%, respectively. However, the gamma contribution to total dose varied from 3.6 % to 6.6 % as the neutron sensitivity to the graphite detector changed from 0.01 to 0.03. Although it is very difficult to determine a small absorbed dose of photons when accompanied by a large absorbed dose of neutrons, we can be satisfied to evaluate the absorbed dose rate of photons more or less qualitatively since the biological effects of the photons are negligible compared with those of neutrons when the RBE values are considered.

REFERENCES

Attix FH. Introduction to radiological physics and radiation dosimetry. New York: John Wiley& Sons; 1986.

Belmont. Certificate of analysis for low melting alloy (Belmont 2562G). Brooklyn, NY: Belmont Metals Incorporation; 1997.

Briesmeister JF. MCNP^{TM} – A general Monte Carlo code N-particle transport code, version 5. Los Alamos, NM: Los Alamos National Laboratory; LA-UR-03-1987; 2003.

Brooks & Perkins. The specification of Boral^{TM} plate. Detroit, MI: Brooks & Perkins Advanced Structure Company; 1983.

Chen C. Development of SUNMAN: A graphically driven steady state neutronic and thermal hydraulic model of the Nuclear Science Center reactor at Texas A&M University. Ph.D. Dissertation; Texas A&M University; College Station; 1997.

ENDF. Evaluated Nuclear Data File (ENDF). Upton, NY: Brookhaven National Laboratory; ENDF/B-VI; 1998.

Foster Jr. DG, Arthur ED. Average neutron properties of “prompt” fission products. Los Alamos, NM: Los Alamos National Laboratory; LA-9168-MS; 1982.

Gidden P. Flash polymerization of silicone oils using gamma irradiation for conserving waterlogged wood. MS Thesis; Texas A&M University; College Station; 1996.

Griffin PJ, Kelly JG. SAND II manual: Neutron flux spectra determination by multiple foil activation-iterative method. Albuquerque, NM: Sandia National Laboratories; PSR-345; 1994.

International Atomic Energy Agency. Properties of lead-bismuth coolant and perspectives of non-electric applications of lead-bismuth reactor. Vienna, Austria: International Atomic Energy Agency; IAEA-TECDOC-1056; 1998.

International Atomic Energy Agency. Comparative assessment of thermo-physical and thermo-hydraulic characteristics of lead, lead-bismuth, and sodium coolants for fast reactors. Vienna, Austria: International Atomic Energy Agency; IAEA-TECDOC-1289; 2002.

International Commission on Radiation Units and Measurements. Neutron fluence, neutron spectra and kerma. Washington, DC: ICRU Publications; ICRU Report 13; 1969.

International Commission on Radiation Units and Measurements. Radiation protection instrumentation and its application. Washington, DC: ICRU Publications; ICRU Report 20; 1971.

International Commission on Radiation Units and Measurements. Neutron dosimetry for biology and medicine. Washington, DC: ICRU Publications; ICRU Report 26; 1977.

International Commission on Radiation Units and Measurements. An international neutron dosimetry intercomparison. Washington, DC: ICRU Publications; ICRU Report 27; 1978.

Jang SY, Kim CH, Reece WD. Characterization of the neutron field in the irradiation cell of the Texas A&M University Research Reactor for Boron Neutron Capture Therapy (BNCT). Health Physics 82(6):S123; 2002.

Jang SY, Kim CH, Reece WD, Braby LA. Advanced neutron irradiation system for radiation biology. Health Physics 84(6):S165; 2003.

Kim CH, Jang SY, Reece WD. Neutron spectrum determination by Monte Carlo simulation and foil activation. Transaction American Nuclear 86:315-316; 2002.

Kim CH, Jang SY, Reece WD. Monte Carlo modeling of the Texas A&M University Research Reactor. Nuclear Technology 145:1-10; 2004.

Knoll GF. Radiation detection and measurement. New York: John Wiley& Sons; 2000.

National Institute of Standards and Technology. Tables of x-ray mass attenuation coefficients and mass energy absorption coefficients. Washington, DC: National Institute of Standards and Technology; NIST Table Series; 1996.

Matsumoto T. Neutron beam design for neutron radiography at the Musashi reactor. Nuclear Instruments and Methods in Physics Research A 377:48-51; 1996.

Nuclear Science Center. Safety Analysis Report (SAR) for the Nuclear Science Center of Texas A&M University. College Station, TX: Nuclear Science Center (NSC) at Texas A&M University; 2003.

Oak Ridge Associated Universities. Biological effectiveness of neutrons: research needs. Oak Ridge, TN: Oak Ridge Associated Universities; ORAU-94/D-58; 1994.

Prasanna PG, Kolanko CJ, Gerstenberg HM, Blakely WF. Premature chromosome condensation assay for biodosimetry: studies with fission-neutrons. Health Physics 72:594-600; 1997.

Prasanna PG, Loats H, Gerstenberg HM, Torres BN, Shehata CW, Duffy KL, Floura RS, Khusen AW, Jackson WE, Blakely WF. AFRRI's gamma-ray, x-ray, and fission neutron calibration curves for the lymphocyte dicentric assay: Application of a metaphase finder system. Bethesda, MD: Armed Forces Radiobiology Research Institute; AFRRI Special Publication 02-1; 2002.

Redpath JL, Antoniono RJ, Sun C, Gerstenberg HM, Blakely WF. Late Mitosis/Early G1 phase and mid-G1 phase are not hypersensitive cell cycle phases for neoplastic transformation of Hela x skin Fibroblast human hybrid cells induced by fission-spectrum neutrons. Radiation Research 141:37-43; 1995.

Ross D, Constantine G, Weaver DR, Beynon TD. Designing an epithermal neutron beam for boron neutron capture therapy for a DIDO type reactor using MCNP. Nuclear Instruments and Methods in Physics Research A 334:596-606; 1993.

Sakurai Y, Kobayashi T. Characteristics of the KUR Heavy Water Neutron Irradiation Facility as a neutron irradiation field with variable energy spectra. Nuclear Instruments and Methods in Physics Research A 453:569-596; 2000.

Schumacher RF, Randall JD. Determination of spatial and spectral distribution of neutron flux in the Texas A&M Nuclear Science Center Reactor Exposure Cell. College Station, TX: Nuclear Science Center at Texas A&M University; Technical Report No. 31; 1975.

White JR, Jirapongmed A. Design and initial testing of an ex-core fast neutron irradiator for the University of Massachusetts-Lowell Research Reactor. Santa Fe, NM: Radiation Protection and Shielding Topical Conference; 2002.

Zeman GH, Dooley M, Eagleson DM, Goodman LJ, Schwartz RB, Eisenhauer CM, Mcdonald JC. Intercomparison of neutron dosimetry techniques at the AFFRI TRIGA Reactor. Radiation Protection Dosimetry 23:317-320; 1988.

APPENDIX A

MONTE CARLO SOURCE PROGRAMS

These programs calculate neutron flux and photon fluence rate at the location of interest using the F4:N tally of the MCNP.

```
r70: pneumatics tubes were added to B1, C2 and D2 locations.
C 80% SS location, 1 cm gap btn cell window and void box 9/1/'03
C
C Note: XeIrr IC is S/S or Aluminum !! (Cell 602)
C
C 34567890123456789012345678901234567890123456789012345678901234567890123456789012345678901234567890
C ===================================================================
C                           CELL CARDS
C ===================================================================
C
C FUEL PIN - LOW ENRICHED (UNIVERSE = 1)
C
 1  9   8.6023-2  (-2 6 -7):(-3 7 -8):(-5 8 -9)  u=1 imp:n,p=1 $ fitting
 2  7   8.1299-2  -4 9 -10                       u=1 imp:n,p=1 $ low graphite
 3 12   4.2909-2  -1 10 -13        tmp1=4.77-8   u=1 imp:n,p=1 $ inner Zr rod
 4 111  8.9782-2   1 -4  10 -771   tmp1=4.77-8   u=1 imp:n,p=1 $ fuel seg. #1
 5 112  8.9782-2   1 -4 771 -772   tmp1=4.77-8   u=1 imp:n,p=1 $ fuel seg. #2
 6 113  8.9782-2   1 -4 772 -773   tmp1=4.77-8   u=1 imp:n,p=1 $ fuel seg. #3
 7 114  8.9782-2   1 -4 773 -774   tmp1=4.77-8   u=1 imp:n,p=1 $ fuel seg. #4
 8 115  8.9782-2   1 -4 774 -13    tmp1=4.77-8   u=1 imp:n,p=1 $ fuel seg. #5
 9  7   8.1299-2  -4 13 -14                      u=1 imp:n,p=1 $ up graphite
10  8   8.6218-2   4 -5 9 -14                   u=1 imp:n,p=1 $ cladding
11  9   8.6023-2  (-5 14 -15):(-3 15 -16):(-2 16 -18) u=1
                                                    imp:n,p=1 $ fitting
12 10     -2.112  -6:(2 6 -7)                    u=1 imp:n,p=1 $ mixed Al
13  6   1.0004-1  (3 7 -8):(5 8 -15):(3 15 -16)  u=1 imp:n,p=1 $ H2O
14 11   6.0240-2  (2 16 -17)                     u=1 imp:n,p=1 $ Al
15  6   1.0004-1  (2 17 -18):18                  u=1 imp:n,p=1 $ H2O
C
C LOW ENRICHED 4-ELEMENT BUNDLE (UNIVERSE = 2)
C
16  0         -19   fill=1                   u=2 imp:n,p=1 $ fuelpin SW
17 like 16 but trcl=(3.8862  0  0)                        $ fuelpin SE
18 like 16 but trcl=(0 3.8862  0)                         $ fuelpin NW
19 like 16 but trcl=(3.8862  3.8862  0)                   $ fuelpin NE
C
20 10    -2.112  -7       #16 #17 #18 #19     u=2 imp:n,p=1 $ mixed Al
21  6  1.0004-1   7 -16   #16 #17 #18 #19     u=2 imp:n,p=1 $ middle H2O
22 11  6.0240-2   16 -17  #16 #17 #18 #19     u=2 imp:n,p=1 $ top Al
23  6  1.0004-1   17      #16 #17 #18 #19     u=2 imp:n,p=1 $ top H2O
C
C FUEL PIN - MEDIUM ENRICHED (UNIVERSE = 51)
C
201   9  8.6023-2  (-2 6 -7):(-3 7 -8):(-5 8 -9)  u=51 imp:n,p=1 $ fitting
202   7  8.1299-2  -4 9 -10                       u=51 imp:n,p=1 $ low graphite
203  12  4.2909-2  -1 10 -13        tmp1=4.77-8   u=51 imp:n,p=1 $ inner Zr rod
204 121  8.9782-2   1 -4  10 -771   tmp1=4.77-8   u=51 imp:n,p=1 $ fuel seg. #1
205 122  8.9782-2   1 -4 771 -772   tmp1=4.77-8   u=51 imp:n,p=1 $ fuel seg. #2
206 123  8.9782-2   1 -4 772 -773   tmp1=4.77-8   u=51 imp:n,p=1 $ fuel seg. #3
```

```
207 124  8.9782-2   1 -4 773 -774   tmp1=4.77-8   u=51 imp:n,p=1 $ fuel seg. #4
208 125  8.9782-2   1 -4 774 -13    tmp1=4.77-8   u=51 imp:n,p=1 $ fuel seg. #5
209   7  8.1299-2  -4 13 -14                     u=51 imp:n,p=1 $ up graphite
210   8  8.6218-2   4 -5 9 -14                   u=51 imp:n,p=1 $ cladding
211   9  8.6023-2  (-5 14 -15):(-3 15 -16):(-2 16 -18) u=51
                                                      imp:n,p=1 $ fitting
212  10    -2.112  -6:(2 6 -7)                   u=51 imp:n,p=1 $ mixed Al
213   6  1.0004-1  (3 7 -8):(5 8 -15):(3 15 -16)  u=51 imp:n,p=1 $ H2O
214  11  6.0240-2  (2 16 -17)                    u=51 imp:n,p=1 $ Al
215   6  1.0004-1  (2 17 -18):18                 u=51 imp:n,p=1 $ H2O
C
C MEDIUM ENRICHED 4-ELEMENT BUNDLE (UNIVERSE = 52)
C
216  0         -19   fill=51                   u=52 imp:n,p=1 $ fuelpin SW
217 like 216 but trcl=(3.8862  0  0)                        $ fuelpin SE
218 like 216 but trcl=(0 3.8862  0)                         $ fuelpin NW
219 like 216 but trcl=(3.8862  3.8862  0)                   $ fuelpin NE
C
220 10    -2.112  -7       #216 #217 #218 #219   u=52 imp:n,p=1 $ mixed Al
221  6  1.0004-1   7 -16   #216 #217 #218 #219   u=52 imp:n,p=1 $ middle H2O
222 11  6.0240-2   16 -17  #216 #217 #218 #219   u=52 imp:n,p=1 $ top Al
223  6  1.0004-1   17      #216 #217 #218 #219   u=52 imp:n,p=1 $ top H2O
C
C FUEL PIN - HIGHLY ENRICHED (UNIVERSE = 53)
C
301   9  8.6023-2  (-2 6 -7):(-3 7 -8):(-5 8 -9)  u=53 imp:n,p=1 $ fitting
302   7  8.1299-2  -4 9 -10                       u=53 imp:n,p=1 $ low graphite
303  12  4.2909-2  -1 10 -13        tmp1=4.77-8   u=53 imp:n,p=1 $ inner Zr rod
304 131  8.9782-2   1 -4  10 -771   tmp1=4.77-8   u=53 imp:n,p=1 $ fuel seg. #1
305 132  8.9782-2   1 -4 771 -772   tmp1=4.77-8   u=53 imp:n,p=1 $ fuel seg. #2
306 133  8.9782-2   1 -4 772 -773   tmp1=4.77-8   u=53 imp:n,p=1 $ fuel seg. #3
307 134  8.9782-2   1 -4 773 -774   tmp1=4.77-8   u=53 imp:n,p=1 $ fuel seg. #4
308 135  8.9782-2   1 -4 774 -13    tmp1=4.77-8   u=53 imp:n,p=1 $ fuel seg. #5
309   7  8.1299-2  -4 13 -14                      u=53 imp:n,p=1 $ up graphite
310   8  8.6218-2   4 -5 9 -14                    u=53 imp:n,p=1 $ cladding
311   9  8.6023-2  (-5 14 -15):(-3 15 -16):(-2 16 -18) u=53
                                                      imp:n,p=1 $ fitting
312  10    -2.112  -6:(2 6 -7)                    u=53 imp:n,p=1 $ mixed Al
313   6  1.0004-1  (3 7 -8):(5 8 -15):(3 15 -16)  u=53 imp:n,p=1 $ H2O
314  11  6.0240-2  (2 16 -17)                     u=53 imp:n,p=1 $ Al
315   6  1.0004-1  (2 17 -18):18                  u=53 imp:n,p=1 $ H2O
C
C HIGHLY ENRICHED 4-ELEMENT BUNDLE (UNIVERSE = 54)
C
316  0   -19   fill=53 u=54 imp:n,p=1 $ fuelpin SW
317 like 316 but trcl=(3.8862  0  0)                        $ fuelpin SE
318 like 316 but trcl=(0 3.8862  0)                         $ fuelpin NW
319 like 316 but trcl=(3.8862  3.8862  0)                   $ fuelpin NE
C
320 10    -2.112  -7       #316 #317 #318 #319   u=54 imp:n,p=1 $ mixed Al
321  6  1.0004-1   7 -16   #316 #317 #318 #319   u=54 imp:n,p=1 $ middle H2O
322 11  6.0240-2   16 -17  #316 #317 #318 #319   u=54 imp:n,p=1 $ top Al
323  6  1.0004-1   17      #316 #317 #318 #319   u=54 imp:n,p=1 $ top H2O
C
C
C
C 2-ELEMENT FUEL BUNDLE (UNIVERSE = 3)
C
31 like 316 but trcl=(3.8862  0  0)            u=3         $ fuelpin SE
32 like 316 but trcl=(3.8862  3.8862  0)       u=3         $ fuelpin NE
C
33 10    -2.112  -7        #31 #32            u=3 imp:n,p=1 $ mixed Al
34  6  1.0004-1   7 -16    #31 #32            u=3 imp:n,p=1 $ middle H2O
35 11  6.0240-2   16 -17   #31 #32            u=3 imp:n,p=1 $ top Al
36  6  1.0004-1   17       #31 #32            u=3 imp:n,p=1 $ top H2O
C
C
```

```
C GRAPHITE BLOCK (UNIVERSE = 4)
C
41 10    -2.112  -6                          u=4 imp:n,p=1 $ mixed Al
42  7  8.1299-2   6 -18                      u=4 imp:n,p=1 $ graphite
43  6  1.0004-1   18                         u=4 imp:n,p=1 $ upper H2O
C
C
C WATER BLOCK (UNIVERSE = 5)
C
45 10    -2.112  -6                          u=5 imp:n,p=1 $ mixed Al
46  6  1.0004-1   6                          u=5 imp:n,p=1 $ H2O
C
C
C SHIM SAFETY ROD (UNIVERSE = 6)
C
51   0            -37    31 -32               u=6 imp:n,p=1  $ bottom void
52  12  4.2909-2  -1     32 -10               u=6 imp:n,p=1  $ Zr rod
53 140  8.9782-2   1 -37 32 -10  tmp1=4.77-8  u=6 imp:n,p=1  $ fuel meat
54  13     -2.51  -37    10 -33               u=6 imp:n,p=1  $ borated graphite
55   0            -37    33 -34               u=6 imp:n,p=1  $ top void
56   8  8.6218-2  37 -38 31 -34               u=6 imp:n,p=1  $ cladding
57   6  1.0004-1  38:34:-31                   u=6 imp:n,p=1  $ H2O
C
C SHIM SAFETY ROD IN DUMMY UNIVERSE (UNIVERSE = 7)
C
58  0  -19  fill=6  u=7 imp:n,p=1  $ shim safety at 0%
C
C
C 3-ELEMENT FUEL BUNDLE WITH SHIM SAFETY ROD (UNIVERSE = 8)
C
61 like 58 but trcl=(0 0 32)             u=8         $ SS at 80%
62 like 16 but trcl=(3.8862  0 0)          u=8         $ fuelpin SE
63 like 16 but trcl=(0  3.8862  0)         u=8         $ fuelpin NW
64 like 16 but trcl=(3.8862  3.8862  0)    u=8         $ fuelpin NE
C
65 10    -2.112  -7       #61 #62 #63 #64    u=8 imp:n,p=1 $ mixed Al
66  6  1.0004-1   7 -16   #61 #62 #63 #64    u=8 imp:n,p=1 $ middle H2O
67 11  6.0240-2   16 -17  #61 #62 #63 #64    u=8 imp:n,p=1 $ top Al
68  6  1.0004-1   17      #61 #62 #63 #64    u=8 imp:n,p=1 $ top H2O
C
C
C TRANSIENT ROD AT 100% POSITION (UNIVERSE = 9)
C
71  0            -44 10 -41           u=9 imp:n,p=1 $ void
72 13     -2.51 -44 41 -42           u=9 imp:n,p=1 $ borated graphite
73 11  6.0240-2   44 -45 10 -42       u=9 imp:n,p=1 $ Al cladding
74  6  1.0004-1   45:42:-10           u=9 imp:n,p=1 $ remainder-H2O
C
C
C TRANSIENT ROD IN DUMMY UNIVERSE (UNIVERSE = 10)
C
75  0  -19  fill=9  u=10 imp:n,p=1  $ transient rod at 100%
C
C 3-ELEMENT FUEL BUNDLE WITH TRANSIENT ROD (UNIVERSE = 11)
C
81 like  75 but trcl = (0 0 0)             u=11         $ transnt rod
82 like 216 but trcl=(3.8862  0 0)         u=11         $ fuelpin SE
83 like 216 but trcl=(0 3.8862  0)         u=11         $ fuelpin NW
84 like 216 but trcl=(3.8862  3.8862  0)   u=11         $ fuelpin NE
C
85 10    -2.112  -7       #81 #82 #83 #84  u=11 imp:n,p=1 $ mixed Al
86  6  1.0004-1   7 -16   #81 #82 #83 #84  u=11 imp:n,p=1 $ middle H2O
87 11  6.0240-2   16 -17  #81 #82 #83 #84  u=11 imp:n,p=1 $ top Al
88  6  1.0004-1   17      #81 #82 #83 #84  u=11 imp:n,p=1 $ top H2O
C
C
C
```

```
C REGULATING ROD AT 0% POSITION (UNIVERSE = 13)
C
90 14      -2.5  -44     10 -13          u=13 imp:n,p=1   $ BC4
91 11  6.0240-2   44 -45 10 -13          u=13 imp:n,p=1   $ Al cladding
92  6  1.0004-1   45:13:-10              u=13 imp:n,p=1   $ water
C
C
C REGULATING ROD IN DUMMY UNIVERSE (UNIVERSE = 14)
C
93  0            -19  fill=13   u=14 imp:n,p=1  $ regulating rod at 0%
C
C
C 3-ELEMENT FUEL BUNDLE WITH REGULATING ROD (UNIVERSE = 15)
C
101 like 316 but                                u=15         $ fuelpin SW
102 like 316 but trcl=(3.8862  0 0)             u=15         $ fuelpin SE
103 like  93 but trcl=(0  3.8862  20)           u=15         $ RR at 50%
104 like 316 but trcl=(3.8862  3.8862  0)       u=15         $ fuelpin NE
C
105 10    -2.112  -7      #101 #102 #103 #104  u=15 imp:n,p=1 $ mixed Al
106  6  1.0004-1   7 -16  #101 #102 #103 #104  u=15 imp:n,p=1 $ middle H2O
107 11  6.0240-2   16 -17 #101 #102 #103 #104  u=15 imp:n,p=1 $ top Al
108  6  1.0004-1   17     #101 #102 #103 #104  u=15 imp:n,p=1 $ top H2O
C
C
C ALUMINIUM BLOCK WITH SAFETY/PULSE DETECTORS (UNIVERSE = 20)
111 10  -2.112    -6            u=20  imp:n,p=1     $ mixed Al
112  0             6 -51        u=20  imp:n,p=1     $ detector (void)
113 11  6.0240-2   6 -18 51     u=20  imp:n,p=1     $ Al block
114  6  1.0004-1   18 51        u=20  imp:n,p=1     $ upper water
C
C
C WATER BLOCK WITH LINEAR DETECTOR (UNIVERSE = 21)
116 10  -2.112   -6        u=21  imp:n,p=1     $ mixed Al
117  0            6 -52    u=21  imp:n,p=1     $ detector (void)
118  6  1.0004-1  6  52    u=21  imp:n,p=1     $ H2O block
C
C
C TI DEVICE AL CANS (UNIVERSE = 25)
120  0            -61 64 -65       u=25 imp:n,p=1 $ Lower can
121  0            -62 64 -65       u=25 imp:n,p=1 $ Middle can
122  0            -63 64 -65       u=25 imp:n,p=1 $ Upper can
123  6  1.0004-1  #120 #121 #122 7 u=25 imp:n,p=1 $ H2O
124 10  -2.112    -7               u=25 imp:n,p=1 $ Mixed Al
C
C
C WATER BLOCK WITH PNEUMATIC TUBE (UNIVERSE = 26)
130 10  -2.112   -6        u=26  imp:n,p=1     $ mixed Al
131  0            6 -54    u=26  imp:n,p=1     $ detector (void)
132  6  1.0004-1  6  54    u=26  imp:n,p=1     $ H2O block
C
C
C NEW XENON IRRADIATOR (UNIVERSE = 28)
140  0           -693  683 -684                u=28 imp:n,p=1 $ Xe gas
141 12  4.2909-2 -692  682 -685 (693:-683:684) u=28 imp:n,p=1 $ Zr wall
142  0           -691  681 -686 (692:-682:685) u=28 imp:n,p=1 $ Void/H2O
143 12  4.2909-2 -691    7 -681                u=28 imp:n,p=1 $ Low Zr
144 12  4.2909-2 -691  686                     u=28 imp:n,p=1 $ Up Zr
145 11  6.0240-2  691 -690   7                u=28 imp:n,p=1 $ Al wall
146  6  1.0004-1  690  7                      u=28 imp:n,p=1 $ H20
147 10  -2.112    -7                          u=28 imp:n,p=1 $ Mixed Al
C
C
C IN-CORE VERTICAL FLUX MAPPING DEVICE (UNIVERSE = 30)
151  6  1.0004-1  -700  10 -701  u=30 imp:n,p=1  $ detector  1 (lowest)
152  6  1.0004-1  -700 701 -702  u=30 imp:n,p=1  $ detector  2
153  6  1.0004-1  -700 702 -703  u=30 imp:n,p=1  $ detector  3
```

```
154  6  1.0004-1  -700 703 -704  u=30 imp:n,p=1  $ detector  4
155  6  1.0004-1  -700 704 -705  u=30 imp:n,p=1  $ detector  5
156  6  1.0004-1  -700 705 -706  u=30 imp:n,p=1  $ detector  6
157  6  1.0004-1  -700 706 -707  u=30 imp:n,p=1  $ detector  7
158  6  1.0004-1  -700 707 -708  u=30 imp:n,p=1  $ detector  8
159  6  1.0004-1  -700 708 -709  u=30 imp:n,p=1  $ detector  9
160  6  1.0004-1  -700 709 -13   u=30 imp:n,p=1  $ detector 10 (highest)
161  6  1.0004-1  -10:13:700     u=30 imp:n,p=1  $ remainder
C
C
C INFINITE BUNDLES LATTICE (UNIVERSE = 100)
C
400 0            -101 102 104 -103    lat=1 u=100 imp:n,p=1
                         fill=0:4 -6:2 0:0
C
C                              NOTRH
C                            ==================
                             20  20  21  20   4     $ 9
                              4   4   4   4   4     $ 8
                             54  54  25  54  54     $ 7
                              3   8   2   8  54     $ 6  E
                             54  52  11  52  54     $ 5  A
                              3   8  52   8  52     $ 4  S
                             52  52  25  54  15     $ 3  T
                              4  26  26   4  52     $ 2
                             26   4   4   4   4     $ 1
C                            ==================
C                         A   B   C   D   E   F
C                                SOUTH
C
C
C
C UNIVERSES TO FILL THE REACTOR LATTICES
C  2: low enriched 4-element bundle
C 52: medium enriched 4-element bundle
C 54: highly enriched 4-element bundle
C  3: 2-element fuel bundle
C  4: graphite block
C  5: water block
C  8: 3-element fuel bundle with shim-safety rod
C 11: 3-element fule bundle with transient rod
C 15: 3-element fuel bundle with regulating rod
C 20: aluminum block with safety/pulse detectors
C 21: water block with linear detector
C 25: TI device Al cans
C 26: water block with pneumatic tube
C 28: New Xenon Irradiator
C 30: In-core vertical flux mapping device
C
C REACTOR WINDOW
C
500  0        -105 106 -107 108 -201 202  fill=100  imp:n,p=1 $ reactor
C
501 10  -2.112  203 -106 108 -107 202 -6 imp:n,p=1 $ A row bottom grid
C
502  0        6 -201 -53    imp:n,p=1  $ Log channel detector at A9
c
503 21 -2.3 750 -205 807 -748 809 -819 imp:n,p=1 $ basement concrete
c                 elpt:n 0.01
c
c
c ----------------------------------------------------------c
c ---- IRRADIATION CELL                                 -----c
c ----------------------------------------------------------c
c 700 21 -2.3 824 -814 815 -818 819 -822
c            u=301 imp:n,p=16 $concrete
c                 elpt:n 0.01
```

```
751 20 -0.00125
                (824 -814 815 -818 820 -821)
                 (-9901:9902:-9903:9904:-9905:9906)
                 (-9946:9949:-9923:9924:-9925:9926)
                 (-9972:9973:-9974:9975:-9976:9977)
                 (-9970:9971:-9923:9924:-9925:9926)
                 (-9901:9949:-9903:9904:-9907:9905)
                                      u=301 imp:n,p=16 $air
c ------------------------------------------------------------c
c ---- Pool Wall
c ------------------------------------------------------------c
450 21 -2.3 750 -746 807 -808 819 -822 imp:n,p=1 $back
c                elpt:n 0.01
451 21 -2.3 746 -205 807 -816 819 -822 imp:n,p=1 $left
c                elpt:n 0.01
452 21 -2.3 746 -205 817 -808 819 -822 870 imp:n,p=1 $right w/o penetr
453 21 -2.3 750 -205 807 -808 822 -749 imp:n,p=1 $top
454 21 -2.3 817 -808 -870 imp:n,p=1 $ right w/ penetr
c ********************************************************************
c N Irradiator
c ********************************************************************
99901 20 -0.00125 9901 -9902 9903 -9904 9905 -9906
              (-9940:9941:-9942:9943:-9944:9945)
                                       imp:n,p=16 u=301 $ boral(al)
c
99903 20 -0.00125 9940 -9941 9942 -9943 9944 -9945
              (-9911:9912:-9913:9914:-9915:9916)
                                       imp:n,p=16 u=301 $ boral(b4c)
c
99902 20 -0.00125 9911 -9912 9913 -9914 9915 -9916
              (-9921:9922:-9923:9924:-9925:9926)
                                        imp:n,p=16 u=301 $ boral(al)
c
99927 20 -0.00125 9921 -9922 9923 -9924 9925 -9926
              (-9978:9979:-9980:9981:-9982:9983)
                                        imp:n,p=16 u=301 $ Pb/Bi
c
c 99903 20 -0.00125 9921 -9922 9923 -9924 9925 -9926 imp:n,p=1 u=301 $ void cube
c
99911 20 -0.00125 9954 -9979 9980 -9981 9982 -9983 imp:n,p=16 u=301
99912 20 -0.00125 9955 -9954 9980 -9981 9982 -9983 imp:n,p=16 u=301
99913 20 -0.00125 9956 -9955 9980 -9981 9982 -9983 imp:n,p=16 u=301
99914 20 -0.00125 9957 -9956 9980 -9981 9982 -9983 imp:n,p=16 u=301
c
99915 20 -0.00125 9958 -9957 9980 -9981 9982 -9983 imp:n,p=16 u=301
99916 20 -0.00125 9959 -9958 9980 -9981 9982 -9983 imp:n,p=16 u=301
99917 20 -0.00125 9960 -9959 9980 -9981 9982 -9983 imp:n,p=16 u=301
99918 20 -0.00125 9961 -9960 9974 -9975 9976 -9977 imp:n,p=16 u=301
99922 20 -0.00125 9962 -9961 9980 -9981 9982 -9983 imp:n,p=16 u=301
99923 20 -0.00125 9963 -9962 9980 -9981 9982 -9983 imp:n,p=16 u=301
99924 20 -0.00125 #99911 #99912 #99913 #99914 #99915 #99916 #99917
                  #99918 #99922 #99923
                  9978 -9979 9980 -9981 9982 -9983 imp:n,p=16 u=301
c pre-filter
c
99919 20 -0.00125 9946 -9947 9923 -9924 9925 -9926 imp:n,p=16 u=301
99920 20 -0.00125 9947 -9948 9923 -9924 9925 -9926 imp:n,p=16 u=301
99921 20 -0.00125 9948 -9949 9923 -9924 9925 -9926 imp:n,p=16 u=301
c
99925 20 -0.00125 9972 -9973 9974 -9975 9976 -9977 imp:n,p=16 u=301 $g det1
99926 20 -0.00125 9970 -9971 9923 -9924 9925 -9926 imp:n,p=16 u=301 $nf
c
99928 52 -7.0 9901 -9949 9903 -9904 9907 -9905 imp:n,p=16 u=301 $table
c
c Pre boral box
c
c 99928 11 6.0240-2 9984 -9985 9903 -9904 9905 -9906
```

```
c               (-9984:9986:-9942:9943:-9944:9945)
c                                imp:n,p=16 u=301 $ boral al
c 99929 13 -2.62  9984 -9986 9942 -9943 9944 -9945
c               (-9984:9987:-9913:9914:-9915:9916) imp:n,p=16 u=301
c 99930 11 6.0240-2 9984 -9987 9913 -9914 9915 -9916
c               (-9984:9988:-9923:9924:-9925:9926) imp:n,p=16 u=301
c 99931 20 -0.00125 9984 -9988 9923 -9924 9925 -9926
c                                          imp:n,p=16 u=301
c
c ***************************************************************************
c 450 20 -0.00125  -878 879 880 -814 u=301 imp:n,p=16 $ out cone
c 451 20 -0.00125  -881 880 -814 u=301 imp:n,p=16 $ air in cone
c 452 20 -0.00125  -879 881 880 -814 u=301 imp:n,p=16 $ in cone
c ***
743 0 #751 #99901 #99902 #99903 #99919 #99920 #99921
       #99911 #99912 #99913 #99914 #99915 #99916 #99917 #99918
        #99922 #99923 #99924 #99925 #99926
       #99927 #99928  u=301 imp:n,p=16
c ***
c
c dummy universe for irradiation cell
c
752 0 (824 -814 815 -818 820 -821) u=310 fill=301 imp:n,p=16
c
c
c ---------------------------------------------------------c
c ---- CONCRETE BETWEEN IRRADIATION CELL & RX POOL   -----c
c ---------------------------------------------------------c
c ********************
c thickness 45 (Al,Pb,Bi,Al)*
c ********************
c
c 701 26 -2.88 81 (-803 -804 -805 -806) -802 u=302 imp:n,p=8
                                         $cavity wedge;AlF3 FILTER
c ////////////////////////////////////////////////////////////
701 20 -0.00125 81 (-803 -804 -805 -806) -802 u=302 imp:n,p=8 $Air
c ////////////////////////////////////////////////////////////
c
c ********************
c thickness 15 (Pb,Al,Al,Bi)*
c ********************
c
c 904 27 -1.1050 905 (-803 -804 -805 -806) -81 u=302 imp:n,p=8
                                         $ D2O
c 901 15 -11.4 82 (-803 -804 -805 -806) -905 u=302 IMP:N,P=8
                                         $Cavity wedge;Pb Filter
c ////////////////////////////////////////////////////////////
904 20 -0.00125  905 (-803 -804 -805 -806) -81 u=302 imp:n,p=8 $Air
901 20 -0.00125 82 (-803 -804 -805 -806) -905 u=302 imp:n,p=8 $Air
c ////////////////////////////////////////////////////////////
c
c ********************
c thickness 10 (Bi,Bi,Pb,Pb)*
c ********************
c
c 902 56 -9.78  83 (-803 -804 -805 -806) -82 u=302 imp:n,p=8
                                         $Cavity wedge;Bismuth Filter
c 903 56 -8.65  801 (-803 -804 -805 -806) -83 u=302 imp:n,p=8
                                         $Cavity wedge;Cadmium Filter
c ////////////////////////////////////////////////////////////
902 20 -0.00125 83 (-803 -804 -805 -806) -82 u=302 imp:n,p=8 $Air
903 20 -0.00125 812 (-803 -804 -805 -806) -83
                #765 u=302 imp:n,p=8 $Air
765 20 -0.00125 812 -83 894 -895 896 -897 u=302 imp:n,p=8 $n flux 2
c ////////////////////////////////////////////////////////////
c
c ************************************************************
```

```
c ************************************************************
c ************************************************************
c
702 21 -2.3 #701 #904 #901 #902 #903 #765 u=302 imp:n,p=8
                                      $Concrete w/o cavity wedge
c
c dummy universe for concrete between irradiation cell and rx pool
c
703 0 812 -802 815 -818 820 -821  fill=302 imp:n,p=8
                                        u=303    $real wall
c
c
c ------------------------------------------------------------c
c ---- Aluminum Plate                                  ------c
c ------------------------------------------------------------c
c
705 11 6.0240-2 824 -836 837 -838 839 -840
              -824:841:-842:843:-844:845 imp:n,p=4 u=304 $Al plate
741  13 -2.51  9967 -841 842 -843 844 -845 imp:n,p=4 u=304 $air
761  11 6.0240-2 9964 -9967  842 -843 844 -845 imp:n,p=4
                                      u=304
762  20 -0.00125 9966 -9964 842 -843 844 -845 imp:n,p=4
                                      u=304
763  20 -0.00125 824 -9966  842 -843 844 -845 imp:n,p=4
                                      u=304
744  0 #705 #741 #761 #762 #763 u=304 imp:n,p=4
c
c Al plate in dummy universe
c
742 0 (824 -836 837 -838 839 -840) u=305 fill=304 imp:n,p=4
c
c ------------------------------------------------------------c
c ---- VOID BOX                                        ------c
c ------------------------------------------------------------c
c
706 11 6.0240-2 824 -825 826 -827 828 -829
      (-830:831:-832:833:-834:835) imp:n,p=2 u=307 $Al Void casing
731 15 -11.4 (830 -831 832 -833 834 -835) -846 imp:n,p=2 u=307 $lead
732 20 -0.00125 (830 -831 832 -833 834 -835) 846 imp:n,p=2 u=307 $Void
745 0 #706 #731 #732                   imp:n,p=2 u=307
c
c in dummy universe
c
746 0 (824 -825 826 -827 828 -829) u=308 fill=307 imp:n,p=2
c
c ------------------------------------------------------------c
c ---- PHANTOM                                           ------c
c ------------------------------------------------------------c
c
c 760 0 870 -871 872 -873 874 -875  u=384
c                                                  imp:n,p=1 fill=381
c 761 0 876 -877 878 -879 880 -881 imp:n,p=1 fill=380 u=384
c 762 0 882 -883 884 -885 886 -887 lat=1 u=380 fill=-1:1 -1:1 -1:1 383
c      383 383 383 383 383 383 383 383 383 383 383 383 383 383 383
c      383 383 383 383 383 383 383 383 383 383  imp:n,p=1
c 763 0 882 -883 884 -885 886 -887 lat=1 u=381 imp:n,p=1 fill=382
c 764 6   1.0004-1 888 -889 890 -891 892 -893 u=382 imp:n,p=1
c 765 6   1.0004-1 #764 imp:n,p=1 u=382
c 766 6 1.0004-1 888 -889 890 -891 892 -893 u=383 imp:n,p=1
c 767 6 1.0004-1  #766 imp:n,p=1 u=383
c 768  0 -870:871:-872:873:-874:875 imp:n,p=1 u=384
c
c Phantom in dummy universe
c
c 769 0 (870 -871 872 -873 874 -875) u=385 fill=384 imp:n,p=1
c
c
```

```
c ========================================================================== c
c ====== EXPERIMENTS (ADJUST CELL 888 AFTER ADDING EXPERIMENT)      ======== c
c ========================================================================== c
C
C XENON IRRADIATOR (UNIVERSE = 201)
C
601  0             -506 502 -503           u=201 imp:n,p=1 $ I.C. inside
602  9   8.6023-2  (-507 501 -504) #601    u=201 imp:n,p=1 $ I.C. wall-SS
603  0             -508  #601 #602         u=201 imp:n,p=1 $ Space
604 11   6.0240-2   508                     u=201 imp:n,p=1 $ XeIrr wall (Al)
C
C XENON IRRADIATOR IN DUMMY UNIVERSE (UNIVERSE = 202)
C
606  0             -509 6 -204  fill=201  u=202  imp:n,p=1
607  6  1.0004-1   #606                   u=202  imp:n,p=1
C
C XENON IRRADIATOR IN CURRENT UNIVERSE (TURNED OFF)
C
C 608  like 606  but trcl=(-10.0709 24.288 0)  u=0  $ XeIrr at A6
C
C SUNMAN TUBE (UNIVERSE = 205)
C
610  6  1.0004-1   -520      -10 u=205 imp:n,p=1  $ sunman tube bottom H2O
611  0             -520  10 -771 u=205 imp:n,p=1  $ sunman tube 1st fifth
612  0             -520 771 -772 u=205 imp:n,p=1  $ sunman tube 2nd fifth
613  0             -520 772 -773 u=205 imp:n,p=1  $ sunman tube 3rd fifth
614  0             -520 773 -774 u=205 imp:n,p=1  $ sunman tube 4th fifth
615  0             -520 774  -13 u=205 imp:n,p=1  $ sunman tube 5th fifth
616  0             -520  13      u=205 imp:n,p=1  $ sunman tube top H2O
617 11   6.0240-2   520           u=205 imp:n,p=1  $ Long tube (Aluminum)
C
C SUNMAN TUBE IN DUYMMY UNIVERSE (UNIVERSE = 206)
C
618  0             -521 6 -204  fill=205  u=206  imp:n,p=1
619  6 1.0004-1     #618                  u=206  imp:n,p=1
C
C SUNMAN TUBE IN CURRENT UNIVERSE (TURNED ON)
C
C 620  like 618 but trcl=(-7.7119  -8.096  0)  u=0  $ sunman tube at A2
C 621  like 618 but trcl=(-7.7119   8.096  0)  u=0  $ sunman tube at A4
C 622  like 618 but trcl=(-7.7119  24.288  0)  u=0  $ sunman tube at A6
C 623  like 618 but trcl=(-7.7119  40.480  0)  u=0  $ sunman tube at A8
C
C
C
C LONG TUBE AND AL CANS (UNIVERSE =  207)
C
630  15     -11.4   -531 -543            u=207 imp:n,p=1  $ Bottom lead
634   0             -530 543 -544        u=207 imp:n,p=1  $ Can #1
635   0             -530 544 -545        u=207 imp:n,p=1  $ Can #2
636   0             -530 545 -546        u=207 imp:n,p=1  $ Can #3
637   0             -530 546 -547        u=207 imp:n,p=1  $ Can #4
638   0             -530 547 -548        u=207 imp:n,p=1  $ Can #5
639   0             -530 548 -549        u=207 imp:n,p=1  $ Can #6
640   0             -530 549 -550        u=207 imp:n,p=1  $ Can #7
641   0              530 -531 543 -550   u=207 imp:n,p=1  $ void
642   0             -531 550 -551        u=207 imp:n,p=1  $ void
643   0             -531 551             u=207 imp:n,p=1  $ void
644  11  6.0240-2    531                 u=207 imp:n,p=1  $ Long tube wall
C
C
C LONG TUBE AND AL CANS IN DUMMY UNIVERSE (UNIVERSE = 208)
647   0              -532 6 -204  fill=207  u=208  imp:n,p=1
648   6  1.0004-1    #647                  u=208  imp:n,p=1
C
C LONG TUBE AND AL CANS IN CURRENT UNIVERSE (TURNED OFF)
c 649 like 647 but trcl=(-7.7119 -8.096 8.89) u=0 $ Long tube A2, 1.5" up
```

```
c 650 like 647 but trcl=(-7.7119  8.096 8.89) u=0 $ Long tube A4, 1.5" up
c 651 like 647 but trcl=(-7.7119 24.288 8.89) u=0 $ Long tube A6, 1.5" up
c 652 like 647 but trcl=(-7.7119 40.480 8.89) u=0 $ Long tube A8, 1.5" up
C
C
C TOPAZ BOX (UNIVERSE = 210)
661  14  -2.5     560 -561 562 -563 564 -565   u=210  imp:n,p=1  $ Boral
662  16  -2.33    560 -561 562 -563 565 -566   u=210  imp:n,p=1  $ Topaz
663  14  -2.5     560 -561 562 -563 566 -567   u=210  imp:n,p=1  $ Boral
C
c
C TOPAZ BOX IN DUMMY UNIVERSE (UNIVERSE = 211)
667   0      560 -561 562 -563 564 -567  fill=210 u=211 imp:n,p=1
C
C TOPAZ BOX IN CURRENT UNIVERSE (TURNED OFF)
C 669   like 667  but u=0                                $ Topaz box
c
c final step for configuration of IC (location change)
c
668 like 752 but trcl=(-572.5079 18.1351 36.83) u=0
c
c final step for configulation of concrete btn IC & Rx pool
c
669 like 703 but trcl=(-84.8279  18.1351 36.83) u=0
c
c final step for configulation of Al plate
c
670 like 742 but trcl=(-24.8279  18.1351 36.83) u=0
c
c final step for configulation of void box
c
671 like 746 but trcl=(-12.0729  18.1351 36.83) u=0
c
c final step for configulation of pool wall
c
c 672 like 450 but trcl=(-19.4229 18.1351 0) u=0
c 673 like 451 but trcl=(-19.4229 18.1351 0) u=0
c
c LRL sample loading area
885 20 -0.00125 872 -873 808 -871 874 -875 u=212 imp:n,p=64
883 20 -0.00125 876 -877 808 -878 879 -880
                (-872:873:-808:871:-874:875) u=212 imp:n,p=64
882 20 -0.00125 881 -882 808 -883 884 -885
                (-876:877:-808:878:-879:880) u=212 imp:n,p=64
881 20 -0.00125 886 -887 808 -888 889 -890
                (-881:882:-808:883:-884:885) u=212 imp:n,p=64
880 20 -0.00125 891 -892 808 -893 901 -900
                (-886:887:-808:888:-889:890) u=212 imp:n,p=64
886 20 -0.00125 750 -205 808 -748 819 -749
                (-891:892:-808:893:-901:900) u=212 imp:n,p=64
884 0 #885 #883 #882 #881 #880 #886 u=212 imp:n,p=64
887 0           750 -205 808 -748 819 -749 fill=212
                                u=213 imp:n,p=64
889 like 887 but u=0
C
C space outside of the reactor
c
888 6 1.0004-1 750 -205 807 -748 809 -749
                   #500 #501 #502 #503
                   #450 #451 #452 #453 #454
                   #668 #669 #670 #671
                   #889
                   imp:n,p=1 $ H2O
c
c final outer space
c
9999 0  -750:205:-807:748:-809:749      imp:n,p=0   $ outer
```

```
C ======================================================================
C                              SURFACE CARDS
C ======================================================================
C
c
c concrete between irradiation cell and reactor pool
c
c                        <FILTERS>
c
81  px 56.0 $
905 px 55.9
82  px 17.5 $
83  px 0.1
801 px 15 $
802 px 60 $
803 p 1 0 -2 120
804 p 1 0 2 120
805 p 1 -2 0 120
806 p 1 2 0 120
807 py -368.8951
808 py  362.6249
809 pz -165.57
810 pz 217.6
811 px 150
c
c irradiation cell
c
812 px 0
813 px 60
814 px 487.68
815 py -295.5902
816 py -277.4551
817 py  271.1849
818 py  253.0498
819 pz -115.57
820 pz -152.4
821 pz  152.4
822 pz  189.23
c ********************************************************************************
995 px 156.0646
c ********************************************************************************
c
9972 px  482.68
9973 px  487.58
9974 py -7
9975 py  7
9976 pz -2.5
9977 pz  2.5
894 py -30
895 py  30
896 pz -30
897 pz  30
c 898 pz -7
c 899 pz  7
c ********************
c pre boralbox
c ********************
9984 px 397.52
9989 px 397.521
9990 px 397.522
9991 px 397.523
9985 px 420.37
9986 px 420.27
9987 px 419.835
9988 px 419.735
c ************************************
```

```
c external cube
c ************************************
9901 px 327.66 $50
9902 px 397.51 $50
9903 py -29.845
9904 py  29.845
9905 pz -29.845
9906 pz  29.845
9907 pz -39.845
c ************************************
c middle part
c ************************************
9940 px 327.76 $50
9941 px 397.41 $50
9942 py -29.745
9943 py  29.745
9944 pz -29.745
9945 pz  29.745
c
c internal cube
c
9911 px 328.195 $50
9912 px 396.975 $50
9913 py -29.31
9914 py  29.31
9915 pz -29.31
9916 pz  29.31
c
c void cube
c
9921 px 328.295 $50
9922 px 396.875 $50
9923 py -29.21
9924 py  29.21
9925 pz -29.21
9926 pz  29.21
c
c
c
9978 px 338.455
9979 px 386.715
9980 py -19.05
9981 py  19.05
9982 pz -19.05
9983 pz  19.05
c 8 cubes
c
9931 px 408.68 $50
9932 py -2
9933 py  2
9934 pz -2
9935 pz  2
9954 px 382.3175
9955 px 380.3175
9956 px 373.4275
9957 px 371.4275
9958 px 364.5375
9959 px 362.5375
9960 px 359.0925
9961 px 355.0925
9962 px 350.715
9963 px 348.715
9970 px 325.66
9971 px 326.66
c
c Pre-filter
c
```

```
9946 px 397.52
9947 px 407.51
9948 px 417.51
9949 px 418.51
9950 py -29.845
9951 py  29.845
9952 pz -29.845
9953 pz  29.845
c
c cylinder
c
c 9941 c/z 471 0 15 $ internal
c 9942 c/z 471 0 18 $ external
c
c 9943 pz 60
c
c ********************************************************************************
c ********************************************************************************
823 px 610
c
c void box
c
824 px 0
825 px 10.16
826 py -27.94
827 py  27.94
828 pz -36.83
829 pz  27.6225
830 px 0.3175
831 px 9.8425
832 py -26.67
833 py  26.67
834 pz -34.925
835 pz  26.3526
c
846 pz -29.8607
c
c aluminum window
c
836 px 11.755
837 py -31.27
838 py  31.27
839 pz -31.27
840 pz  31.27
841 px 11.655
842 py -30
843 py  30
844 pz -30
845 pz  30
9964 px 9.85
9965 px 4.08
9966 px 3.08
9967 px 11.22
c 9968 px 12.925
c 9969 px 13.025
c
c rx confinement
c
746 px -572.5079
747 py -259.32
748 py 462.6249
749 pz 250.19
750 px -633.4679  $IC innwe wall
c
c ---------------------------------------------------------------c
c Penetration
c ---------------------------------------------------------------c
```

```
c
870 c/y -120 -100 6.35
c
c ***************************************
871 py 400
872 px -140
873 px -100
874 pz  10
875 pz  50
876 px -142
877 px  -98
c
c ***************************************
c
878 py 402
879 pz 8
c 879 kx 506.5 2.6
880 pz 52
c 881 kx 513 2.6
881 px -143
882 px  -97
883 py  403
884 pz  7
885 pz  53
886 px -153
887 px  -87
c
c ***********************
c
888 py  413
889 pz  -3
c
c ***********************
c
890 pz 63
891 px  -163
892 px  -77
893 py  423
901 pz -4
900 pz 73
c ***********************
c 900 kx 530 1.62
c 901 kx 532 1.62
c 902 px 536
c
c
c ------------------------------------------------------------------c
c ------ REACTOR CORE                                          ----c
c ------------------------------------------------------------------c
c
  1 cz 0.2286    $ Zr rod
  2 cz 0.79      $ top/bottom fitting - smaller radius
  3 cz 1.395     $ top/bottom fitting - larger radius
  4 cz 1.74117   $ fuel meat radius
  5 cz 1.79197   $ feul element radius (=1.411 inch)
C
  6 pz     0     $ fitting (fuel pin bottom)
  7 pz  2.33     $ fitting
  8 pz  7.31     $ fitting
  9 pz  8.89     $ fitting graphite
 10 pz 17.78     $         graphite fuel 0/5
771 pz 25.40     $                  fuel 1/5
772 pz 33.02     $                  fuel 2/5
773 pz 40.64     $                  fuel 3/5
774 pz 48.26     $                  fuel 4/5
 13 pz 55.88     $         graphite fuel 5/5
 14 pz 64.77     $ fitting graphite
```

```
 15 pz 66.35     $ fitting
 16 pz 68.29     $ fitting
 17 pz 70.83     $ fitting
 18 pz 76.20     $ fitting (fuel pin top)
C
19 cz  1.85      $ fuelpin window surface
C
31 pz -38.10     $ shim safety bottom end
32 pz -20.32     $ bottom void - fuel interface
33 pz  53.34     $ boron - top void interface
34 pz  66.04     $ shim safety top end
37 cz  1.69545   $ shim safety inner radius
38 cz  1.74625   $ shim safety outer radius
C
41 pz  68.58     $ transient rod void-fuel interface
42 pz 106.68     $ transient rod top end
44 cz 1.51638    $ transient rod inner radius
45 cz 1.56718    $ transient outer radius
C
51 c/z  1.9431 1.9431 1.905      $ safety/pulse detector housing
52 c/z  1.9431 1.9431 3.001      $ linear channel detector housing
53 c/z  -5.7688  50.5196  2.220  $ log channel detector housing
54 c/z  1.9431 1.9431 3.175      $ pneumatic tube housing
C
61 c/y  1.9431 27.5 3.056  $ TI device lower can
62 c/y  1.9431 35.5 3.056  $ TI device middle can
63 c/y  1.9431 43.5 3.056  $ TI device upper can
64 py   0.2496             $ TI device south plane
65 py   3.6366             $ TI device north plane
C
101 px  5.8031   $ lattice window surface (+x)
102 px -1.9129   $ lattice window surface (-x)
103 py  5.9911   $ lattice window surface (+y)
104 py -2.1049   $ lattice window surface (-y)
C
105 px  36.6471  $ reactor window surface (+x)
106 px  -1.9129  $ reactor window surface (-x)
107 py  54.5671  $ reactor window surface (+y)
108 py -18.2969  $ reactor window surface (-y)
201 pz  96.20    $ reactor window surface (+z) 20 cm above fuel pin
202 pz -12.30    $ reactor window surface (-z) bottom of grid plate
203 px  -9.6248  $ front limite of A row to define gride plate for A row
204 pz  102.33   $ experiment upper limit
c
205 px 60     $ Right x-axis limit for Rx surroundings
206 pz -63.17 $ Lower z-axis limit for Rx surroundings
207 pz 136.83 $ Upper z-axis limit for Rx surroundings
208 pz -80    $ Lower z-axis limit for Rx surroundings(above 60cm concrete)
C
C
C 1000 cc chamber
C
 501 pz   7.58                 $ Xe Irradiator - Irradiation chamber
 502 pz   8.04                 $ Xe Irradiator - Irradiation chamber
 503 pz  28.04                 $ Xe Irradiator - Irradiation chamber
 504 pz  28.50                 $ Xe Irradiator - Irradiation chamber
 506 c/z 1.9431 1.9431 3.985   $ Xe Irradiator - Irradiation chamber
 507 c/z 1.9431 1.9431 4.445   $ Xe Irradiator - Irradiation chamber
C
C 100 cc chamber
C 501 pz  31.73                $ Xe Irradiator - Irradiation chamber
C 502 pz  32.19                $ Xe Irradiator - Irradiation chamber
C 503 pz  41.47                $ Xe Irradiator - Irradiation chamber
C 504 pz  41.93                $ Xe Irradiator - Irradiation chamber
C 506 c/z 1.9431 1.9431 1.851  $ Xe Irradiator - Irradiation chamber
C 507 c/z 1.9431 1.9431 2.310  $ Xe Irradiator - Irradiation chamber
C
```

```
508 c/z 1.9431 1.9431  5.113    $ Xe Irradiator (inner)
509 c/z 1.9431 1.9431  5.715    $ Xe Irradiator (outer)
C
520 c/z 1.9431 1.9431  3.65125  $ SUNMAN tube inner surface
521 c/z 1.9431 1.9431  3.81000  $ SUNMAN tube outer surface
C
C
C
530 c/z 1.9431 1.9431  3.056    $ Long tube - Al can
531 c/z 1.9431 1.9431  3.65125  $ Long tube - inner
532 c/z 1.9431 1.9431  3.81     $ Long tube - outer
543 pz 20.990                   $ Long tube
544 pz 24.377                   $ Long tube
545 pz 27.764                   $ Long tube
546 pz 31.151                   $ Long tube
547 pz 34.538                   $ Long tube
548 pz 37.925                   $ Long tube
549 pz 41.312                   $ Long tube
550 pz 44.699                   $ Long tube
551 pz 49.699                   $ Long tube
C
560 py  -2.1                    $ Topaz box
561 py  38.4                    $ Topaz box
562 pz  18.0                    $ Topaz box
563 pz  56.0                    $ Topaz box
564 px  37.6                    $ Topaz box
565 px  38.2                    $ Topaz box
566 px  43.9                    $ Topaz box (changing)
567 px  44.5                    $ Topaz box (changing)
C
C
C This models Parker's 300 cc cylinder at the best altitude
681 pz   2.932                  $ New Xenon Irradiator
682 pz  23.165                  $ New Xenon Irradiator
683 pz  23.495                  $ New Xenon Irradiator
684 pz  43.277                  $ New Xenon Irradiator
685 pz  43.607                  $ New Xenon Irradiator
686 pz  95.598                  $ New Xenon Irradiator
690 c/z 1.9431 1.9431 3.3293    $ New Xenon Irradiator
691 c/z 1.9431 1.9431 2.7273    $ New Xenon Irradiator
692 c/z 1.9431 1.9431 2.5273    $ New Xenon Irradiator
693 c/z 1.9431 1.9431 2.1971    $ New Xenon Irradiator
C
C
700 c/z 1.9431 1.9431 2.000     $ In-core Vetical Flux Mapping Device
701 pz   21.59                  $ In-core Vetical Flux Mapping Device
702 pz   25.40                  $ In-core Vetical Flux Mapping Device
703 pz   29.21                  $ In-core Vetical Flux Mapping Device
704 pz   33.02                  $ In-core Vetical Flux Mapping Device
705 pz   36.83                  $ In-core Vetical Flux Mapping Device
706 pz   40.64                  $ In-core Vetical Flux Mapping Device
707 pz   44.45                  $ In-core Vetical Flux Mapping Device
708 pz   48.26                  $ In-core Vetical Flux Mapping Device
709 pz   52.07                  $ In-core Vetical Flux Mapping Device
C
C
C
999 s  14.168 18.216 36.83  200   $ big water ball sphere

C ===================================================================
C                       EVERTHING-ELSE CARDS
C ===================================================================
C
C Material Cards
C
C
m111   $ fuel meat (= 8.9781-2)
```

```
         1001.50c   5.4364-2  $ Hydrogen 300K
        40090.63c   1.7482-2  $ Zr in detail (total = 3.3977-2)
        40091.69c   3.8120-3
        40092.69c   5.8270-3
        40094.69c   5.9050-3
        40096.69c   9.5140-4
        68166.69c   1.0560-4
        68167.69c   2.6081-5  $ Fraction of BOL Er-167 (7.2132-5)
        92235.66c   6.1157-4  $ Fraction of BOL U-235 (8.8320-4)
        92238.66c   3.7878-4
        45117.90c   6.9110-6  $ U-235fp for keff=1
mt111   h/zr.62t              $ 600 K, zr/h.04t not used.
C
m112    $ fuel meat (= 8.9781-2)
         1001.50c   5.4364-2  $ Hydrogen 300K
        40090.63c   1.7482-2  $ Zr in detail (total = 3.3977-2)
        40091.69c   3.8120-3
        40092.69c   5.8270-3
        40094.69c   5.9050-3
        40096.69c   9.5140-4
        68166.69c   1.0560-4
        68167.69c   1.7357-5  $ Fraction of BOL Er-167 (7.2132-5)
        92235.66c   5.2790-4  $ Fraction of BOL U-235 (8.8320-4)
        92238.66c   3.7878-4
        45117.90c   6.9110-6  $ U-235fp for keff=1
mt112   h/zr.62t              $ 600 K, zr/h.04t not used.
C
m113    $ fuel meat (= 8.9781-2)
         1001.50c   5.4364-2  $ Hydrogen 300K
        40090.63c   1.7482-2  $ Zr in detail (total = 3.3977-2)
        40091.69c   3.8120-3
        40092.69c   5.8270-3
        40094.69c   5.9050-3
        40096.69c   9.5140-4
        68166.69c   1.0560-4
        68167.69c   1.7143-5  $ Fraction of BOL Er-167 (7.2132-5)
        92235.66c   5.2554-4  $ Fraction of BOL U-235 (8.8320-4)
        92238.66c   3.7878-4
        45117.90c   6.9110-6  $ U-235fp for keff=1
mt113   h/zr.62t              $ 600 K, zr/h.04t not used.
C
m114    $ fuel meat (= 8.9781-2)
         1001.50c   5.4364-2  $ Hydrogen 300K
        40090.63c   1.7482-2  $ Zr in detail (total = 3.3977-2)
        40091.69c   3.8120-3
        40092.69c   5.8270-3
        40094.69c   5.9050-3
        40096.69c   9.5140-4
        68166.69c   1.0560-4
        68167.69c   2.5528-5  $ Fraction of BOL Er-167 (7.2132-5)
        92235.66c   6.0686-4  $ Fraction of BOL U-235 (8.8320-4)
        92238.66c   3.7878-4
        45117.90c   6.9110-6  $ U-235fp for keff=1
mt114   h/zr.62t              $ 600 K, zr/h.04t not used.
C
m115    $ fuel meat (= 8.9781-2)
         1001.50c   5.4364-2  $ Hydrogen 300K
        40090.63c   1.7482-2  $ Zr in detail (total = 3.3977-2)
        40091.69c   3.8120-3
        40092.69c   5.8270-3
        40094.69c   5.9050-3
        40096.69c   9.5140-4
        68166.69c   1.0560-4
        68167.69c   3.9670-5  $ Fraction of BOL Er-167 (7.2132-5)
        92235.66c   7.1162-4  $ Fraction of BOL U-235 (8.8320-4)
        92238.66c   3.7878-4
        45117.90c   6.9110-6  $ U-235fp for keff=1
```

```
mt115  h/zr.62t              $ 600 K, zr/h.04t not used.
C
m121   $ fuel meat (= 8.9781-2)
        1001.50c   5.4364-2  $ Hydrogen 300K
       40090.63c   1.7482-2  $ Zr in detail (total = 3.3977-2)
       40091.69c   3.8120-3
       40092.69c   5.8270-3
       40094.69c   5.9050-3
       40096.69c   9.5140-4
       68166.69c   1.0560-4
       68167.69c   3.4065-5  $ Fraction of BOL Er-167 (7.2132-5)
       92235.66c   6.7352-4  $ Fraction of BOL U-235 (8.8320-4)
       92238.66c   3.7878-4
       45117.90c   6.9110-6  $ U-235fp for keff=1
mt121  h/zr.62t              $ 600 K, zr/h.04t not used.
C
m122   $ fuel meat (= 8.9781-2)
        1001.50c   5.4364-2  $ Hydrogen 300K
       40090.63c   1.7482-2  $ Zr in detail (total = 3.3977-2)
       40091.69c   3.8120-3
       40092.69c   5.8270-3
       40094.69c   5.9050-3
       40096.69c   9.5140-4
       68166.69c   1.0560-4
       68167.69c   2.5771-5  $ Fraction of BOL Er-167 (7.2132-5)
       92235.66c   6.0893-4  $ Fraction of BOL U-235 (8.8320-4)
       92238.66c   3.7878-4
       45117.90c   6.9110-6  $ U-235fp for keff=1
mt122  h/zr.62t              $ 600 K, zr/h.04t not used.
C
m123   $ fuel meat (= 8.9781-2)
        1001.50c   5.4364-2  $ Hydrogen 300K
       40090.63c   1.7482-2  $ Zr in detail (total = 3.3977-2)
       40091.69c   3.8120-3
       40092.69c   5.8270-3
       40094.69c   5.9050-3
       40096.69c   9.5140-4
       68166.69c   1.0560-4
       68167.69c   2.5558-5  $ Fraction of BOL Er-167 (7.2132-5)
       92235.66c   6.0712-4  $ Fraction of BOL U-235 (8.8320-4)
       92238.66c   3.7878-4
       45117.90c   6.9110-6 $ U-235fp for keff=1
mt123  h/zr.62t             $ 600 K, zr/h.04t not used.
c
m124   $ fuel meat (= 8.9781-2)
        1001.50c   5.4364-2  $ Hydrogen 300K
       40090.63c   1.7482-2  $ Zr in detail (total = 3.3977-2)
       40091.69c   3.8120-3
       40092.69c   5.8270-3
       40094.69c   5.9050-3
       40096.69c   9.5140-4
       68166.69c   1.0560-4
       68167.69c   3.3558-5  $ Fraction of BOL Er-167 (7.2132-5)
       92235.66c   6.6988-4  $ Fraction of BOL U-235 (8.8320-4)
       92238.66c   3.7878-4
       45117.90c   6.9110-6 $ U-235fp for keff=1
mt124  h/zr.62t              $ 600 K, zr/h.04t not used.
c
m125   $ fuel meat (= 8.9781-2)
        1001.50c   5.4364-2  $ Hydrogen 300K
       40090.63c   1.7482-2  $ Zr in detail (total = 3.3977-2)
       40091.69c   3.8120-3
       40092.69c   5.8270-3
       40094.69c   5.9050-3
       40096.69c   9.5140-4
       68166.69c   1.0560-4
       68167.69c   4.6006-5  $ Fraction of BOL Er-167 (7.2132-5)
```

```
       92235.66c   7.5075-4  $ Fraction of BOL U-235 (8.8320-4)
       92238.66c   3.7878-4
       45117.90c   6.9110-6  $ U-235fp for keff=1
mt125  h/zr.62t              $ 600 K, zr/h.04t not used.
C
m131   $ fuel meat (= 8.9781-2)
        1001.50c   5.4364-2  $ Hydrogen 300K
       40090.63c   1.7482-2  $ Zr in detail (total = 3.3977-2)
       40091.69c   3.8120-3
       40092.69c   5.8270-3
       40094.69c   5.9050-3
       40096.69c   9.5140-4
       68166.69c   1.0560-4
       68167.69c   4.1919-5  $ Fraction of BOL Er-167 (7.2132-5)
       92235.66c   7.2594-4  $ Fraction of BOL U-235 (8.8320-4)
       92238.66c   3.7878-4
       45117.90c   6.9110-6  $ U-235fp for keff=1
mt131  h/zr.62t              $ 600 K, zr/h.04t not used.
C
m132   $ fuel meat (= 8.9781-2)
        1001.50c   5.4364-2  $ Hydrogen 300K
       40090.63c   1.7482-2  $ Zr in detail (total = 3.3977-2)
       40091.69c   3.8120-3
       40092.69c   5.8270-3
       40094.69c   5.9050-3
       40096.69c   9.5140-4
       68166.69c   1.0560-4
       68167.69c   3.4625-5  $ Fraction of BOL Er-167 (7.2132-5)
       92235.66c   6.7750-4  $ Fraction of BOL U-235 (8.8320-4)
       92238.66c   3.7878-4
       45117.90c   6.9110-6  $ U-235fp for keff=1
mt132  h/zr.62t              $ 600 K, zr/h.04t not used.
C
m133   $ fuel meat (= 8.9781-2)
        1001.50c   5.4364-2  $ Hydrogen 300K
       40090.63c   1.7482-2  $ Zr in detail (total = 3.3977-2)
       40091.69c   3.8120-3
       40092.69c   5.8270-3
       40094.69c   5.9050-3
       40096.69c   9.5140-4
       68166.69c   1.0560-4
       68167.69c   3.4433-5  $ Fraction of BOL Er-167 (7.2132-5)
       92235.66c   6.7614-4  $ Fraction of BOL U-235 (8.8320-4)
       92238.66c   3.7878-4
       45117.90c   6.9110-6  $ U-235fp for keff=1
mt133  h/zr.62t              $ 600 K, zr/h.04t not used.
C
m134   $ fuel meat (= 8.9781-2)
        1001.50c   5.4364-2  $ Hydrogen 300K
       40090.63c   1.7482-2  $ Zr in detail (total = 3.3977-2)
       40091.69c   3.8120-3
       40092.69c   5.8270-3
       40094.69c   5.9050-3
       40096.69c   9.5140-4
       68166.69c   1.0560-4
       68167.69c   4.1484-5  $ Fraction of BOL Er-167 (7.2132-5)
       92235.66c   7.2321-4  $ Fraction of BOL U-235 (8.8320-4)
       92238.66c   3.7878-4
       45117.90c   6.9110-6  $ U-235fp for keff=1
mt134  h/zr.62t              $ 600 K, zr/h.04t not used.
C
m135   $ fuel meat (= 8.9781-2)
        1001.50c   5.4364-2  $ Hydrogen 300K
       40090.63c   1.7482-2  $ Zr in detail (total = 3.3977-2)
       40091.69c   3.8120-3
       40092.69c   5.8270-3
       40094.69c   5.9050-3
```

```
       40096.69c   9.5140-4
       68166.69c   1.0560-4
       68167.69c   5.1844-5  $ Fraction of BOL Er-167 (7.2132-5)
       92235.66c   7.8386-4  $ Fraction of BOL U-235 (8.8320-4)
       92238.66c   3.7878-4
       45117.90c   6.9110-6  $ U-235fp for keff=1
mt135  h/zr.62t             $ 600 K, zr/h.04t not used.
C
m140   $ fuel meat - SS follower (= 8.9781-2)
        1001.50c   5.4364-2  $ Hydrogen 300K
       40090.63c   1.7482-2  $ Zr in detail (total = 3.3977-2)
       40091.69c   3.8120-3
       40092.69c   5.8270-3
       40094.69c   5.9050-3
       40096.69c   9.5140-4
       68166.69c   1.0560-4
       68167.69c   2.5334-5  $ 35% of BOL Er-167 (7.2132-5)
       92235.66c   5.9670-4  $ 68% of BOL U-235 (8.8320-4)
       92238.66c   3.7878-4
       45117.90c   6.9110-6  $ U-235fp for keff=1
mt140  h/zr.62t             $ 600 K, zr/h.04t not used.
C
C
C
m6     $ water (= 1.0004-1)
        1001.50c   0.66666
        8016.50c   0.33334
mt6     lwtr.60t   $ 300 K
C
c ***************************
c m27     $ D2O
c        1002.50c  0.66666
c        8016.50c  0.33334
c ////////////////////////////
c         82000.35c 1.0 $Pb
c ////////////////////////////
c ***************************
c
m7     $ graphite (= 8.1299-2)
        6012.50c   1.0000
mt7     grph.60t
C
m8     $ cladding (= 8.6218-2)
       26000.55c   0.70071
       24000.50c   0.20162
       28000.50c   0.09399
        6012.50c   0.00368
C
m9     $ SS304 (= 8.6023-2)
       26000.55c   0.68826
       24000.50c   0.20210
       28000.50c   0.08951
        6012.50c   0.02013
C
m10    $ mixed aluminium (= -2.112: water 33% and Al 66% in volume)
        1001.50c   -0.018
        8016.50c   -0.142
       13027.50c   -0.840
C
m11    $ aluminium (= 6.0240-2)
       13027.50c   1.0
C
m12    $ Zr (= 4.2909-2)
       40000.42c   1.0
C
m13    $ borated graphite (= 2.51 g/cm3 assumed)
        5010.50c  -0.1557
```

```
        5011.55c  -0.6269
        6012.50c  -0.2174
mt13    grph.60t
C
m14    $ B4C powder (= 2.5 g/cm3)
        5010.50c  -0.038925
        5011.55c  -0.156725
        6012.50c  -0.80435
C
c ******************************
m15    $ lead (= 11.4 g/cm3)
c        82000.50c   1.0000
c ////////////////////////////
         82000.42c 1.0
c ////////////////////////////
c
c ******************************
C
m16    $ Topaz (= 2.33 g/cm3 - NSC measured density)
        1001.50c   0.15094
        8016.50c   0.52830
        9019.50c   0.03774
       13027.50c   0.18868
       14000.50c   0.09434
C
c m17    $ Au-197 (This X-section is to calculate Au-198 production)
c       79197.50c  1.0
C
C m18    $ Xe-124 (This X-section is to calculate Xe-125 production)
C        54124.61c  1.0
C
c m19    $ Co-59 (This X-section is to calculate Co-60 production)
c       27059.60c  1.0
m20    $ dry air
       7014.42c -0.755 8016.50c -0.232 18000.42c -0.013 $ dry air
c
m21    $ Concrete
       1001.50c   0.105
       8016.50c   0.584
       11023.50c  0.014
       12000.50c  0.00188
       13027.50c  0.0319
       14000.50c  0.211
       19000.50c  0.0092
       20000.50c  0.0389
       26000.55c  0.00413
C
c ****************************
c m22    $ Bismuth
c       83209.42c -1
c ////////////////////////////
c        83209.35c 1.0 $Bi
c ////////////////////////////
c ****************************
c
c ****************************
c m23    $ Cadmium
c       48000.42c -1
c ////////////////////////////
c        83209.35c 1.0 $Bi
c ////////////////////////////
c ****************************
C
c m24    $ boron-contained water
c       1001.50c -0.109975
c       8016.50c -0.879975
c       5010.50c -0.00005
```

```
c
c m25    $ polyethylene
c       1001.50c 2
c       6000.60c 1
c mt25   poly.01t
c ***************************
c m26    $AlF3 (d=2.88 g/cc)
c       13027.50c -0.5869565
c        9019.50c -0.4130435
c ////////////////////////////
c        13027.35c 1.0
c ////////////////////////////
c m50 82000.35c 1.0 $Pb
c
c m51 83209.35c 1.0 $Bi
m52 26000.55c 1.0 $Fe-Nat
c m53 16032.50c 1.0 $S
c m54  5010.50c 1.0 $B
c m55 14000.50c 1.0 $Si-nat
c m56 22000.50c 1.0 $Ti-nat
c m57 28058.35c 1.0 $Ni-58
c m58 23000.50c 1.0 $V-nat
c m59 42000.50c 1.0 $Mo
c m60 74000.55c 1.0 $W
m61     $Pb-Bi Alloy
        82000.42c -0.443 $Pb
        83209.42c -0.5561 $Bi
        51000.42c -0.00033 $Ab
        29000.50c -0.000024 $Cu
        30000.42c -0.000013 $Zn
        48000.42c -0.001 $Cd
        50000.42c -0.001 $Tin
c
c ////////////////////////////
c ***************************
C sdef sur=999 nrm=-1
C sdef pos=0 0 35
C
c xs1  1001.69c  0.999170   xs558 xs2/xs558 2 1    2898   2048 512 4.8085E-08
c xs2  40090.69c 89.132004  xs558 xs2/xs558 2 8    28639  2048 512 4.8085E-08
c xs3  40091.69c 90.122002  xs558 xs2/xs558 2 65   61053  2048 512 4.8085E-08
c xs4  40092.69c 91.112000  xs558 xs2/xs558 2 186  47337  2048 512 4.8085E-08
c xs5  40094.69c 93.096001  xs558 xs2/xs558 2 280  49780  2048 512 4.8085E-08
c xs6  40096.69c 95.081001  xs558 xs2/xs558 2 379  26269  2048 512 4.8085E-08
c xs7  68166.69c 164.505005 xs558 xs2/xs558 2 432  55622  2048 512 4.8085E-08
c xs8  68167.69c 165.498001 xs558 xs2/xs558 2 542  76649  2048 512 4.8085E-08
c xs9  92235.69c 233.025000 xs558 xs2/xs558 2 693  362610 2048 512 4.8085E-08
c xs10 92238.69c 236.006000 xs558 xs2/xs558 2 1403 427430 2048 512 4.8085E-08
C
C
xs1   1001.69c .999170       h1.558 xs1/h1.558    1 1  2898  0 0 4.808E-08
xs2  40090.63c 89.13200    zr90.600 xs1/zr90.600  1 1 34005  0 0 5.170E-08
xs3  40091.69c 90.122002   zr91.558 xs1/zr91.558  1 1 61053  0 0 4.808E-08
xs4  40092.69c 91.112000   zr92.558 xs1/zr92.558  1 1 47337  0 0 4.808E-08
xs5  40094.69c 93.096001   zr94.558 xs1/zr94.558  1 1 49780  0 0 4.808E-08
xs6  40096.69c 95.081001   zr96.558 xs1/zr96.558  1 1 26269  0 0 4.808E-08
xs7  68166.69c 164.505005 er166.558 xs1/er166.558 1 1 55622  0 0 4.808E-08
xs8  68167.69c 165.498001 er167.558 xs1/er167.558 1 1 76649  0 0 4.808E-08
c xs992235.69c 233.025000  u235.558 xs1/u235.558  1 1 362610 0 0 4.808E-08
c xs1092238.69c 236.006000 u238.558 xs1/u238.558  1 1 427430 0 0 4.808E-08
xs9 54124.61c 122.842000 xe124.300 xs1/xe124.300 1 1 10050 0 0 2.5852E-08
C
print
prdmp
C
C * calculate Au-198 production rate from thermal and epi-th nentrons *
C  Date: 5/6/01
```

```
C
c e0 4e-7  100   $ thermal, other
C A2,A4,A6,A8 (low can --> high can)
C
c f14:n (634<649) (635<649) (636<649) (637<649) (638<649)
c f24:n (634<650) (635<650) (636<650) (637<650) (638<650)
c f34:n (634<651) (635<651) (636<651) (637<651) (638<651)
c f44:n (634<652) (635<652) (636<652) (637<652) (638<652)
C
C D3,D7 (low can --> high can)
C
c f14:n (120<400[2 0 0])  (121<400[2 0 0])  (122<400[2 0 0])
c f24:n (120<400[2 -4 0]) (121<400[2 -4 0]) (122<400[2 -4 0])
c n, photon flux at surface 894 , 895
mode n p
c f12:n 894 895
c fm12 7.5e+16
c e12 0 1e-9 2m 2m 2m 2m 2m 2m 2m 2m 2m 2m 2m 2m 2m 2m 2m 2m 2m 2m 2m 2m
c           2m 2m 2m 2m 2m 2m 2m 2m 2m 2m 2m 2m 2m
c f22:p 894 895
c fm22 7.5e+16
c
c e22 0 1e-9 2m 2m 2m 2m 2m 2m 2m 2m 2m 2m 2m 2m 2m 2m 2m 2m 2m 2m 2m 2m
c           2m 2m 2m 2m 2m 2m 2m 2m 2m 2m 2m 2m 2m
c
c f16:n 753 764
c fm16 7.5e+16
c f26:p 753
c fm26 7.5e+16
c
C n flux (#/cm2/sec)
c ***
f14:n 741 701 904 99911 99912 99913 99914 99915 99916 99917 99918
                  99922 99923 99925 99926 765 885 880 886
c ***
c ***
fm14 7.5e+16
c ***
c ***
e14 1e-8 2m 2m 2m 2m 2m 2m 2m 2m 2m 2m 2m 2m 2m 2m 2m 2m
         2m 2m 2m 2m 2m 2m 2m 2m 2m 2m 2m 2m 2m 2m 2m
c 1e-1 2e-1 4e-1 6e-1 8e-1 1 1.2 1.4 1.6 1.8 2 2.2
c           2.4 2.6 2.8 3 5 7 9 13
c ***
c
c f15:n -129.1 18.14 36.8 2
c fm15 7.5e+16
c f25:n -133.1 18.14 36.8 2
c fm25 7.5e+16
c f35:n -137.1 18.14 36.8 2
c fm35 7.5e+16
c photon flux (#/cm2/sec)
c ***
f24:p 741 701 904 99911 99912 99913 99914 99915 99916 99917 99918
              99922 99923 99925 99926 765 885 880 886
c ***
c ***
fm24 7.5e+16
c ***
c ***
e24 0 1e-4 2m 2m 2m 2m 2m 2m 2m 2m 2m 2m 2m 2m 2m 2m 2m 2m 2m
c 1e-1 2e-1 4e-1 6e-1 8e-1 1 1.2 1.4 1.6 1.8 2 2.2
c           2.4 2.6 2.8 3
c ***
c gamma dose (rad)
c ***
f34:n 741 701 904 99911 99912 99913 99914 99915 99916 99917 99918
```

```
                  99922 99923 99925 99926 765 885 880 886
c ***
c ***
fm34 7.5e+16
e34 1e-2 2m 2m 2m 2m 2m 2m 1 2 3 4 5 6 7 8 9 10 15
c 1.6045e-9 6 -5 -6
c ***
c ***
f44:p 99911 99912 99913 99914 99915 99916 99917 99918 99925 99926
c ***
c ***
fm44 7.5e+16
e44 1e-2 2m 2m 2m 2m 2m 2m 1 2 3 4 5 6 7 8 9 10 15
c ***
c gamma dose (rad/particle)
c f16:p 753 764
c fm16  1.6e-8
c
f54:n  99927
fm54 (-1 61 -2)
e54 1e-3 1e-2 2m 2m 2m 2m 2m 2m 1 2 3 4 5 6 7
f64:n 99901 99902
fm64 (-1 11 -2)
e64 1e-3 1e-2 2m 2m 2m 2m 2m 2m 1 2 3 4 5 6 7
f74:n 99911
fm74 (-1 20 -2)
e74 1e-3 1e-2 2m 2m 2m 2m 2m 2m 1 2 3 4 5 6 7
f84:n 450 451 453
fm84 (-1 21 -2)
e84 1e-3 1e-2 2m 2m 2m 2m 2m 2m 1 2 3 4 5 6 7
c n dose (rad/particle)
c ***
f16:n 741 701 904 99911 99912 99913 99914 99915 99916 99917 99918
                  99922 99923 99925 99926 765 885 880 886
c ***
c ***
fm16 1.6e-8
c ***
c p dose (rad/particle)
c ***
f26:p 741 701 904 99911 99912 99913 99914 99915 99916 99917 99918
                  99922 99923 99925 99926 765 885 880 886
c ***
c ***
fm26 1.6e-8
c ***
c
c n dose (rad/particle)
c f18:n 99903
c fm18 1.6e-8
c p dose (rad/particle)
c f28:p 99903
c fm28 1.6e-8
c
c
```

```
C
c fm14 (2.293+14 17 -2)  $ Au198 produc. rate for 1 g of Au-197 (atoms/s)
c fm24 (2.293+14 17 -2)  $ Au198 produc. rate for 1 g of Au-197 (atoms/s)
c fm34 (2.293+14 17 -2)  $ Au198 produc. rate for 1 g of Au-197 (atoms/s)
c fm44 (2.293+14 17 -2)  $ Au198 produc. rate for 1 g of Au-197 (atoms/s)
c fm54 (2.293+14 17 -2)  $ Au198 produc. rate for 1 g of Au-197 (atoms/s)
c fm64 (2.293+14 17 -2)  $ Au198 produc. rate for 1 g of Au-197 (atoms/s)
C
C
thtme 0
kcode 10000 1.0 50 200
c ksrc 0 0 35
c void
```

VITA

The author, Si Young Jang, was born in 1967, in Youngdong Chungbuk, Korea. He attended the Hanyang University and earned a B.S. degree in nuclear engineering in 1989. He attended the Korea Advanced Institute of Science and Technology and earned a M.S. degree in nuclear engineering in 1991. He then worked as a researcher and senior researcher in the Korea Institute of Nuclear Safety for almost ten years. He entered Texas A&M University in 2001, to pursue a Ph.D. degree in the health physics program. He earned his Ph.D. degree in nuclear engineering in August 2004. Si Young Jang's current mailing address is: 231 Yangjeong, Yongdong Chungbuk, Korea.